UNITED KINGDOM • CHINA • MALAYSIA

Hydrogen Production through Sorption-Enhanced Steam Reforming of Ethanol using CaO-Based Sorbent mixed with Iron Oxide Catalyst

Hind Omer Elsheikh Elfaki

A thesis submitted to The University of Nottingham for the degree of Doctor of Philosophy

February 2016

Abstract

Novel synthetic CaO-based sorbents for carbon dioxide (CO_2) capture in sorption-enhanced steam reforming (SESR) were prepared by the co-precipitation method. Magnesium oxide (MgO) and cerium oxide (CeO_2) were mixed with calcium oxide (CaO) in different molar percentages in order to obtain the optimum percentage, which provide high CO_2 uptake capacity and cyclic stability. The TGA results for CO_2 uptake, revealed that for the molar ratio of CaO, MgO and CeO_2 of (6:2:1) and (4:2:1), the sorbents had CO_2 capture capacity of 29 and 25 wt.%, respectively.

The fresh sorbents were characterized using X-ray diffraction, mercury porosimetry, N_2 physisorption and scanning electron microscopy. It was found that the sorbents with higher CO_2 uptake capacities had relatively high porous surface structure with porosity percentage (>66%). Modelling of CO_2 uptake kinetics showed that JMA (Johnson-Mehl-Avrami) fits best the first and second stages except for the molar ratio of CaO, MgO and CeO_2 of (4:2:1) sample where, surface chemisorption (SC) fits the initial stage and JMA fits the second stage. While the contracting volume model (CV2/3) fits the final stages of all the studied sorbents. The stability of sorbents at high temperatures was examined over multiple cycles of carbonation/de-carbonation reactions. After 45 cycles, the sample with a molar ratio of CaO, MgO and CeO_2 of (6:2:1) remained as high as 25 wt.% (0.43g CO_2 /1g CaO) with only 25% decrease from its CO_2 uptake capacity as a fresh sample. Therefore, the latter sample was selected to be mixed with iron oxide catalyst and used for the SESR.

The study of ethanol steam reforming employing an iron oxide as a catalyst, with and without in-situ CO_2 removal, has been investigated. The results confirmed that iron oxide exhibited catalytic activity for hydrogen (H_2) production from ethanol steam reforming/decomposition reactions. Furthermore, the CaO-based sorbent had sucessfully decrease the amount of CO_2 produced during ethanol reforming reaction up to 70 min of reaction time. Ethanol reformation with in-situ CO_2 removal was investigated at 550-

700 °C. The maximum H_2 yield achieved was 3.5 mol (H_2) /mol (EtOH) at 600°C. GC results revealed that there was no evidence of CO and C across the studied temperature range. The results showed an enhancement in reaction reactivity by increasing the gas hourly space velocities (GHSVs). The amount of H_2 produced remained stable within 10 cycles, which is equivalent to 30 hours of reaction time.

Publications

- Abstract "Sorption-enhanced steam reforming of ethanol using CaO-based sorbent mixed with iron oxide catalyst" was accepted for oral presentation and as preceeding paper in the 6th International Conference on Hydrogen Production, May 2015, UOIT-Oshawa-Ontario-Canada.
- Abstract "Hydrogen production through sorption-enhanced steam reforming of ethanol using CaO-based sorbent mixed with iron oxide catalyst" was presented as a poster in ETRI Energy Policy Conference, December 2015, Nottingham-UK.
- Abstract "Hydrogen production through sorption-enhanced steam reforming of ethanol using CaO-based sorbent mixed with iron oxide catalyst" was presented as a poster in H_2FC SUPERGEN 2015 conference, December 2015, Bath-UK.

Dedication

To my family, my friend and high school teacher Linda and to Mr. Kamal Salih (Uncle Kamal) the former Library Officer in the National Energy Research Centre-Khartoum-Sudan.

Acknowledgement

I would like first to thank the almighty God for giving me strength to complete this work. Secondly, I would like to express my deepest gratitude to my supervisor Prof. Gavin Walker for his step-by step guidance, patience and the constructive suggestions and comments throughout this work. I also would like to thank Dr. John Andresen for his guidance during the first year of my study. My thanks are due to the Technical Staff in the Wolfson building for their patience and kind assistance. Special thanks to my mentor Dr. Martin Khzouz and also to William Boardman for their technical support and help in the setting up of the steam reforming (SR) reactor. Many thanks are also due to my office mates: Gulcan and Joel for their care, support and for the great working environment we have had together. The financial support from Islamic Development Bank (IDB) and University of Nottingham, UK, (Advanced Material Research Division) are also acknowledged. My gratitude is immeasurable to my family for their unlimited love, support and encouragement.

Table of Contents

List of Figures

List of Tables

List of Abbreviations

$a\ (BET)$	The specific surface area.
a.u	Arbitrary unit.
AFC	Alkaline Fuel Cells.
AMP	2-Amino-2-methyl-1-propano.
$b_{experimental}$	The total line broadening.
$b_{instrument}$	Instrument constant.
b_{size}	The peak width/degree.
BASF	Baden Aniline and Soda Factory.
BET	Brunauer-Emmett-Teller.
BSE	Backscattered electron.
c	Constant related exponentially to the heats of adsorption and liquefaction of the gas.
CEA	Chemical Equilibrium with Applications.
CV	Contracting volume model.
D	Diameter of the capillary.
d	The distance between planes of atoms in a crystallite.
DMFC	Direct Methanol Fuel Cell.
EDX	Energy-dispersive X-ray spectroscopy.
ESR	Ethanol steam reforming.
FID	Flame ionization detector.
FSC	Fixed-site-carrier.

FT	Fischer–Tropsch.
FWHM	Full width at half maximum.
GC	Gas Chromatograph.
Gt	Giga (10^9) tonnes of oil equivalent.
Gt CO_2-eq	Giga tonnes of carbon-dioxide equivalent.
GHSV	Gas hourly space velocity.
HC	Hydrocarbon gases.
HHV	Higher Heating Value/ kJ/g.
HT	High temperature shift reaction
HTLC	Hydrotolcite-like compounds
HTR	High Temperature nuclear reactor
IC	Internal combustion engine
IGCC	Integrated gasification combined cycle
ILs	Ionic Liquids
INDC	Intended Nationally Determined Contributions.
IPA	Isopropyl alcohol.
IUPAC	International Union of Pure and Applied Chemistry.
JMA	Johnson-Mehl-Avrami model
J	Joule
k	Reaction rate constant
L	Alvogado constant
LDH	Layered double hydroxides
LHSV	Liquid hourly space velocity

LHV	Lower Heating Value/ kJ/g
LT	Low temperature shift reaction.
m/z	Mass/charge ratio.
MCFC	Molten Carbonate Fuel Cell.
MDEA	N-Methyldiethanolamine
MEA	Monoethanolamine, liquid solvent.
Mtoe	Energy unit, million (10^6) tonne of oil equivalent
n	The order of diffraction.
$N(P)$	The number of the adsorbed moles per unit mass of the adsorbent at pressure p.
NHC	Non-hydrocarbon gases
Nm^3	Normal cubic meters of hydrogen.
Non-OCED	Countries not members in Organization for Economic Cooperation and Development
OECD	Countries members in Organization for Economic Cooperation and Development
p	Pressure
p_0	Saturation pressure of adsorbate gas at the experimental temperature
PAFC	Phosphoric Acid Fuel Cell
PC	Propylene carbonate
PD	Pore size distribution/ $f(w)$

PEM	Proton Exchange Membrane Fuel Cell
PPM	Parts per million
PSA	Pressure swing adsorption
$q1$	Heat of adsorption on the first layer,
ql	Heat of liquefaction of the adsorbed gas on all other layers
R	The gas constant.
SC	Surface reaction model (chemisorption)
SE	Secondary electrons
SEM	Scanning electron microscopy
SE	Secondary electrons
SESR	Sorption enhanced steam reforming
SEHP	Sorption enhanced hydrogen production
SESRE	Sorption enhanced steam reforming of ethanol
SMR	Steam methane reforming
SOFC	Solid Oxide Fuel Cell
SR	Steam reforming
t	Crystallite size/ nm.
TCD	Thermal conductivity detector
TGA	Thermogravimetric analyser
TPED	Total primary energy demand
TSA	Temperature swing adsorption

TW	Energy unit, Terawatt (10^{12} watts).
β	Peak width
γ	Surface tension of the liquid
σ	Contact angle of the liquid
θ	Bragg angle/ degree.
λ	X-ray wavelength/ nm.
o	The average cross-sectional area

CHAPTER ONE

Introduction

1.1. Current and Future Energy Situation

The population increase and the urbanisation across the world has given an increase in the global demand for energy. The world population in 2011 was estimated to be 7 billion with corresponding worldwide energy consumption of 15 TW. In 2050, the world energy consumption is projected to be 30 TW for the growing world population of nine billion (Dincer and Acar, 2015). However, fossil fuels, which meet most of the global energy demand are being lessened every recent day, see Figure 1.1. The increase of the worldwide energy consumption is expected to occur in the non-OECD countries (countries which are not members in Organization for Economic Cooperation and Development), it is estimated to be 63 % in 2035 compared with the OECD countries, see Table 1.1

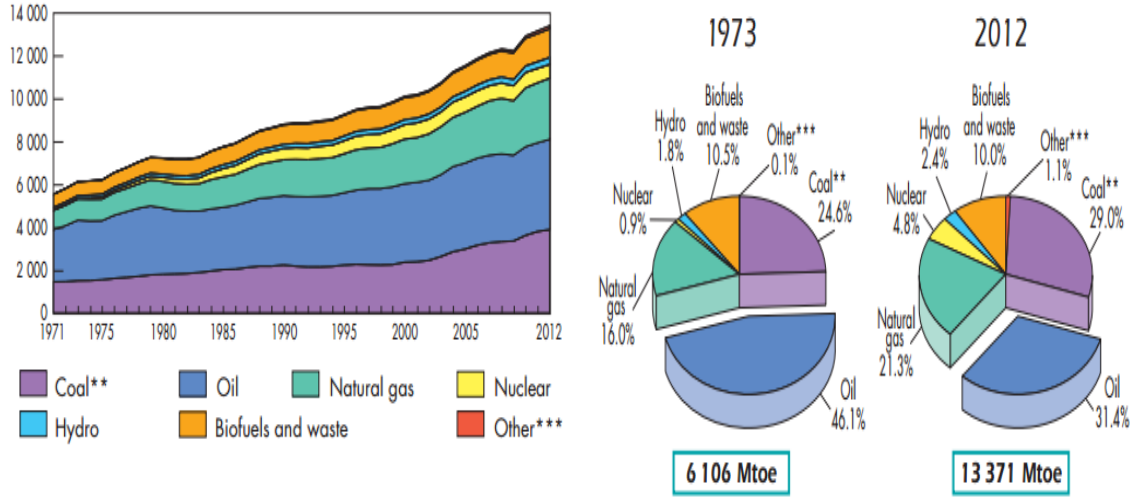

Figure 1.1. World total primary energy supply and share from 1971 to 2012/ Mtoe (IEA, 2014).

Table 1.1. World primary energy demand and energy-related CO_2 emissions and projection 2000-2035 (IEA, 2012).

	2000	2010	2020	2035
Total	10097	12730	14922	17197
Coal	2378	3474	4082	4218
Oil	3659	4113	4457	4656
Gas	2073	2740	3266	4106
Nuclear	676	719	1 138	886
Hydro	226	295	388	488
Bioenergy*	1027	1277	1532	1881
Other renewable	60	112	299	710
Fossil fuel share in TPED	80%	81%	79%	75%
Non-OECD share of TPED**	45%	55%	60%	65%
CO_2 emission(Gt)	23.7	30.2	34.6	37.0

* Includes traditional and modern biomass uses. ** Excludes international bunkers. Note: TPED : total primary energy demand; Mtoe : million tonnes of oil equivalent; Gt Gigatonnes.

1.2. Energy and carbon dioxide emissions

Our climate has witnessed a fundamental change. Storms, floods and heat waves become more frequent and intense (Winter, 2009). From the year 1850 to 2000, the global surface temperature was increased by 1 °C from 13.5 °C to 14.5°C. Accordingly, the sea level had been raised from -150 to +50 mm over the period time of 1870 - 2000. From 1920 to 2000, the ice cover in the Northern Hemisphere decreased from 37 to 35 million km^3, see Figure 1.2. Carbon dioxide and other greenhouse gases are considered the main causes of the climate changes (Winter, 2009). The concentration of atmospheric CO_2 was 280 ppm during the pre-industrial time. Over the past century, carbon dioxide (CO_2) concentrations in the atmosphere have been increased dramatically (Winter, 2009).

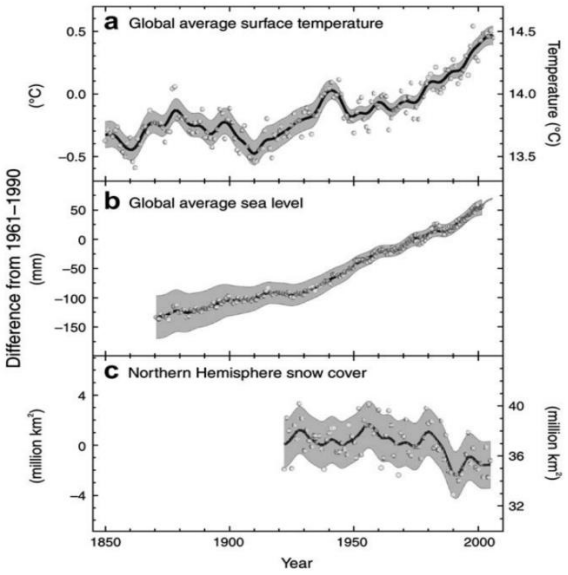

Figure 1.2. Changes in temperature, sea level and Northern Hemisphere snow cover (Winter, 2009).

In the last ten years, the average growth the CO_2 atmospheric concentration has been estimated to be 2 ppmv per year. Particularly, the global carbon dioxide emissions related to energy production are expected to increase by 46 % from 31.2 $\times 10^{9}$ metric tons in 2010 to 36.4 $\times 10^{9}$ metric tons in 2020 and 45.5 $\times 10^{9}$ metric tons in 2040, see Figure 1.3. Table 1.2 presents the world energy and process–related greenhouse gas emission in the INDC scenarios for period 2013-2030.

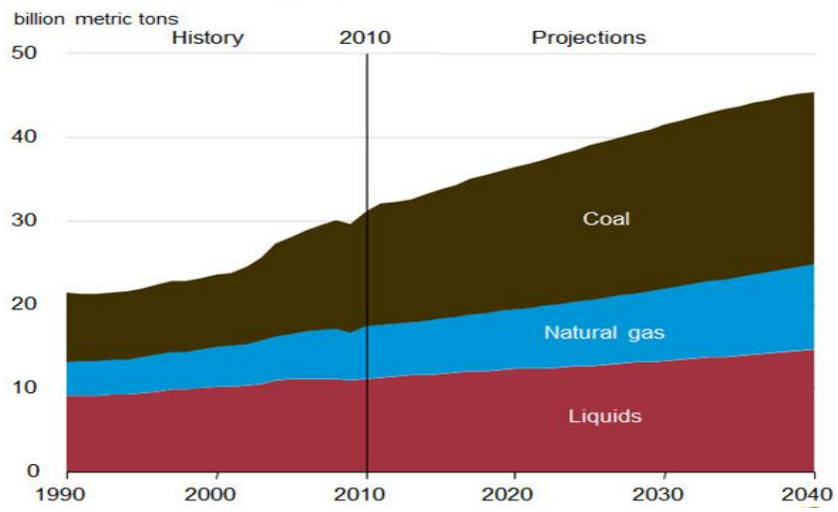

Figure 1.3. World energy related carbon dioxide emissions by fuel, 1990-2035 (IEA, 2013).

Table 1.2. Global energy and process –related greenhouse gas emission in the INDC scenarios/ Gt CO_2-eq (IEA, 2015).

	2013	2020	2025	2030
Energy related				
Carbon dioxide(CO_2)	32.2	33.9	34.3	34.8
Methane (CH_4)	3.0	3.1	3.1	3.1
Nitrous oxide(N_2O)	0.3	0.3	0.4	0.4
Process related				
Carbon dioxide (CO_2)	2.0	2.2	2.2	2.3
Total	37.5	39.5	40.0	40.6

Gt CO_2-eq: Giga tonnes of carbon-dioxide equivalent, INDC: Intended Nationally Determined Contributions

However, over the projection period, from 2010 to 2040, with the adapted polices for efficient usage of energy worldwide, the CO_2 atmospheric concentration may decrease by 2.7% per year in the non-OECD countries and 1.9% per year in the OECD countries (IEA, 2013). Different approaches are being adopted by those countries to reduce the CO_2 emission such as:

- Encourage the utilisation of renewable energy i.e. solar, wind and bioenergy in private and industrial sectors.
- Improve the energy efficiency of and use low carbon fuel including hydrogen and nuclear power.
- Appling CO_2 capture and storage technologies (Leung et al., 2014).

1.3. Carbon dioxide capture technologies

The technical approaches of carbon dioxide (CO_2) capture depend fundamentally on the way that CO_2 is produced. In some processes such as cement manufacture and power plants, CO_2 is produced as a by-product from the combustion process. Therefore, CO_2 separation requires a separate process. In some other industrial processes, CO_2 capture is an integrated step. The technical methods of CO_2 capture can be categorised according

to the modification process used to enable CO_2 separation. The three main technologies established for CO_2 capture and separation are; the post-combustion, pre-combustion and oxy-fuel combustion systems.

1.3.1. Post-combustion system

About 40% of worldwide CO_2 atmospheric emissions are from power plants sources (Cuéllar-Franca and Azapagic, 2015, Markewitz et al., 2012). Post-combustion involves separation of the CO_2 from the flue gases of existing power plants. The plant flue gas contains large volume of nitrogen and relatively small level of CO_2 (7-14% for coal–fired plant volume and 4% gas fired plant) (Leung et al., 2014). Therefore, large equipment is required for CO_2 separation (Cuéllar-Franca and Azapagic, 2015). Liquid solvents such as monoethanolamine (MEA) are employed for the CO_2 capture from the flue gas stream. However, MEA regeneration require high heat consumption and accordingly this method is not economically feasible (Cuéllar-Franca and Azapagic, 2015).

1.3.2. Pre-combustion system

A pre-combustion is usually used at the integrated gasification combined cycle (IGCC) power plants (Leung et al., 2014). Fossil fuels or biomass react with steam in the presence of a controlled amount of oxygen gas or air. This partial oxidation provides heat which leads to the chemical fragmentation of the fuel. The resultant gas mixture consists mostly of carbon monoxide and hydrogen (synthesised gas i.e. syngas)(Leung et al., 2014). Then the syngas is shifted to hydrogen while the carbon monoxide is converted to separable CO_2. The CO_2 concentration in the produced mixture is >20% by volume (Leung et al., 2014). Then, CO_2 is separated into a pure stream using CO_2 sorbent. Pre-combustion is considered a less expensive technology compared to post-combustion and it is preferable for new plants (Yang et al., 2008).

1.3.3. Oxy-fuel combustion system

The fuel combusted in a pure, or nearly pure, oxygen stream to produce flue gases which consist mainly of water vapor and CO_2 (Leung et al., 2014). The product gas

mixture consists of CO_2, water, SO_2 and particulates. SO_2 is removed by a desulphurization method while particulates are removed by an electrostatic precipitation. The resulting gas which contains 80-98% of the CO_2 is then compressed and stored (Leung et al., 2014). The separation and extraction of oxygen from air increases the energy penalty (Yang et al., 2008, Cuéllar-Franca and Azapagic, 2015). The oxy-fuel technology is considered immature and the expenses of its operating and capital cost is nearly as much as post-combustion (Yang et al., 2008). Table 1.3 gives the comparison factors between the three CO_2 capture technologies.

Table 1.3. Advantages and disadvantage of the different CO_2 capture technologies (Leung et al., 2014).

Capture process	Application area	Advantage	Disadvantage
Post-combustion	Coal-fired and gas-fired plants	Mature technology; can easily retrofit into existing plants	Low CO_2 concentration affects the capture efficiency
Pre-combustion	Coal-gasification plants	High CO_2 concentration enhance sorption efficiency, fully developed technology, commercially deployed at the required scale in some industrial sectors, opportunity for retrofit to exciting plant	Heat transfer problems and efficiency decay due to the usage of hydrogen rich gas turbine fuel, energy need for sorbent regeneration, high capital and operating cost for current sorption systems.
Oxy-fuel combustion	Coal-fired and gas–fired plants	Very high CO_2 concentration that enhances sorption efficiency, mature air separation technologies available, reduced volume of gas to treated, hence require smaller equipment	High efficiency drop and energy penalty, cryogenic O_2 production is expensive, corrosion problems may arise.

1.4. Hydrogen Energy

Hydrogen utilization as low carbon fuel is considered one of the main approaches to reduce CO_2 emission and mitigate global climate change. Hydrogen is the lightest element, its concentration in air is only about 0.01% (Suban et al., 2001). Hydrogen is an abundant element, consisting 75% of the mass of nature materials and over 90% by number of atoms (Mariolakos et al., 2007). The physical properties of hydrogen fuel are (Norbeck et al., 1997):

- Hydrogen flammability: a combustible mixture can be produced with only 4% hydrogen by volume with air.
- Hydrogen ignition energy is low (0.02 MJ).
- Hydrogen heating value is high in comparison with the other fuels.
- Hydrogen diffusivity in air is relatively high which favours for safety in case of hydrogen leakage.

The heating values of hydrogen fuels and other alternative fuels are given in Table 1.4.

Table 1.4. Higher and lower heating values of hydrogen and common fossil fuels at 25 °C and 101.325 × 10 ^{3} Pa (Dincer and Acar, 2015).

Fuel	Higher Heating Value (HHV)/ kJ/g	Lower Heating Value (LHV)/ kJ/g
Hydrogen	141.9	119.9
Methane	55.5	50.0
Gasoline	47.5	44.5
Diesel	44.8	42.5
Methanol	20.0	18.1

1.4.1. Current and Future Hydrogen Production

Hydrogen can be produced through different technologies and each of these technologies has barriers that limit their application, see Table 1.5. Currently the world wide annual production of hydrogen is 5×10^{11} m^3, 95 vol.% of the worldwide hydrogen is being produced from fossil fuels through catalytic steam reforming, partial oxidation, or a combination of the two, see Table 1.6 (Lipman, 2004). The latter processes collectively liberate 0.4 Gt (CO_2)/year (Pacala and Socolow, 2004) which contribute to the increase of the annual global carbon emissions.

Table 1.5. Summary of hydrogen production technologies (EC, 2003).

Hydrogen production technology	Benefits	Barriers
Electrolysis: splitting water using electricity	Commercially available with proven technology; Well-understood industrial process; modular; high purity hydrogen, convenient for producing H_2 from renewable electricity, compensates for intermittent nature of some renewables	Competition with direct use of renewable electricity
Reforming (stationary and vehicle applications): splitting hydrocarbon fuel with heat and steam	Well-understood at large scale; widespread; low cost hydrogen from natural gas; opportunity to combine with large scale CO_2 sequestration (carbon storage)	Small-scale units not commercial; hydrogen contains some impurities - gas cleaning may be required for some applications; CO_2 emissions; CO_2 sequestration adds costs; primary fuel may be used directly
Gasification: splitting heavy hydrocarbons and biomass into hydrogen and gases for reforming	Well-understood for heavy hydro-carbons at large scale; can be used for solid and liquid fuels; possible synergies with synthetic fuels from biomass-biomass gasification being demonstrated	Small units very rare; hydrogen usually requires extensive cleaning before use; biomass gasification still under research; biomass has land-use implications; competition with synthetic fuels from biomass
Thermochemical cycles using cheap high temperature heat from nuclear or concentrated solar energy	Potentially large scale production at low cost and without greenhouse gas emission for heavy industry or transportation; International collaboration (USA, Europe and Japan) on research, development and deployment	Complex, not yet commercial, research and development needed over 10 years on the process: materials, chemistry technology; High Temperature nuclear reactor (HTR) deployment needed, or solar thermal concentrators
Biological production: algae and bacteria produce hydrogen directly in some conditions	Potentially large resource	Slow hydrogen production rates; large area needed; most appropriate organisms not yet found; still under research

Accelerating climate change, with associated economic and environmental impacts and limitation of fossil fuel reserves, has promoted the investigation of alternative resources for hydrogen production (Dunn, 2002). The steam reforming process (SMR) is the dominant industrial process for hydrogen production (Twigg and Twigg, 1989). Natural gas is considered the cheapest fossil fuel for SMR process. The quality of the feedstock also affects the percentage of CO_2 produced (Collodi and Wheeler, 2010). Conventional

steam reforming has a lot of disadvantages beside the high percentage of the CO_2 produced such as the cost and the size of the reformer and carbon deposition which reduces the reforming catalyst activity. To overcome these problems combining the reforming and the CO_2 capture in one reactor is proposed. This process is known as sorption enhanced steam reforming (SESR), which was discussed in more detail in sections 2.4.

The alternative processes for hydrogen production include water electrolysis using off-peak nuclear power, high-temperature thermochemical cycles based on nuclear energy or solar energy (Floch et al., 2007). Most of the studied thermochemical cycles showed poor practical feasibility (Lewis and Taylor, 2006, McQuillan et al., 2005). Bio-liquids have been proposed as an alternative feedstock the production of hydrogen, since they are is renewable and can be CO_2 neutral (Martos et al., 2009, Wang and Wang, 2009).

Table 1.6. Annual worldwide hydrogen production shares by source (2004) (Lipman, 2004).

Source	Production/ $Nm^3(10^9)$/ Year	Share/ %
Natural gas	240	48
Oil	150	30
Coal	90	18
Electrolysis	20	4
Total	500	100

Note: Nm^3 are normal cubic meters of hydrogen.

1.4.2. Current and Future Hydrogen Utilization and storage technologies

About 50 vol.% of the worldwide hydrogen production is used in ammonia synthesis plants for fertilizer production. Hydrogen gas is used in the refineries for desulfurisation reactions. Energy utilisation of hydrogen includes the high temperature industrial furnaces, internal combustion engine (IC) and rockets (BACAS, 2006).

Fuel cells have a similar operational concept as batteries, they consist of anode, cathode

and electrolyte. Fuel cells use hydrogen as a fuel, see Figure 1.4. Hydrogen gas is introduced to the fuel cell from the anode side where, H_2 is oxidized and releases electrons while passing through the electrolyte to the cathode. The released electrons generate direct electric current which is drawn through an external electric circuit to the cathode. The H^+ protons react at the cathode with oxygen to form H_2O (Jain, 2009). Table1.7 compares the various types of the fuel cell.

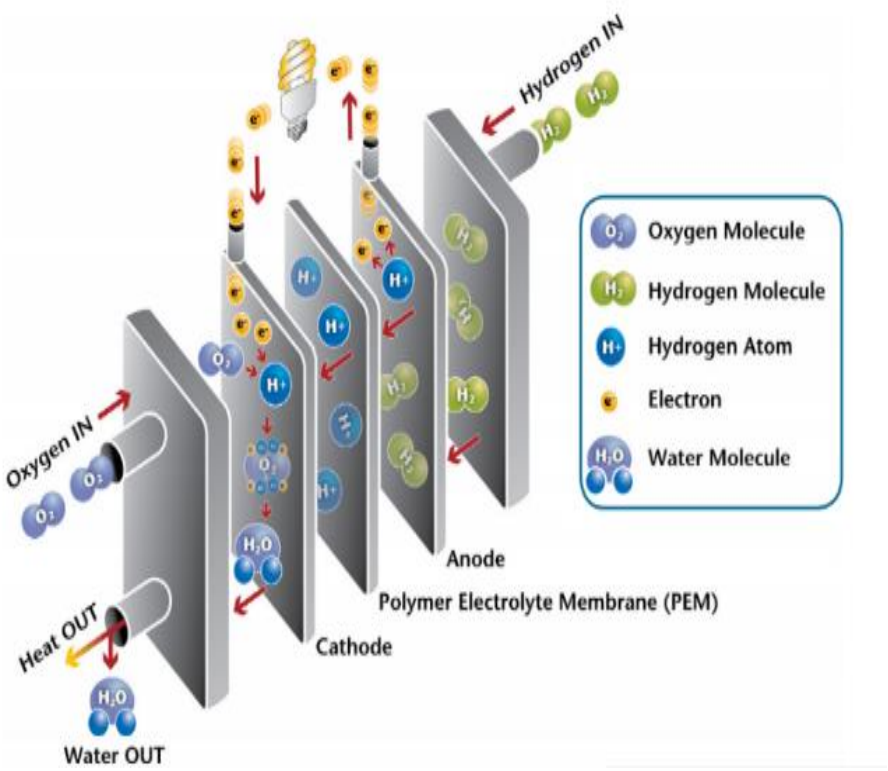

Figure 1.4. Principal of working of fuel cell (EERE, 2010).

Table 1.7. Comparison of fuel cells technologies (EERE, 2010).

Fuel Cell Type	Common Electrolyte	Operating Temperature	Typical Stack Size	Efficiency	Applications	Advantages	Challenges
Polymer Electrolyte Membrane (PEM)*	Perfluoro sulfonic acid	50-100°C typically 80°C	1 kW–100 kW	60% transportation 35% stationary	-Backup power -Portable power Distributed generation -Transportation - Specialty vehicles	-Solid electrolyte reduces corrosion & electrolyte management problems -Low temperature -Quick start-up	-Expensive catalysts Sensitive to fuel impurities -Low temperature waste heat
Alkaline (AFC)	Aqueous solution of potassium hydroxide soaked in a matrix	90-100°C	10–100 kW	60%	Military Space	-Cathode reaction faster in alkaline electrolyte, leads to high performance -Low cost components	-Sensitive to CO_2 in fuel and air -Electrolyte management
Phosphoric Acid (PAFC)	Acid (PAFC) Phosphoric acid soaked in a matrix	150-200°C	400 kW 100 kW module	40%	Distributed generation	-Higher temperature enables CHP -Increased tolerance to fuel impurities	-Pt catalyst -Long start up time -Low current and power
Molten Carbonate (MCFC)	Solution of lithium, sodium, and/or potassium carbonates, soaked in a matrix	600-700°C	300 kW–3 MW 300 kW module	45-50%	-Electric utility -Distributed generation	-High efficiency -Fuel flexibility -Can use a variety of catalysts Suitable for CHP	-High temperature corrosion and breakdown of cell components -Long start up time -Low power density
Solid Oxide (SOFC)	Yttria stabilized zirconia	700-1000°C	1 kW–2 MW	60%	-Auxiliary power -Electric utility Distributed generation	-High efficiency -Fuel flexibility Can use a variety of catalysts -Solid electrolyte Suitable for CHP & CHHP -Hybrid/GT cycle	-High temperature corrosion and breakdown of cell components -High temperature operation requires long start up time and limits

1.4.3. Hydrogen storage system

A feasible hydrogen storage system is considered a critical issue in the current and future utilisation. Hydrogen can be stored in different forms such as:

- Metal hydride, which absorbs/desorbs hydrogen at low pressure but, still

considered as expensive approach.

- High-pressure, the hydrogen is compressed to 69 $\times 10^6$ Pa and stored at 2×10^7 Pa in special cylindrical tanks made from graphite. The compression energy is estimated to be 16.7472 kJ /mol H_2.
- Chemical carriers such as anhydrous ammonia.
- Cryogenic, where insulated tanks are used to store liquid hydrogen at (-253 °C). This method is complicated and intensively energy consuming (Jain, 2009, Momirlan and Veziroglu, 2005).

Table 1.8 gives a summary of the hydrogen storage technologies and the barriers of their applications. At the present time, the on-board hydrogen storage in the automotive is considered the main challenge to comply with a range of greater than 500 km which is a technical requirement (Ball and Wietschel, 2009).

Table 1.8. Summary of hydrogen storage technologies (EC, 2003).

Hydrogen storage technology	Benefits	Barriers
Compressed gas cylinders	Well understood up to pressures of 200bar;	Only relatively small amounts of H_2 are stored at $2 \prec 10^7$ pa ; fuel and storage energy densities at high pressure (7×10^7pa) are comparable to liquid hydrogen, but still lower than for gasoline and diesel; high pressure storage still under development Very low temperatures require super insulation; cost can be high; some hydrogen is lost through evaporation; energy intensity of liquid hydrogen production; energy stored still not comparable to liquid fossil fuels Heavy; can degrade with time; currently expensive; filling requires cooling-circuit Challenges in the logistics of handling of waste products and in infrastructure requirements Not fully understood or developed; early promise remains unfulfilled
Liquid tanks	generally available; can be low cost	Very low temperatures require super insulation; cost can be high; some hydrogen is lost through evaporation; energy intensity of liquid hydrogen production; energy stored still not comparable to liquid fuels
Metal hydrides	Well-understood technology; good storage	Heavy; can degrade with time; currently expensive; filling requires cooling-circuit
Chemical hydrides	density possible	Challenges in the logistics of handling of waste products and in infrastructure requirements
Carbon structures	Some technology available; solid-state storage;	Not fully understood or developed; early promise remains unfulfilled

1.5. Thesis scope and motivation

Conventional steam reforming (SR) is a multi-step hydrogen production process. It consists of a high temperature endothermic reaction (850°C), followed by two stages of low temperature shift reactions (250-450°C) in order to increase the hydrogen yield. CO_2 removal is needed with additional energy consumption. Sorption enhanced steam reforming (SESR) is a novel method for hydrogen production. SESR integrates the reforming, CO_2 capture and water–gas shift (WGS) in one reactor (Hufton et al., 1999, Waldron et al., 2001). SESR aims to achieve high hydrocarbon conversion to hydrogen (>90%) and high purity of the produced hydrogen (98%) with concentration of ppm level of CO and CO_2 impurities in the produced gas stream (Harrison, 2008, Lysikov et al., 2008). To avoid poisoning, CO impurity level must be reduced in many current applications e.g. fuel cell (Bhatia and Wang, 2004).

The choice of suitable CO_2 removal sorbents is based on different criteria such as capacity, selectivity, adequate adsorption/ desorption kinetics, significant stability, low cost and ease of regeneration capability (Yong et al., 2001). The most commonly used sorbent for SESR is calcium oxide (CaO), which can reversibly react with CO_2 to form calcium carbonate (Blamey et al., 2010). Much attention has been given to CaO due to its high CO_2 capture capacity and its low cost (Anthony, 2011). The deactivation of CaO-based adsorbent over multiple cycles of carbonation/de-carbonation reactions is well known in the literature (Abanades and Alvarez, 2003, Barker, 1973). It was reported that the CO_2 adsorption capacity of natural CaO declines by 80% after few cycles (10-20 cycles) (Park and Yi, 2012a). The decay of the CO_2 capture capacity may be caused by gas impurities and coke deposition, which reduce the number of active sites, and therefore the reaction rate is decreased. Sintering of the adsorbents usually occurs at high regeneration temperatures and causes irreversible physical changes such as loss of the porous structure (Blamey et al., 2010). Bandi et al., 2002 reported that the CaO adsorption capacity could be maintained during the cycling process by addition of inert material (Bandi et al., 2002). These inert materials disperse between CaO particles and

prevent its sintering (Bandi et al., 2002). However, to the knowledge of the author, there are no studies that report the synthesis CaO by the addition of magnesium oxides (MgO) and cerium oxide (CeO_2) by the co-precipitation method and being used for CO_2 capture in SESR. Iron oxide is used for hydrogen production in the iron-steam process and as an oxygen carrier in the chemical-looping process. There is a lack of literature for employing iron oxide as a catalyst in the steam reforming process. The key novelty of this research was related to employing iron oxide as a catalyst in SR. Therefore, the preparation of CaO-based sorbent in different molar percentages and selection of the most suitable percentage to be mixed with iron oxide as reforming catalyst for ethanol steam reformation were conducted in this work.

1.6. Aims and Objectives

The two major aims of this study are, first to develop CaO- based sorbent with adequate CO_2 uptake capacity and reliable stability over multiple cycle carbonation/ de-carbonation reactions. Second, investigate the hypothesis of employing iron oxide as a reforming catalyst by applying the synthetic CaO-sorbent and iron oxide mixture in ethanol sorption enhanced steam reforming process.

The objectives of this study are:

- Investigate the synthesis of a novel CaO-based sorbent modified by magnesium oxides (MgO) and cerium oxide (CeO_2) using co-precipitation method in different molar percentages and evaluate their CO_2 uptake capacities during multiple cycles of carbonation/de-carbonation reactions.
- Study the effect composition has upon the physical and chemical properties of the prepared CaO-based sorbents in order to explore the differences and similarities between them and relate the characterisation results with their CO_2 uptake capacities.
- Investigate the kinetics of the CO_2 uptake reaction and identifying any effect of oxide composition has upon the mechanism of carbonation.

- Employ the iron oxide/sorbent mixture in the SESR process and explore the optimum operating conditions for hydrogen production.

1.7. Thesis outline.

There are a literature review of the steam reforming process, reforming catalysts, the catalyst deactivation mechanisms, ethanol steam reforming, iron oxide as a catalyst, sorption enhanced steam reforming, the CO_2 accepters, CO_2 accepters regeneration processes and overview of alternative CO_2 capture technologies in chapter 2. The equipment and testing instruments used for the sorbents and catalyst preparation and characterisation and a detailed description of the ethanol steam reforming rig and gas analysis are described in chapter 3. Chapter 4 presents the CO_2 uptake performance of the prepared CaO-based sorbent and assess the effect of magnesium oxide (MgO) and cerium oxide (CeO_2) addition as modifying element to enhance the CO_2 uptake capacity and stability of CaO.

Characterisation tests of powder X-ray diffraction (XRD), scanning electron microscopy (SEM), measurement of surface area and porosity were done to understand the effect of varying the molar composition on the microstructure of the prepared samples. The modelling of the sorption kinetics was studied to understand the CO_2 uptake mechanism. The CO_2 capture capacities and their cyclic stability of the prepared samples were evaluated over multiple carbonation/de-carbonation cycles. Chapter 5 presents a study of ethanol steam reforming with and without in-situ CO_2 removal. The effect of varying temperature in the range 550-700° C, applying different GHSV and long stability of the catalyst and CO_2 sorbent over 30 hours of reaction time were investigated. Finally, the findings and general conclusions of this study and recommendations for future study are presented in chapter 6.

CHAPTER TWO

Literature Review

1.2. Introduction

This chapter discusses the literature for steam reforming processes. In particular the following topics are covered: criteria of practical reforming catalyst and catalyst deactivation modes in section (2.2), ethanol steam reforming in section (2.3), Iron oxide catalyst in section (2.4), sorption enhanced steam reforming and the different CO_2 sorbents in section (2.5), Calcium oxide (CaO) regeneration processes in section (2.6). Alternative CO_2 capture technologies are also discussed in section (2.7).

2.2. Steam reforming (SR)

Steam reforming (SR) is the main process for hydrogen production (Twigg and Twigg, 1989). It is a catalytic reaction which can convert hydrocarbons in the presence of steam to form a mixture of hydrogen, carbon dioxide and carbon monoxide. SR reaction is usually followed by methanation and water-gas shift (WGS) reactions to form methane and carbon dioxide, see equation 2.1, 2.2, and 2.3.

Steam reforming (SR):

$$C_nH_mO_z + (n-z)\ H_2O \rightarrow (n+\frac{m}{2}-z)\ H_2 + n\ CO \qquad (2.1)$$

Methanation: $CO + 3H_2 \leftrightarrow CH_4 + H_2O \qquad \Delta H^0{}_{298} = -216.73\ kJ/mol \qquad (2.2)$

Water-gas shift (WGS): $CO + H_2O \leftrightarrow H_2 + CO_2 \qquad \Delta H^0{}_{298} = -41.2\ kJ/mol \qquad (2.3)$

The reforming unit is normally expensive and has intensive energy consumption. Efficient and reliable operation is the key to the performance of the whole plant. The first description of steam reforming process was by Tessie du Motay and Marechal in 1868

(Rostrup-Nielsen, 1984). However, the first methane steam reformers were started up in Germany by BASF (Baden Aniline and Soda Factory) in 1926. In 1930, the Standard Oil Company of New Jersey (now Exxon) in United States produced hydrogen in a steam reformer. These reformers were operated at slightly above atmospheric pressure. By the 1950s, the operating pressure of the steam reformer had increased in the range of 0.4 to 1 MPa. In the 1960s, for integrated steam reforming and ammonia-synthesis plants, the process pressure had increased to 3MPa. Recently, reforming processes have been designed to operate at high pressure i.e. 2.5–3MPa and at temperatures around 1000°C. Steam reforming is an endothermic reaction that needs external energy supply. Waste gases from the hydrogen purification unit are often burned to provide the external heat required. Up to 25% of the feed stock may also be combusted to drive the endothermic reaction (Rostrup-Nielsen, 1984). Partial oxidation and auto-thermal reforming are alternative reforming technologies. Table 2.1 shows the advantage and the disadvantage of these technologies.

Table 2.1 Summary of fossil fuel reforming technologies (Khzouz, 2014).

Technology	Chemical reaction	Advantages	Disadvantages
Steam reforming	$C_nH_mO_z + (n-z)\ H_2O \rightarrow (n+\frac{m}{2}-z)\ H_2 + n\,CO$	-Most developed industrial process -No oxygen requirement -Lowest operating temperature -Best H_2/CO ratio.	-Higher air emission
Auto-thermal reforming	$C_nH_mO_z + yO_2 + 2\ (n-y-\frac{z}{2})\ H_2O \rightarrow n\,CO_2 + 2\ (n-y-\frac{z}{2}+\frac{m}{4})H_2$	-Lower process temperature than partial oxidation -Low methane slip	-Limited commercial experience -Air/oxygen requirement
Partial oxidation	$C_n\ H_m\ O_z + \frac{1}{2}(n-z)\ O_2 \rightarrow n\,CO + \frac{m}{2}H_2$	Reduced desulfurisation requirement -No catalyst requirement - Low methane slip	-Low H_2/CO ratio -High operating temperatures -Complex handling process

2.2.1. Steam methane reforming (SMR)

SMR process is the dominant industrial process for hydrogen production (Twigg and Twigg, 1989). SMR is an highly energy consuming process, which involves multiple-steps and has many disadvantages such as the high expenses of reformer manufacture, low hydrogen yield and carbon deposition (Bhat and Sadhukhan, 2009, Ramkumar et al., 2012). Reformer tubes must be made from alloy that usually is expensive to handle the severe SMR operating conditions (Waldron et al., 2001). Reaction parameters such as pressure, temperature and feedstock amount must be controlled to avoid carbon deposition as it reduces the catalyst activity. The schematic flow sheet for conventional SMR process is shown in Figure 2.1. Equations 2.4 and 2.5 show the endothermic reactions of methane with steam to form hydrogen, carbon dioxide and carbon monoxide.

$$CH_4 + H_2O \rightarrow CO + 3H_2 \qquad \Delta H^0{}_{298} = 206.2\ kJ/mol \qquad (2.4)$$

$$CH_4 + 2H_2O \rightarrow CO_2 + 4H_2 \qquad \Delta H^0{}_{298} = 165\ kJ/mol \qquad (2.5)$$

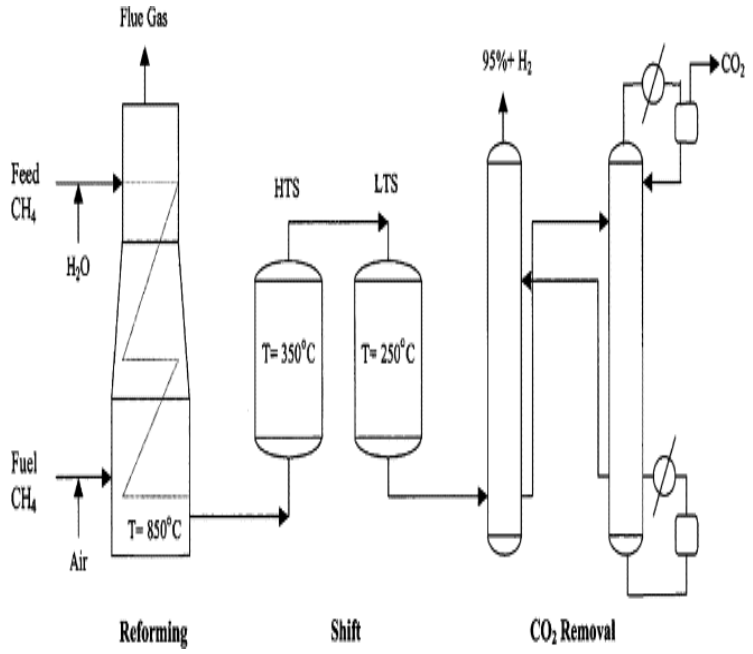

Figure 2.1. Flowsheet for the conventional SMR process, where HTS is the higher temperature shift reaction and LTS is the lower temperature shift reaction (Barelli et al., 2008).

The reformer products are then introduced to the shift reactor where the WGS reaction occurs, see equation 2.3. The WGS reaction coverts CO into easy separable CO_2 and increases the desired hydrogen yield. The shift reaction is reasonably exothermic, therefore the thermodynamic equilibrium decrease with increasing temperature. A low temperature is favoured for higher conversion. The WGS reaction is often accomplished in two stages. The first stage, is a high temperature shift reaction (HT) occurring at about 350-475°C where most of the CO is converted to CO_2 followed by the second stage of the lower temperature shift reaction (LT) is at 200-250°C (Hufton et al., 1999). Mixed oxides of chromium and iron oxide as a catalyst for WGS were first used by Bosh and Wild in 1912 (Twigg and Twigg, 1989). Iron oxide and chromium mixed catalyst converts 98% of the CO in to CO_2 at temperature 400-500°C. The iron based catalyst is not highly active at lower temperature; a copper based catalyst was proposed for lower temperature in the (LT) (Twigg and Twigg, 1989). For certain applications hydrogen should be purified depending on the specific application. Up to 99.999% hydrogen purity could be achieved by palladium membranes or pressure swing absorption (PSA) systems (Voss, 2005).

2.2.2. Steam reforming Catalysts

A catalyst is a material that accelerates a chemical reaction without being spent in the reaction (Richardson, 1999). The catalyst consists of one or more substances known as the active metal component and the support. Generally, a steam reforming catalyst is considered as a heterogeneous catalyst as the phase of reactants differs from the phase of catalysts (Richardson, 1999).

A practical catalyst for steam reforming should have number of objectives such as:

- Selectivity: promote the desired reactions, inhibit the side reactions and be resistant to contaminants and carbon deposition.
- Stability: the catalyst must be chemically stable under the process conditions to withstand the handling and thermal stresses results from process startup and shut down.

- Microstructure: the catalyst and support material are important parameters for the catalyst stability over prolonged periods.

2.2.3. Catalyst Deactivation

Catalyst deactivation is defined as a decline in catalytic activity over reaction time. It is considered one of the major problems in heterogeneous catalysis operation. Deactivation can occur by chemical or physical mechanisms. It can be classified into four groups, sintering, poisoning, fouling, and oxidation as discussed in sections 2.2.3.1 to 2.2.3.4.

2.2.3.1. Sintering

Sintering is considered as the deterioration of active surface due to changes in the molecular crystalline of either the support material or the active phase indicated by decreasing surface-to-volume ratio (Hennings and Reimert, 2008). Elevated temperature and the process conditions are the most important factors that enhance sintering (Men and Yang, 2012). The presence of sintering agents such as steam will accelerate the sintering process. Generally, sintering is an irreversible process therefore, it is better to be prevented (Sehested et al., 2006). Figure 2.2, shows the main conceptual models of sintering phenomenon. Temperatures below 0.3 to 0.5 of the melting point, in K, of the metal and support are recommended to prevent sintering (Karelovic et al., 2010). The value of 0.3 refers to the Huttig temperature, the point at which the atoms at defects gain mobility, while the 0.5 value indicates the Tamman temperature, which is the point at which atoms in the bulk become mobile.

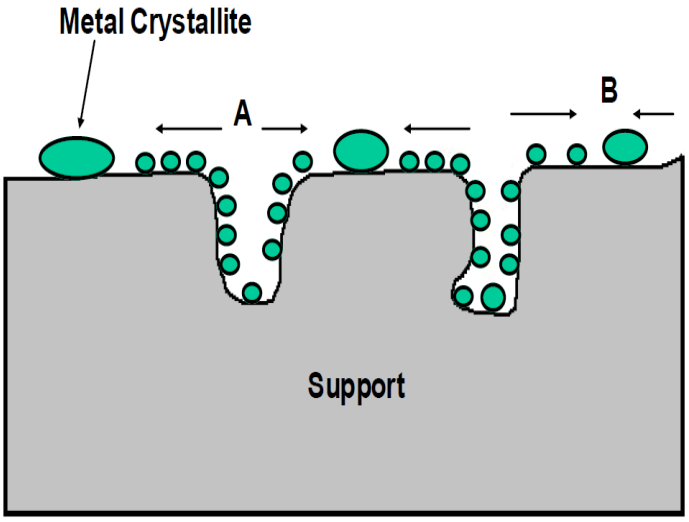

Figure 2.2. Two conceptual models of crystallite growth due to sintering, (A) by atomic migration where atoms detach from the metal crystallites and migrate to the surface where it is attached to the support particles (B) by particle migration where the support surface particles migrate and become attached to each other by collision (Bartholomew and Farrauto, 2011).

2.2.3.2. Poisoning

Irreversible chemisorption of the feed impurities onto the available active catalytic sites leads to a decline in the catalyst activity, this phenomenon is known as catalyst poisoning (Hennings and Reimert, 2008). Catalyst poisons block the active surface sites of the catalyst or alter the absorptivity of other species (Homsi, 2012). They also may cause changes in the catalyst geometric or electronic structure (Xie et al., 2011). For steam reforming catalysts, sulfur is considered the most severe poison. It presents in the form of H_2S, which is adsorbed by chemisorption on the metal surfaces, see equation 2.6 (Men and Yang, 2012).

$$H_2S + M \leftrightarrow M - S + H_2 \qquad (2.6)$$

The deposited sulfur can be removed by re-reduction and oxidation of the catalyst (Homsi, 2012). Figure 2.3 shows an example of poisoning of a metal catalyst by sulfur in ethylene hydrogenation process.

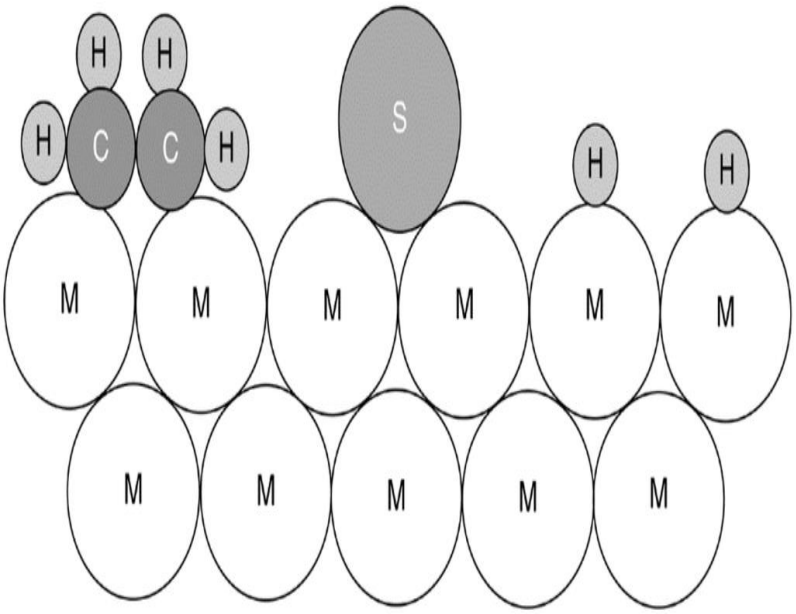

Figure 2.3. Sulfur atoms poison on a metal surface during ethylene hydrogenation (Bartholomew and Farrauto, 2011).

2.2.3.3. Fouling

Fouling is the coverage of active surface area or blockage of pores by deposit of species produced from the reacting fluid phase. The difference between poisoning and fouling is that fouling is considered physical (mechanical) deposition (Bartholomew, 2001). Severe fouling normally results in deterioration of catalyst particles, see Figure 2.4 (Bartholomew, 2001). Carbon or coke deposition in porous catalysts, combustion ashes and wear residues from process equipment are considered as fouling examples. Coke deposits may vary from graphite to carbon atoms, depending on the process parameters such as reaction conditions and catalyst type (Sehested et al., 2006). Optimisation of the process parameters results in a reduction in carbon deposition. To minimise carbon deposition, some studies suggest the adding of dopant materials normally from alkaline-earth metal or lanthanide group into reforming catalyst (Samoila et al., 2010, Martin and Duprez, 1995).

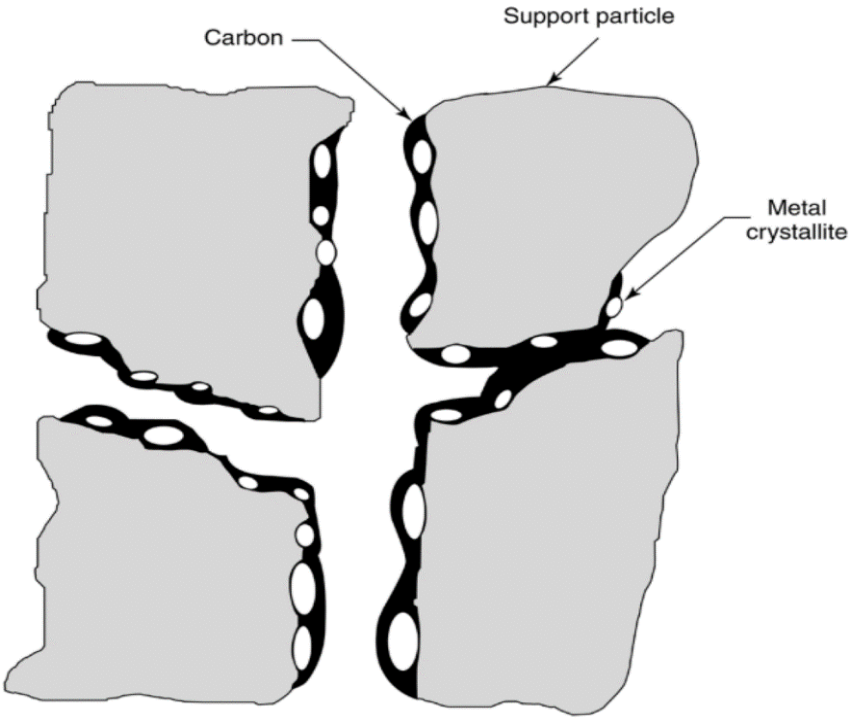

Figure 2.4. Pore plugging and crystallite encapsulation of a supported metal catalyst owing to carbon deposition (Bartholomew and Farrauto, 2011).

2.2.3.4. Oxidation

At high steam to carbon ratios, metal particles may be oxidised by steam, which reduces catalyst activity. Under normal steam reforming conditions, a sufficient amount of hydrogen for catalyst reduction will be produced and may reduce most of active metal surface during reaction (Homsi, 2012). Noble metals are not sensitive to oxidation (Hennings and Reimert, 2008). Table 2.2 summarises the different mechanisms of catalyst deactivation.

Table 2.2. Mechanisms of catalyst deactivation (Argyle and Bartholomew, 2015).

Mechanism	Type	Description
Poisoning	Chemical	Strong chemisorption of species on catalytic site, thereby blocking sites for catalytic reaction
Fouling from liquid	Mechanical	Physical deposition of species phase onto the catalytic surface and in catalyst pores
Thermal degradation (sintering)	Thermal	Thermally-induced loss of catalytic surface area, support area and active phase-support reactions
Vapour formation	Chemical	Reaction of gas with catalyst phase to form volatile compound
Vapour-solid and solid-solid reaction	Chemical	Reaction of liquid, support, or parameter with catalytic phase to produce inactive phase
Attrition/crushing	Mechanical	Loss of catalytic material due to abrasion. Loss of internal surface area due to mechanical induced crushing of the catalyst particle

2.2.4 Ethanol steam reforming (ESR)

Ethanol is a very attractive feedstock for steam reforming processes because it can be produced from different biomass sources by fermentation; it has a low toxicity and is easy to store and transport (Wang, 2012).

2.2.4.1. Ethanol Production

Ethanol is considered as a more environmentally acceptable fuel compared to petroleum hydrocarbons. Therefore, ethanol had a rapid growth of production and consumption in countries like Brazil, the United States (US) and Europe. Table 2.3 shows the world fuel ethanol production in 2014. Ethanol is expected to remain the dominant biofuel in 2018 with an estimated 1.81 million barrels per day of production.

Table 2.3. 2014 World Fuel Ethanol Production adapted from Renewable Fuels Association report,2015 (RFA, 2015).

Continent/country	Millions of Gallons
United States	14,300
Brazil	6,190
Europe	1,445
China	635
Canada	510
Thailand	310
Argentina	160
India	155
Rest of World	865

Numerous researches had been conducted for hydrogen production through ethanol steam reforming (ESR) (Haryanto et al., 2005, Xuan et al., 2009). ESR is an endothermic reaction in which 1 mole of ethanol produces 6 moles of hydrogen, see equation 2.7.

$$C_2H_5OH + 3\ H_2O \rightarrow 2\ CO_2 + 6\ H_2 \qquad \Delta H^{\circ}{}_{298} = +147.4\ kJ/mol \qquad (2.7)$$

The ethanol/steam reaction can go through different reaction pathways. C_2H_5OH complete conversion is important for the process economics. Catalysis has a crucial role to increase the rate of reaction (Armor, 1999). However, ethanol steam reforming can undergo several reactions. Table 2.4 shows the possible ethanol reaction mechanisms.

Table 2.4. Possible ethanol reaction mechanisms (Bshish et al., 2011).

Reaction	Equation	Remarks
Reforming in sufficient steam supply.	$C_2H_5OH+3H_2O\rightarrow 2CO_2+6H_2$	Ideal pathway, the highest hydrogen production.
Reforming in insufficient steam supply.	$C_2H_5OH+H_2O\rightarrow 2CO+4H_2$ $C_2H_5OH+2H_2\rightarrow 2CH_4+H_2O$	Undesirable products, lower hydrogen production.
Dehydrogenation to acetaldehyde (C_2H_4O), followed by acetaldehyde decarbonisation acetaldehyde steam reforming.	$C_2H_5OH\rightarrow C_2H_4O+H_2$ $C_2H_4O\rightarrow CH_4+CO$ $C_2H_4O+H_2O\rightarrow 3H_2+2CO$	Reaction pathways for hydrogen production in practice.
Dehydration into ethylene and water. Polymerization.	$C_2H_5OH\rightarrow C_2H_4+H_2O$ $C_2H_4\rightarrow$ polymeric deposits(Coke)	Undesired pathway, main source of coke formation.
Decomposition /cracking to CH_4 and H_2.	$C_2H_5OH\rightarrow CO+CH_4+H_2$	Coke formation, low hydrogen production.
Decomposition to acetone.	$2C_2H_5OH\rightarrow CH_3COCH_3+CO+3H_2$	
Reaction of decomposition products. Methanation.	$CO+3H_2\rightarrow CH_4+H_2O$ $CO_2+4H_2\rightarrow CH_4+2H_2O$	
Methane decomposition.	$CH_4\rightarrow 2H_2+C$	
Boudouard reaction.	$2CO\rightarrow CO_2+C$	
Water gas shift reaction (WGS).	$CO+H_2O\rightarrow CO_2+H_2$	Reduce coke formation, enhance hydrogen production.
Dissociative adsorption of water to form acetic acid.	$C_2H_5OH + H_2O \rightarrow CH_3COOH + 2H_2$	Water adsorption.

2.2.4.2. Catalysts for ethanol steam reforming

Development for an active catalyst for hydrogen production through ethanol steam reforming is an active research area. Noble metals such as rhodium (Rh), platinum (Pt), ruthenium (Ru), palladium (Pd) and iridium (Ir) have been intensively investigated, see Table 2.5. Rhodium (Rh) has been investigated through different studies and claimed to be active for ethanol steam reforming (Liguras et al., 2003, Cavallaro et al., 2003). Ethanol conversion over Rh/MgO catalysts was 100% at 650°C, with hydrogen selectivity of 92% (Frusteri et al., 2004). Rh/CeO_2 catalyst gave 100% hydrogen selectivity and >99% ethanol conversion at 800°C (Wanat et al., 2004). It was reported that ruthenium (Ru) has catalytic activity similar to Rh (Cavallaro et al., 2003, Kaddouri and Mazzocchia, 2004, JIANG et al., 2006). However, ethylene is produced in the reactions catalysed with Ru. Ethylene is then led to the formation of coke. Pt is used as a catalyst for the WGS reaction and increases the CO removal (Salge et al., 2005). Noble metals provide higher activity and stability but their high prices limit their wide commercial application (Salge et al., 2005).

Table 2.5. List of ethanol steam reforming results over noble metal catalyst (Kumar et al., 2014).

Catalyst Metal load /mol%	Support	Reaction Condition Steam/Ethanol molar ratio, S/E	Temp/ °C	Ethanol Conversion /%	Hydrogen selectivity /%	References
Rh (1)	γ-Al_2O_3	3	800	100	96	(Liguras et al., 2003)
Rh (3)	MgO	8.5	650	99	91	(Cavallaro et al., 2003)
Rh (1)	CeO_2	3	450	> 90	82	(Frusteri et al., 2004)
Rh (2)	CeO_2	8	450	100	69	(Erdőhelyi et al., 2006)
Rh (2)	ZrO_2	8	450	100	70.3	(Diagne et al., 2004)
Rh (2)	CeO_2-ZrO_2 (Ce/Zr =1)	8	450	100	70.3	(Diagne et al., 2002)
Ru (5)	γ-Al2O3	3	800	100	96	(Liguras et al., 2003)
Ru (1)	CeO_2	3	450	>90	57	(Erdőhelyi et al., 2006)
Pt (2.5) Ru (1)	γ-Al_2O_3	10	550	100	100	(Koh et al., 2008)
Pt (1)	γ-Al_2O_3	3	800	100	96	(Liguras et al., 2003)
Pt (0.5)	γ-Al_2O_3	4	340	95	40	(Basagiannis et al., 2008)
Pt (1)	CeO_2	3	300	100	39	(Ciambelli et al., 2010)
Pt (1.5)	CeO_2-ZrO_2 (Ce/Zr =4)	10	550	100	88	(Chen et al., 2008)
Pd (1)	γ-Al_2O_3	3	800	55	50	(Liguras et al., 2003)
Pd (5)	γ-Al_2O_3	3	650	100	95	(Goula et al., 2004)
Rh (6) Pt (2)	La_2O_3	7	700	100	78	(Cobo et al., 2013)
Ru	CeO_2/YSZ	5	550	100	86.6	(Ramos et al., 2012)

In the non-noble metals category, Ni has proven to be the best catalyst for the production of hydrogen by SR. The catalyst support can also strongly affect the catalytic performance by affecting the stability and dispersion of the metallic part and in some cases it may participate in the chemical reactions (Sánchez-Sánchez et al., 2007). Auprêtre et al.,(2002) investigated the effect of varying metal oxide supports on the activity of Rh and Ni catalysts (Auprêtre et al., 2002). They concluded that hydroxyl (–

OH) mobility increases on the catalyst surface and results in increasing the catalyst activity. The highly acidic nature of the catalyst support facilitates dehydration of ethanol (Fajardo and Probst, 2006) and leads to deactivation of catalysts by carbonaceous deposition, whereas the presence of basic sites on the support (La_2O_3, MgO, SiO_2) decreases coke deposition on the catalysts (Domínguez et al., 2010).

Addition of promoters (alkali and alkaline earth metals) reduces acidity (Hou et al., 2003). As MgO, CeO_2, hydrotalcites and ZnO are basic; they can prevent ethanol dehydration to ethylene, which leads to a reduction in coke formation. Ethylene is usually produced when Al_2O_3 is used as the catalyst support and results in coke formation (Domínguez et al., 2010). Addition of alkali elements to the catalyst can increase catalyst stability by partially decreasing the acidity. La_2O_3 was reported to promote dehydrogenation which leads to coke formation inhibition. ZrO_2, CeO_2–ZrO_2, $La_2O_2CO_3$, SiO_2, and Zeolite-Y were used with the active metals and have shown good selectivity.

Rh and Ni favored the C–C bond rupture and produced the best activity and selectivity to H_2 compared to all other metals (Bshish et al., 2011). Rh was reported to form methane during ESR but has relatively low efficiency in the SR of methane (Bshish et al., 2011). The higher capability of nickel to break O-H and C-C bonds promotes hydrogenation to form hydrogen gas which makes it the best option for ESR. It was reported more than 90% H_2 gas concentration was produced by using: Ru–Ni/CeO_2ZrO_2, Ru/TiO_2, Ru/Al_2O_3, Ru/MgO, Rh/CeO_2, Rh/MgO, Pd/Al_2O_3, CoxOy-Pd/Zeolite-Y, Ni/Ce1−x–ZrxO, Ni/ZnO, Ni/MgO, Ni/Ca–CeO_2–ZrO_2, Ni–CeO_2–ZrO_2, Ni–Fe/$La_2O_2CO_3$, Ni–Al_2O_3–ZrO_2, Ni/Cs-zeolite-Y and Ni–Cu/SiO_2 (Kumar et al., 2014). Machocki et al., 2010 had reported 100% ethanol conversion and 92.6% selectivity towards H_2 over nano-sized CeO_2 support (Machocki et al., 2010). Cobalt shows higher activity for ethanol steam reforming (ESR) but its sintering at high temperature decreases its applicability in ESR. Table 2.6 shows the conversion and hydrogen selectivity for non-noble catalysts

Table 2.6. List of ethanol steam reforming results over non-noble metal catalyst (Kumar et al., 2014).

Catalyst		Reaction Condition		Ethanol Conversion/ %	Hydrogen Selectivity/ %	References
Metal load /%	Support	Steam/ Ethanol molar ratio, S/E	Temp/ °C			
Ni (7)	SiO_2	3.7	600	97.1	82.6	(Calles et al., 2010)
Ni/Ce (7)/(10)		3.7	100	84.4		
Ni/Zr (7)/(10)		3.7	100	82.5		
Cu/Ni (2)/(7)	SiO_2	7.4	600	100	84.8	(Carrero et al., 2010)
Co (1)	V_2O_5	13	450	100	53.5	(Llorca et al., 2002)
	ZnO	13		100	71.3	
	La_2O_3	13		85	63.1	
	CeO_2	13		93.7	69.6	
	Sm_2O_3	13		85.9	64.7	
ZnO (30)	SiO_2	12	500	91.8	57.0	(Seker, 2008)
ZnO (50)	SiO_2	12		92.0	51.4	
ZnO (70)	SiO_2	12		92.3	61.0	
ZnO	-	12		91.7	58.6	
Ir (2)	CeO_2	3.2	650	100	75	(Zhang et al., 2008)
Ir (2)	Ce0.9Pr 0.1	3	500	100	72	(Wang et al., 2011)
Co (52) (molar ratio)	Zn =18	3	550	100	83	(Busca et al., 2010)
	Al=30	3				
Co (20)	CeO_2	3	600	100	66	(Lovon et al., 2012)
Co	CeO_2-N	5.5	420	100	92.6	(Machocki et al., 2010)
	ZrO_2-N	5.5			85.0	
	Ce/ZrO_2-N	5.5			91.9	
	Ce/ZrO_2-M	5.5			91.5	
Ni/Cu (1)/(3)	ZrO_2	-	600	100	84	(Sharma et al., 2013)

2.3. Iron oxide as a catalyst

Iron oxide (Fe_2O_3) is used as a catalyst for the water gas shift (WGS) reaction and the Fischer–Tropsch synthesis reaction. Moreover, iron oxide is also employed as a catalyst in a many of chemical processes such as ammonia synthesis, hydrogen sulfide removal and the dehydrogenation of ethyl benzene to styrene (Sun et al., 2005). Steam-iron process is also well known as an old commercial process, used for hydrogen storage/purification (Zafar et al., 2005, Mattisson et al., 2004, Geus, 1986). Iron oxide has many attractive features; it is inexpensive, non-toxic and shows good catalytic performance at higher operating temperatures. Stabilising iron oxides against sintering or agglomeration is a major challenge. Many studies investigated the possibility of modifying the iron oxide by addition of different metal oxides to promote its stability (Takenaka et al., 2005, Otsuka et al., 2003, Bohn et al., 2008). According to previous studies, co-addition of these materials could inhibit iron oxide sintering or agglomeration by decreasing the contact between the iron oxide particles during reaction and therefore decrease the loss of iron oxide catalytic activity. Table 2.7 summarises the function of the individual added components used in this study i.e. CaO, MgO and CeO_2.

Table 2.7. Function of the individual components in mixed prepared sorbent /catalyst.

Component	Function
Ceria (CeO_2)	The reducibility of Fe_2O_3 was enhanced by CeO_2 (Li et al., 2013, Pojanavaraphan et al., 2015, Miller et al., 2015)
Magnesium oxide (MgO)	MgO improves the oxygen transfer capacity of Fe_2O_3 (Miller et al., 2015, CHENG et al., 2010)
Calcium Oxide (CaO)	Eliminates presence of CO_2, and therefore increase hydrogen purity(Hufton et al., 1999)

Iron oxides were reported to exert an important catalytic role allowing the complete decomposition of ethanol in a temperature range of 600-750°C (Hormilleja et al., 2014). Setzer et al., 1984 recorded a patent of catalysts used for steam reforming prepared from at least 90% by weight iron oxide and various modifiers (Al_2O_3, K_2O, CaO, SiO_2) (Setzer et al., 1984).

2.4. Sorption enhanced steam reforming (SESR)

Conventional steam reforming has several disadvantages as discussed in section 2.2.1. Reduction of carbon deposition is considered one of the main challenges in conventional steam reforming. Carbon deposition leads to catalyst deactivation, mechanical failure and premature reactor shutdown. It is necessary that carbon be present in a form thermodynamically more active than graphite. To overcome these problems a reactor where reforming, CO_2 adsorption and water–gas shift reactions occur simultaneously has been proposed (Tiemersma et al., 2006, Chen et al., 2004), see Figure 3.9.

According to the Le Chatelier principle, the immediate removal of CO_2 results in a decrease in CO_2 partial pressure and accordingly the equilibrium moves towards more hydrocarbon conversion and therefore higher hydrogen yield. Sorbent regeneration to its oxide form consumes energy. However, many studies have reported that the necessary energy for sorbent regeneration is about 20–25% of the energy needed to drive conventional SMR (Lopez Ortiz and Harrison, 2001).

Among the different separation techniques, adsorption has gained increasing attention because of its potential for simple operation, low corrosiveness, and overall low cost (Choi et al., 2009). Adsorption is usually carried out in cycles of adsorption and desorption. Desorption is usually done either by temperature or pressure swing. An example of this application is pressure swing adsorption (PSA), which energy demands are in the range 160–180 kWh tonne^{-1} CO_2 recovered (Holling et al., 2013). Adsorbents for CO_2 capture can be categorized based on their chemical composition, structural characteristics or according to the adsorption mechanisms involved.

CO_2 uptakes are divided into two categories; physical and chemical. The physical absorbents are used for high pressure gas stream, whereas, the chemical CO_2 absorbents are generally used for low and moderate pressure gas stream. Akanolamines are the commonly used chemical adsorbents which usually used in the form of aqueous solutions. These chemical solvents include monoethanolamine (MEA), N-methyldiethanolamine (MDEA), and 2-amino-2-methyl-1-propanol (AMP) etc. Physical

adsorbents require less energy for adsorbents regeneration than the chemical adsorbents. N-Methyl-2-pyrrolidone (NMP), methanol and propylene carbonate (PC) are examples of the physical adsorbents. Under low pressure conditions, a mixture of physical and chemical sorbents enable the efficient capture of CO_2 (Thitakamol et al., 2007). The first process description of SESR was published in 1868 (Rostrup-Nielsen, 1984). Roger (1933) has issued a patent for methane steam reforming with the presence of a mixture of reforming catalyst and lime as CO_2 sorbent (Roger, 1933). Retallick (1963) used a fluidized-bed reactor for SESR (Retallick, 1963).

Numerous research has been conducted using calcium based CO_2 sorbents (Balasubramanian et al., 1999, Brun-Tsekhovoi et al., 1988, Han and Harrison, 1994, Lopez Ortiz and Harrison, 2001, Silaban et al., 1996). Brun-Tsekhovoi et al.,(1988) claimed they achieved energy saving of about 20% of the energy needed for conventional process (Brun-Tsekhovoi et al., 1988). Balasubramanian et al.,(1999) reported that in a single reactor contain CaO and reforming catalyst, 95% H_2 content (dry basis) gas mixture were produced (Balasubramanian et al., 1999). Hufton et al.,(1999) reported that methane conversion reached 82% (Hufton et al., 1999).He et al.,(2009) has studied the thermodynamic and experimental analysis of SESRE process with a CaO-based catalyst (He et al., 2009).

In this study, CO_2 capture experiments were conducted in the form of temperature swing adsorption and consisted of two steps: carbonation, regeneration. The developments of sorbents with good criteria for application in pre-combustion carbon capture include; selectivity, high absorption capacity, low cost and availability, good mechanical and thermal stability easily regenerated, adequate adsorption/desorption kinetics, small temperature gap between reaction and regeneration, long term multi-cycle use and thermal stability (Choi et al., 2009). To date, no sorbents satisfy all these requirements. The sorbents that are mostly studied in the literature for SESR can be divided into natural and synthetic sorbents such as hydrotolcite-like compounds, dolomite and limestone, CaO synthetic acceptor and ceramic acceptor as discussed in the 2.4.1.

2.4.1. CO_2 acceptor.

2.4.1.1. Dolomite and limestone

The most commonly used sorbent for sorption enhanced process hydrogen production is calcium oxide (CaO), which can repeatedly adsorb CO_2 over multiple carbonation/de-carbonation cycles as shown in equation 2.8 (Abanades and Alvarez, 2003)

$$CaO + CO_2 \leftrightarrow CaCO_3 \qquad \Delta H^0_{298} = 178.2\ kJ/mol \qquad (2.8)$$

CaO is found naturally in dolostone and limestone which are sedimentary rocks. Dolostone is composed of dolomite ($CaMg(CO_3)_2$) which contains MgO (Chen et al., 2009). The CO_2 capture capacities of dolomite and limestone ($CaCO_3$) have been studied by many researchers (Silaban et al., 1996, Bhatia and Perlmutter, 1983, Alvarez and Abanades, 2005). The main drawback of using dolomite and limestone as CO_2 acceptors is the dramatic drop of about 80% of the CO_2 adsorption capacity after 10-20 cycles of carbonation/de-carbonation reactions (Johnsen, 2006, Abanades and Alvarez, 2003, Grasa and Abanades, 2006). Although, the CO_2 uptake capacity per unit mass is greater in limestone compared to dolomite, dolomite was found to have a more stable capacity during multi-carbonation/de-carbonation cycling performance, the presence of MgO as inert material in the dolomite composition may be responsible for dolomite stability (Silaban et al., 1996, Han and Harrison, 1994).

2.4.1.2. Hydrotolcite-like compounds (HTLC)

HTLC are also well known as layered double hydroxides (LDH). They are classified into anionic and basic clays and have a typical composition of $Mg_6Al_{12}(OH)_{16}CO_3.4H_2O$ (Miyata, 1977). Recently, these materials are used in many applications such as catalysts, catalysts supports, decolorizing agents, ion exchangers, precursors, filters, industrial adsorbents and polymer stabilizer (Ding and Alpay, 2000b). These materials can chemisorb CO_2 at temperature between 673 and 773K (Ding and Alpay, 2000b). The latter researchers studied the equilibrium and kinetics of CO_2 adsorption on potassium promoted hydrotalcites. Their conclusion was that HTLC has low CO_2 adsorption capacity

under dry conditions (0.65mol CO_2/kg) at 673k. The capacity was increased by 10% in wet conditions independently of the water amount. Choi et al., 2009 reported that the CO_2 uptake capacity of hydrotalcites at temperatures of 200–500 °C ranged from 0.17 to 0.9 mmol g^{-1} (Choi et al., 2009). In multi-cycling operations there is a relatively rapid degradation in CO_2 adsorption capacity of ~30–40% at 673 K and higher drop rates were observed at higher temperatures (Ding and Alpay, 2000b). In spite of this rapid degradation and their relatively low CO_2 adsorption capacity, there is further investigation and optimisation in hydrotalcites formulation in order to understand the control factors that influence their CO_2 adsorption capacity (Hutson et al., 2004, Ebner et al., 2007).

2.4.1.3. Ceramic CO_2 acceptor

Lithium and sodium oxide have been proposed recently for CO_2 capture (Nakagawa and Ohashi, 1998, Ohashi and Nakagawa, 1998). Nakagawa and Ohashi, 1998 reported that lithium zirconate ($LiZrO_3$) has CO_2 adsorption capacity of 28.8 % at temperature 723-873k (Nakagawa and Ohashi, 1998). Li_4SiO_4 has high CO_2 absorption capacity at 700 °C in 100% CO_2 condition, but it has poor absorption kinetics at lower temperature. Li_4SiO_4 CO_2 uptake capacity could be promoted by addition of hetero-atoms. Many studies have been conducted to investigate the effect of addition of different dopants (López-Ortiz et al., 2005, Carvill et al., 1996). However, further investigation is needed to study the steam effect on CO_2 absorption capacity and its stability during adsorption/desorption multiple cycles (Ohashi and Nakagawa, 1998). Sodium based acceptors such as $NaZrO_3$ have been proposed as good alternatives for Li_2ZrO_3 and Li_4SIO_4. (López-Ortiz et al., 2005) studied the CO_2 adsorption of the three materials at 100% CO_2 and reported that Na_2ZrO_3 had the most favorable kinetics. In spite of the high adsorption capacity, stability and lower generation temperature of the ceramic acceptor, CaO shows more favorable thermodynamics than Li, and Na based mixed oxide and therefore, CaO is useful in the removal of lower CO_2 concentrations (López-Ortiz et al., 2005).

2.4.1.3. CaO synthetic adsorbents

It is known that after 10-20 carbonation/ de-carbonation cycles, natural CaO loses its CO_2 uptake capacity by 80% because of agglomeration and sintering of the CaO (Lopez Ortiz and Harrison, 2001). Bandi et al., 2002 claimed that CaO could preserve its microstructure over several carbonation and de-carbontion cycles by addition of an inert materials (Bandi et al., 2002).

Several studies were done to overcome the dramatic drop of CO_2 uptake capacity during cycling in the natural CaO-based acceptor. Many researchers have attempted to enhance CaO strength by the addition of various inert oxides. These include a variety of metal oxide additions to CaO such as Al_2O_3 (Feng et al., 2006, Gruene et al., 2011),Y_2O_3 (Derevschikov et al., 2011), MgO (Liu et al., 2010), $CaTiO_3$ (Wu and Zhu, 2010), $Ca_{12}Al_{14}O_{33}$ (mayenite) (Li et al., 2005), $Ca_9Al_6O_{18}$ (Zhou et al., 2012). Li et al., (2005) claimed that the incorporation of $Ca_{12}Al_{14}O_{33}$ into CaO providing a well-dispersed skeleton, which improves CaO cyclic stability and prevents agglomeration (Li et al., 2005). They claimed that their synthetic CaO had a capacity of 0.45 g CO_2/g CaO that did not degrade upon adsorption/desorption multi–cycles.Silaban et al., (1996) reported that dolomite was more stable than limestone over the CO_2 carbonation/de-carbonation cycles. MgO is a constituent of in dolomite (Ca Mg $(CO_3)_2$) and huntite (Ca Mg_3 $(CO_3)_4$ (Silaban et al., 1996). MgO disperses between CaO particles and provides a partition wall and thus prevents sintering since MgO does not react with CO_2 at temperatures over 400°C (Park and Yi, 2012b). Ceria (CeO_2) facilitates coke gasification under steam due to its high ability of oxygen storage and release which enable the mobility of CO_3^- (Wanat et al., 2004, Rusten, 2010). In addition to that, CeO_2 prevents the metal particles from sintering (Wanat et al., 2004).

Different preparation procedures have been established to integrate inert materials into CaO particles such as flame spray pyrolysis (Lu et al., 2008a, Koirala et al., 2012) and mixing (Zhou et al., 2012, Qin et al., 2012, Kierzkowska and Müller, 2013). However, there have been no study that report the addition of MgO and CeO_2 by the co-

precipitation method used in this work in order to enhance CaO characterisation as CO_2 sorbents for sorption enhanced ethanol reforming.

Table 2.8. Properties of some of high temperature CO_2 accepter (Ruthven, 1984).

Accepter	Capacity/ g CO_2/g sorbent	Stability	Kinetics	Regeneration Temperature [a]/ K
Dolomite	0.46	Poor	Good	1173
Limestone	0.79	Poor	Good	1173
$CaO/Ca_{12}Al_{14}O_{33}$	0.45[b]	Fair	-	1173
$CaO/J\text{-}Al_2O_3$	0.033[c]	Good	-	1173
Li_2ZrO_3	0.29	Fair	Fair/Poor	1020
Na_2ZrO_3	0.24	Fair	Good	1050
Li_4SiO_4	0.36	Fair	Fair	990
Hydrotalcite	0.029[d]	Fair/Poor	Good	PSR [e]

a.Equilibrium regeneration temperature at 1bar and 100% CO_2 (Metz et al., 2005)
b. Capacity reported by (Li et al., 2005)
c. Capacity reported by Feng et al (4.6% CaO, 90% reacted) (Feng et al., 2006)
d. Capacity reported by Ding et al (0.65 mol CO_2/kg) (Ding and Alpay, 2000a)
e. PSR: Pressure swing regeneration

2.5. CaO regeneration processes

CO_2 capture technology is based on adsorption/desorption cycling processes of the gas on solid material. Once the sorbent is saturated, a regeneration step is required. The gas–solid system thermodynamic behaviour depends on temperature and pressure, see Figure 2.5 (Hedin et al., 2013). The adsorption isotherms (p, T) show that increasing pressure results in an increase in the amount of gas adsorbed (n). On the other hand, as the adsorption is an exothermic phenomenon, the amount of gas adsorbed drops with the increase of temperature. Therefore, sorbents' regeneration technologies depend on the variations of temperature and pressure (Hedin et al., 2013). For commercial purposes, a few cyclic adsorption processes have been used for CO_2 regeneration (Ko et al., 2005), such as temperature swing adsorption (TSA), pressure swing adsorption (PSA), and vacuum swing adsorption (VSA).

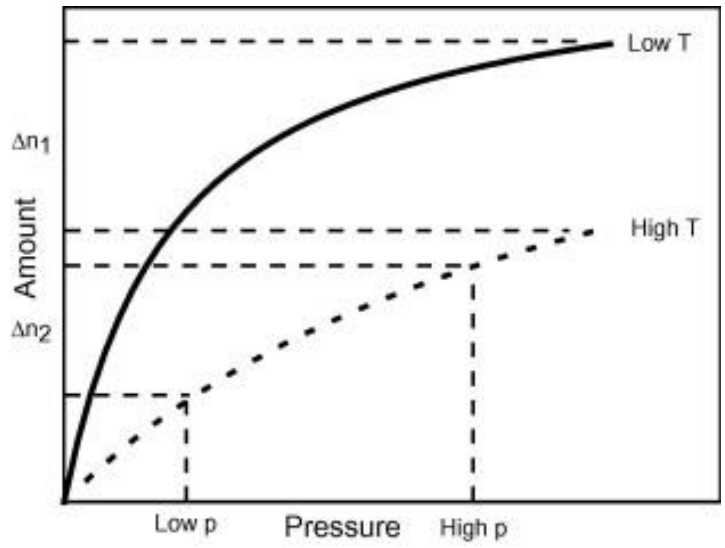

Figure 2.5. Adsorption isotherms illustrate gas–solid system dependence on temperature and pressure, Δn_1 is the high quantity of the adsorbed gas, Δn_2 is the low quantity of the adsorbed gas (Hedin et al., 2013).

2.5.1. Temperature swing adsorption (TSA)

TSA is based on the fact that sorbent CO_2 uptake capacity at any given partial pressure at higher temperature is lower than at lower temperatures (Ruthven, 1984). Generally, CO_2 will be adsorbed on the sorbent surface when the temperature is high enough. However, it is important to increase the temperature only to the extent that it does not lead to loss in the adsorption capacity (Ruthven, 1984).

Introduction of heat in to the adsorbed species could be achieved by heating part of the feed gas, or separate inert gas, or part of the product gas or the ambient air (Ruthven, 1984). TSA processes are used exclusively when the concentration of the adsorbates is low (Humphrey, 1997). In commercial application, it is necessary to purge a hot gas stream to sweep out the desorbed component (Ahner and Häring, 2008). Compared with pressure swing adsorption and vacuum pressure swing adsorption, the high energy consumption needed for heating is considered one of TSA drawbacks. In addition to that, TSA cycle usually takes longer time than PSA because of the time to exchange thermal energy in CO_2 adsorption–desorption processes (Bonjour et al., 2005, Pirngruber et al., 2009).

2.5.2. Pressure swing adsorption (PSA)

PSA technology is based on the principle that certain gaseous species are adsorbed preferentially on solid sorbents at high partial pressure and released when the pressure is decreased (Ko et al., 2005). PSA operation consumes lower energy compared with other technologies as it can be operated at ambient temperature. Moreover, a PSA unit is simple and its operation time is faster than that of TSA. PSA operation was reported to adopt the Skarstrom cycle stages (Kärger and Ruthven, 1992); feed pressurization, adsorption in higher pressure, pressure decrease, and purge.

During the 1960s, a stage of pressure equalization was used to save re-pressurization energy after purging (Tien, 1994, Basmadjian, 1996). Since the 1980s, many studies have been conducted in order to enhance the PSA regeneration efficiency (Do, 1998, Thomas and Crittenden, 1998, Talu, 1998). PSA process description was reported in a Patent (Shin and Knaebel, 1987, Yee and Puri, 1995). Figure 2.6 shows a basic PSA setup, which operates as follows: the pressurized feed gases are introduced into column A which contains the solid adsorbent bed such as activated carbon and zeolites. In column (A) at pressure (P1) not all the components in the feed gas are adsorbed. The non-adsorbed components leave column (A) as a product gas to column (B). The ambient pressure (P_2) is allowed in column (A) which decreased the equilibrium adsorption and accordingly the adsorbates are desorbed and purged out as an exhaust gas. Gas concentration is monitored from the gas leave column (A). When column (A) reaches saturation, the de-sorption process is transferred to column (B). This cycle is repeated continuously to obtain a constant gas flow of target gases (Ruthven, 1984).

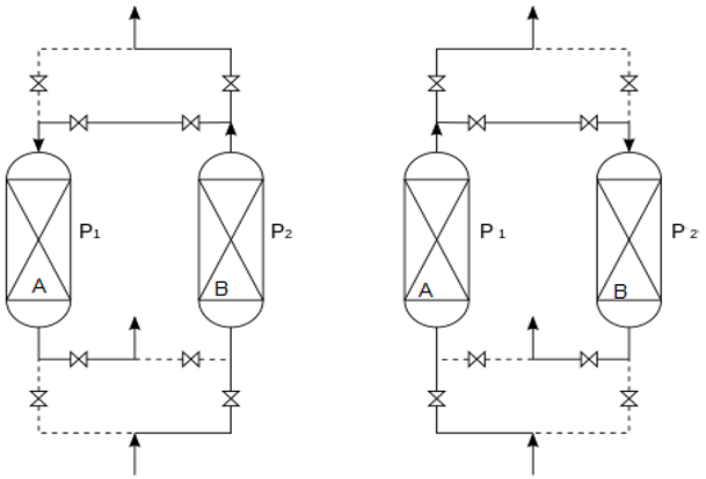

(A) (B)

Figure 2.6. Schematic drawing of PSA ,P_1 is the high pressure and P_2 is low pressure in first cycle (A),then P_1 is the low pressure and P_2 is high pressure in cycle (B) after column (A) saturation (Ruthven, 1984).

Many studies investigated the removal of CO_2 from gas mixture using PSA technique (Yang et al., 1993, Chue et al., 1995). Schell et al., 2009 have reported a CO_2 recovery of 99.8-99% (Schell et al., 2009). PSA units can recover high purity CO_2 streams, which makes PSA a preferable technology in pre-combustion carbon capture compared to TSA (Ebner et al., 2007). Table 2.9 provides summarize comparison between TSA and PSA.

2.5.3. Vacuum Swing Adsorption (VSA)

The primary difference between VSA and PSA is that VSA uses ambient temperatures and pressures, whereas PSA uses higher pressure. A vacuum is used in VSA to draw the gas mixture. VSA is simple and has lower power consumption (Kwon et al., 2011, Plaza et al., 2007). Xiao et al., 2009 obtained a CO_2 product stream with a purity of 95% using VSA in the integrated gasification combined cycle (IGCC) process (Xiao et al., 2009).

Table 2.9. Comparison factors between TSA and PSA (Ruthven, 1984).

Method	Advantage	Disadvantage
Thermal swing adsorption (TSA)	-Good for strongly adsorbed species, small change in temperature, T gives large change in absorbate load q. -Desorbate may be recovered at high concentration. -For gases and liquids.	-Thermal aging of adsorbent. -Heat loss means inefficiency in energy usage. -Unsuitable for rapid cycling so adsorbent cannot be used with maximum efficiency. -In liquid systems high latent heat of interstitial liquid must be added.
Pressure Swing adsorption (PSA)	-Good where weakly adsorbed species is required in high purity. -Rapid cycling.	-Very low pressure may be needed. -Desorbate recovered at low purity.

2.6. Alternative captures technologies

2.6.1. Membranes for CO_2 removal

Gas mixture components could be separated by passing through a membrane barrier based on their rates of permeation (Kohl and Nielsen, 1997). Different gases have different rates of permeation. Some permeate quickly such as helium, hydrogen, hydrogen sulphide, water vapour and carbon dioxide. Others permeate much more slowly such as nitrogen, carbon monoxide, ethane and methane. Accordingly, membranes can separate fast gases from slow gases.

Membranes are generally classified into either organic (polymers) or inorganic membranes. Polymer membranes are further classified into rubbery polymers and glassy polymers. The difference between them is that rubbery is above the glass-transition temperature whereas glassy polymer is below the glass-transition temperature (Scholes et al., 2010, Rodriguez et al., 2014). The first use of membranes for carbon dioxide removal application was in 1981. The main membrane CO_2 capture application is purification of the natural gas where CO_2, first dissolves then diffuses through the membrane. In natural gas purification process, H_2O and H_2S have faster removal rate

compared to methane and higher hydrocarbons (Fried, 2014, Murphy et al., 2009). Application of large scale membrane for gas separation has been limited because of its stability and selectivity (Scott and Hughes, 1996). Poor selectivity led to higher operating cost while unstable membranes affect the unit capital cost (Scott and Hughes, 1996). Membrane thickness is necessary for the operating strength. Developing efficient membranes with layers on the order of 1μm is the main challenges in membrane systems. Moreover, high pressure operation causes membrane plasticisation and compaction in most polymeric membranes (Wind et al., 2004). Many studies were conducted in order to study novel fixed-site-carrier (FSC) membranes and reported high performance for CO_2 removal from natural gas (Deng et al., 2009, Kim et al., 2013, Kim et al., 2012).

2.6.2. Ionic Liquids (ILs)

ILs are salt-like materials that have a melting point less than 100 °C. They consist of an cation and an anion. The cations are typically organic large size molecules such as phosphonium, imidazolium and pyridinium. While the anions are usually small inorganic molecules such as PF^{6-}, $BF^{4-,}$ $CF_3SO_3^-$ and Cl^- (Sánchez et al., 2011). Ionic liquids have been typically used in electrochemistry and organic chemistry until the late 1990s (Hussey, 1988, Welton, 1999, Wasserscheid and Keim, 2000). Freemantle, 1998 studied the possibility of using ionic liquids as solvents (Freemantle, 1998). However, their high cost has limited ILs industrial application (Commercialization, 2004). Recently, using ionic liquids for CO_2 capture has attracted growing attention (Sánchez et al., 2011, Dai et al., 2015). However, for CO_2 capture at high temperatures and pressure, such as pre-combustion capture and gasification, ILs exhibit poor performances (Plazinski et al., 2009).

2.7. Summary

Steam reforming is a process where a hydrocarbon is catalytically converted into hydrogen and carbon dioxide. The literature review shows the different modes of catalyst deactivation and studies carried out for catalyst development for conventional steam reforming processes in order to enhance the catalyst capacity and selectivity towards hydrogen production. Iron oxide has been used as a catalyst in different processes such as the water gas shift (WGS) reaction and the Fischer–Tropsch (FT) process. A specific survey of ethanol steam reforming, and the catalyst used for this process, were presented.

The sorption enhanced steam reforming (SESR) improves the process of the conventional steam reforming. This improvement is referred to as the removal of CO_2 from the products gas phase by a CO_2 accepter which results in production of a high purity hydrogen gas stream. Most of the studies on high temperature CO_2 accepters have been related to the use of the natural CaO precursor dolomite and limestone. However, these compounds suffer from large decay of the CO_2 capture capacity (80%) after 10-20 cycles of multiple carbonation/de-carbonation reactions. The possibility of CaO- based sorbent enhancement of by addition of inert materials had been investigated extensively. Other CO_2 accepters for SESR, their limitations and the regeneration methods of these materials had also been discussed.

Finally, alternative CO_2 capture technologies were overviewed. Based on the literature review, the synthesis of CaO- based sorbent using MgO and CeO_2 as the modification elements, in order to enhance CaO capacity and stability during multiple carbonation /de-carbonation reaction cycles, has been basis of this work. Furthermore, the possibility of using iron oxide as a catalyst in sorption enhanced ethanol steam reforming is also investigated.

CHAPTER THREE

Experimental Methods

3.1. Sorbents/catalyst preparation

The co-precipitation method below modified after (Park and Yi, 2012a) was used to prepare the synthetic CaO-based sorbent consisting of oxide phases of CaO ,MgO and CeO_2. Calcium nitrate tetrahydrate $Ca(NO_3)_2.4H_2O$ (≥99.0% purity, Sigma–Aldrich), magnesium nitrate hexahydrate $Mg(NO_3)_2{\cdot}6H_2O$ (98.0-102.0% (KT) purity, Puriss. p.a., ACS reagent, Sigma–Aldrich) and cerium(III) nitrate hexahydrate $Ce(NO_3)_3.6H_2O$ (99% trace metals basis, Aldrich) were dissolved in a mixture of isopropyl alcohol (IPA) (≥99.7% purity, Sigma–Aldrich) and distilled water at room temperature. Several Ca xMg yCe z samples were prepared, with the values x, y and z representing the molar percentage of the corresponding oxides loaded in the sample, see Table 3.1. The resultant solution was stirred for 1h at 75°C on a hot plate magnetic stirrer inside a fume cupboard and then evaporated at 350°C, see Figure1.1.

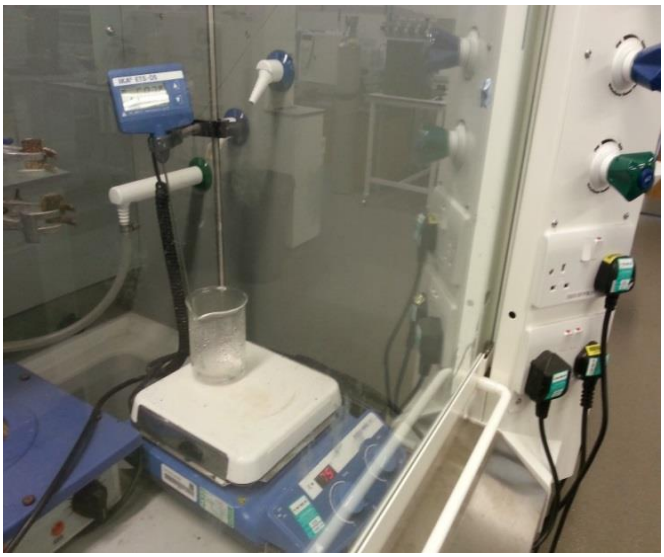

Figure 3.1. Sorbents preparation by co-precipitation method using a hot plate magnetic stirrer inside a fume cupboard.

Table 3.1. Adsorbents preparation parameters values.

Sample		Calcium nitrate tetra-hydrate ($Ca(NO_3)_2.4H_2O$)/g	Magnesium nitrate hexa-hydrate ($Mg(NO_3)_2{\cdot}6H_2O$)/g	Cerium(III) nitrate hexa-hydrate ($Ce(NO_3)_3.6H_2O$)/g	Isopropyl alcohol (C_3H_7O)/ml	Distilled water (H_2O)/ml
Ca4Mg2Ce1	3.7:1.7:1	10.00	5.00	5.00	10.00	50.00
Ca6Mg2Ce1	5.5:1.7:1	9.00	3.00	3.00	8.00	37.00
Ca3Mg2Ce1	2.8:1.7:1	6.00	4.00	4.00	7.00	35.00
Ca2Mg2Ce1	1.8:1.7:1	5.00	5.00	5.00	8.00	37.00
Ca1Mg2Ce1	0.6:1.7:1	2.00	6.00	6.00	7.00	35.00
Ca7Mg2Ce1	7.4:1.7:1	8.00	2.00	2.00	6.00	30.00
Ca11Mg2Ce1	11.0:1.7:1	12.00	2.00	2.00	8.00	40.00
Ca3Mg2Ce1	2.6:1.7: 1	8.00	6.00	6.00	10.00	50.00
CaO	100	10.00	0	0	5.00	25.00

3.2. Determination of the calcination temperature

Calcination leads to thermal decomposition, phase transition and removal of unstable anions and cations which were not desired in the final sorbent. However, the calcination procedure might have affected the sorbent activity so an optimum is desired. In order to select the optimum temperature for sorbents calcination, a thermogravimetric analyser (TGA) was used. The calcination of samples was carried out using a SDT-Q600-TA instrument. 20-50mg of sample was heated in an alumina crucible at a heating ramp rate of 20°C/min from 25°C up to 800°C.

3.3. Carbonation/de-carbonation test

About 20-50mg of sample was placed in a thermogravimetric analyser (TGA) (SDT-Q600-TA instrument) for the carbonation/de-carbonation cyclic tests. The sample was heated to 700°C at a heating rate of 20°C/min under nitrogen (N_2) atmosphere with flow

rate of 100 ml/min. When the temperature was achieved and stabilised, the carbonation reaction step was conducted, the samples were exposed to 100% carbon oxide (CO_2) at a flow rate of 100 ml/min for 60 min, see Figure 3.2.

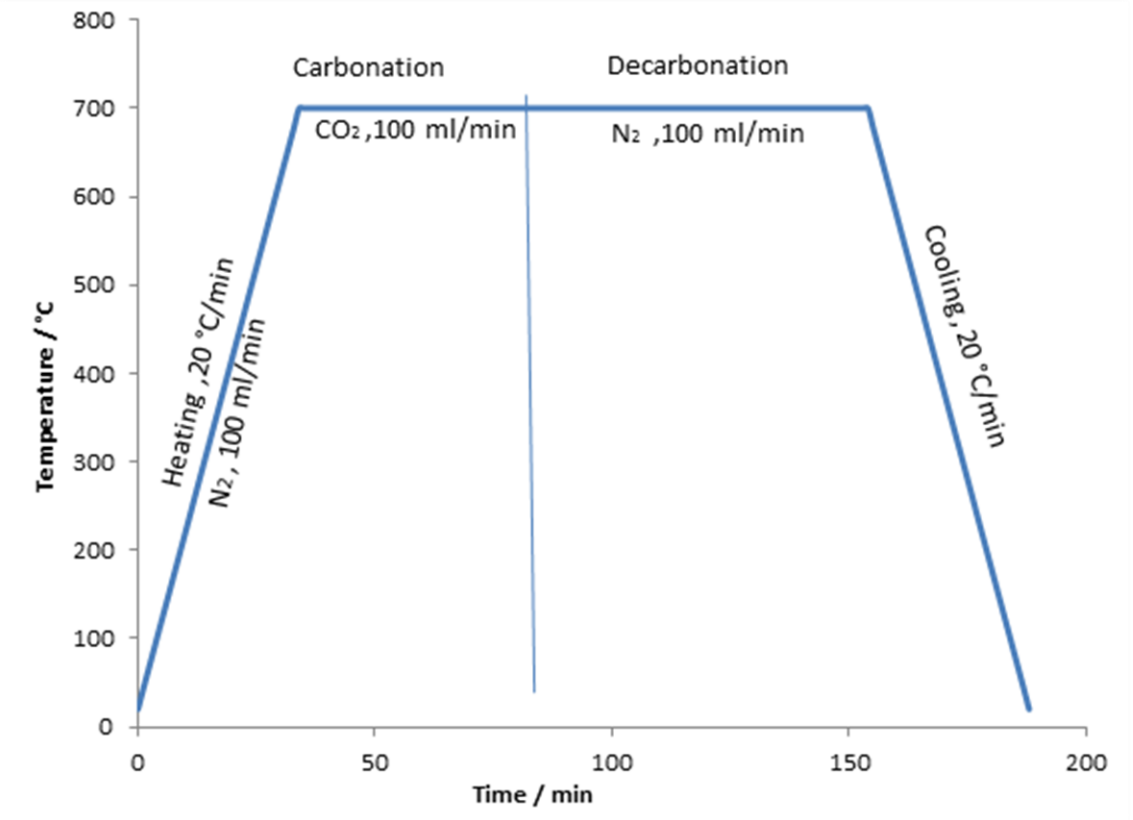

Figure 3.2. Sorbent carbonation/de-carbonation reaction conditions.

The CO_2 uptake capacities of sorbents expressed as the increase in the weight percentage as given in equation (3.1):

$$Adsorption/Absorption \quad capacity \quad (w\%) = \frac{(W_t - W_0)}{W_0} \tag{3.1}$$

It can also be defined as molar ratio as shown in equation (3.2):

$$Molar\ uptake\ capacity = \frac{Mole\ of\ CO_2\ absorbed/adsorbed}{Mole\ of\ CaO\ in\ sorbent\ mixture} \tag{3.2}$$

The carbonation conversion α expressed as.

$$\alpha = \left(\frac{(W_0 - W_t)}{(W_0 - W_\infty)}\right) \quad (3.3)$$

where:

W_0 : is the initial sorbent weight,

W_t : is the sorbent weight at time t,

W_∞ : is the final weight

3.4. Kinetics of CO_2 uptake reaction

The fundamental aim of the study of CO_2 uptake kinetics was to explain the complex mechanisms of carbonation reaction and relating that with the physical and chemical properties of the sorbents. Generally, the solid state reactions have a heterogeneous nature (Khawam, 2007). The solid-state reaction rate coefficient involves geometric changes of the formed products. A number of mathematical methods has been proposed in order to investigate the kinetic of the solid state reaction data such as single heating rate, model fitting and iso-conversional method (Khawam, 2007). In this study, model fitting methods are used to fit the data collected from the thermogravimetric analysis. Sestak and Berggren (1971) proposed a general mathematical form of the kinetic models, equation 3.4 (Šesták and Berggren, 1971).

$$g(\alpha) = \alpha^m \ (1-\alpha)^n \ ((-\ln(1-\alpha))^p \quad (3.4)$$

where:

m, n and p : are constant.

α : is the carbonation conversion.

Different models can be derived by assigning values for m, n and p (Khawam, 2007). Three models were applied to study the kinetics and mechanisms of CO_2 uptake. The kinetics equations of the studied models were listed and summarized in Table 3.2.

3.4.1. Surface chemisorption model (SC)

The SC model is considered the simplest model and it is similar to the homogenous kinetic models where the reaction rate is proportional to the reactant concentration (Khawam, 2007). Surface chemisorption indicates the presence of a chemical interaction between the sorbent surface and the adsorbate, in this case the conversion fraction (α) was proportional to the CO_2 uptake time. The chemisorption of CO_2 is the rate limited step. SC model was derived from the general equation (3.5)

$$\frac{d\alpha}{dt} = k\ (1-\alpha)^n \qquad (3.5)$$

where:

$\frac{d\alpha}{dt}$: is the reaction rate

k : is the reaction rate constant

t : is the reaction time

If $n = 0$ then, $\frac{d\alpha}{dt} = k$ by arranging variables and integrating equation (3.6) (Khawam, 2007)

we get

$$\text{SC}: \ \alpha = kt \qquad (3.6)$$

3.4.2. Contracting volume (CV) model

In the CV model, nucleation commences on the surface of the sorbent with continuous growth of the new product phase towards the sorbent bulk. According to the sorbent crystal shape, different reaction models can be used. Generally, equation (3.7) is applied for any crystal shape.

$$r = r_0 - k_t \tag{3.7}$$

where:

r : is the crystal radius at time t.

r_0 : is the crystal radius at time t_0.

k : is the reaction rate constant.

For sorbent particle with cylindrical shape, equation 3.8 can be applied

$$CV2:1-(1-\alpha)^{1/2} = kt \tag{3.8}$$

For sorbent particle with cubical or spherical shape, equation 3.9 can be applied

(Małecki et al., 1985)

$$CV3:1-(1-\alpha)^{1/3} = kt \tag{3.9}$$

The reaction rate is limited by the progression of the interface of new product towards the sorbent bulk. Equation (3.10) was proposed by Ginsling and Bounstein (1950) with assumption that the shape of the solid particles are spherical (Ginstling and Brounshtein, 1950). This equation describes three-dimension interface movement toward the sorbent bulk with a growth velocity decreasing with time (Meng, 2011). The diffusion of the reactants within the solid bulk is the reaction rate limiting.

$$CV2/3:1-(2\alpha/3)-(1-\alpha)^{2/3} = kt \tag{3.10}$$

3.4.3. Johnson-Mehl-Avrami (JMA) model

The nucleation and growth models such as JMA model can be employed to different solid- state reactions. Johnson, Mehl and Avrami (Selvam et al., 1986b) proposed a model based on the nucleation of a new phase initiates randomly along two or three crystallographic axes either on the surface (2D nucleation) or in the bulk of the sorbent (3D nucleation) as given by equations 3.11 and 3.12 respectively (Khawam, 2007). The rate of the new phase growth is independent of time and controlled by temperature (Liang et al., 1999a). The random nucleation and moving of the nuclei of the new product is the rate-limiting step assuming that the adsorbate had a rapid diffusion.

$$JMA2:[-\ln\ (1-\alpha)]^{1/2} = kt \tag{3.11}$$

$$JMA3:[-\ln\ (1-\alpha)]^{1/3} = kt \tag{3.12}$$

Table 3.2. Kinetic equations in different situations; SC: Surface reaction model, JMA: Johnson-Mehl-Avrami model, CV: Contracting volume model (Meng, 2011, Khawam, 2007)

Kinetic equation	Situation description	Rate controlling process
$\alpha = kt$	SC model: Surface reaction model (chemisorption).	The chemisorption of the gas.
$[-\ln\ (1-\alpha)]^{1/3} = kt$	JMA model: three dimensional growth of existing nuclei with constant velocity of $CaO/CaCO_3$ interface movement.	Random nucleation, Avrami equation, JMA2.
$[-\ln\ (1-\alpha)]^{1/2} = kt$	JMA model: two dimensional growth of existing nuclei with constant velocity of $CaO/CaCO_3$ interface movement.	Random nucleation, Avrami equation, JMA3.
$1-(1-\alpha)^{1/3} = kt$	CV model: three dimensional growth of existing nuclei with constant velocity of $CaO/CaCO_3$ interface movement.	Phase boundary reaction, spherical symmetry.
$1-(1-\alpha)^{1/2} = kt$	CV model: two dimensional growth of existing nuclei with constant velocity of $CaO/CaCO_3$ interface movement.	Phase boundary reaction, cylindrical symmetry.
$1-(2\alpha/3)-(1-\alpha)^{2/3} = kt$	CV model: three dimensional growth of existing nuclei with decreasing velocity of $CaO/CaCO_3$ interface movement, i.e. diffusion controlled.	Three dimensional diffusion, spherical symmetry: Ginstling – Brounshtein equation.

3.5. Sorbent characterisation techniques

3.5.1. X-ray diffraction (XRD)

The microstructures of the sorbents were investigated both before and after CO_2 uptake using X-ray diffraction. The geometry of the interaction between X-rays and sample crystallites is linked to the geometry of the crystal structure via Bragg's law (Klug and Alexander, 1954)

$$n\lambda = 2d\sin\theta \tag{3.13}$$

where:

n : the order of diffraction.

λ : wavelength/nm.

d : the distance between planes of atoms in a crystallite.

θ : The angle between the incident and scattered X-ray.

XRD patterns were recorded by means of a Bruker-AXS D8 Advance diffractometer. It has a Cu-anode X-ray tube (at 40 kV & 35 mA), a Göbel Mirror (parallel beam optics), θ / θ geometry, sample rotation, a diffracted beam Soller-slit collimator (0.12º), and a scintillation counter X-ray detector. The sample were scanned at room temperature with Bragg-Brentano geometry, 2θ over a range of 5º to 80º, with a step size of 0.020° and a step time of 2s. The collected sample data was compared with data base diffraction patterns in the JCPDS-ICDD Powder Diffraction File (Faber and Fawcett, 2002). Data were analysed using Bruker's Eva software. 0.3–0.5 g of the sample was packed into an aluminum sample holder and then compressed lightly with glass sheet to make it. For samples after CO_2 uptake the ground powder were packed in a perspex sample holder and tape was applied to seal the samples.

Energy-dispersive X-ray spectroscopy (EDX) can provide information about the size and level of microstrain within the crystallites. The mean crystal size of material could be

calculated from the broadening of the X-ray diffraction peak, measured at one half the heights. The grain size (t) was calculated from the 100% diffraction peak full width at half maximum (FWHM) by using Scherrer equation, as given by equation (3.14) (Patterson, 1939, Klug and Alexander, 1954).

$$t = \frac{0.9 \times \lambda}{b_{size} \times \cos\theta} \tag{3.14}$$

where:

t: Crystallite size/ nm.

λ: X-ray wavelength/nm.

b_{size}: The peak width/degree.

θ: The Bragg angle /degree.

The experimental total line broadening equation is used for b_{size} driven as shown in equation (3.15):

$$b_{experimental} = b_{size} + b_{instrument} + b_{strain} \tag{3.15}$$

where:

$b_{experimental}$: The total line broadening (full width half maximum, FWHM).

$b_{instrument}$: Instrument constant ($b_{instrument}$= 0.13)

$$b_{size} = b_{experimental} - (b_{instrument} + b_{strain}) \tag{3.16}$$

Assuming b_{strain} =0, therefore:

$$b_{size} = b_{experimental} - b_{instrument} \tag{3.17}$$

3.5.2. Scanning electron microscopy (SEM)

SEM is a type of electron microscope, which focuses a beam of electrons on sample surface in order to produce images of the scanned sample. The interaction between the electrons and the atoms produces signals which give information about the sample's surface topography. This interaction results in different emissions including secondary electrons (SE), backscattered electrons (BE) and X-rays.SE offer the best resolution for the surface topography of the sample, although lower resolution, there is signal attenuation dependent on how light the element is for the backscattered electrons. The X-rays emitted are a result of elastic collisions of the electron beam with the sample, providing information about its elemental composition.

The sample volume is also responsible of the production of backscattered electron (BSE), secondary electron (SE) and X-rays, the different shapes are known as interaction volume. The shapes ranges within the specimen vary from a semi-circle to a tear-drop as shown in Figure 3.3. A Philips XL-30 scanning tungsten electron gun microscope is fitted with an Oxford Instruments INCA-EDX microanalysis system, a modern Si (Li) detector and ultra-thin entrance window for detection of elements down to boron (Z=5), was used to examine surface topography and morphology. The analysis software includes multi-element digital X-ray mapping, a quantitative elemental analysis program and line scan programs. The standard digital image size is 340 kb with Pixel format: 712 x 484/TIF. The powder samples were put on a conductive carbon tab over an aluminium disc and then coated with platinum prior to introduce to the microscope chamber.

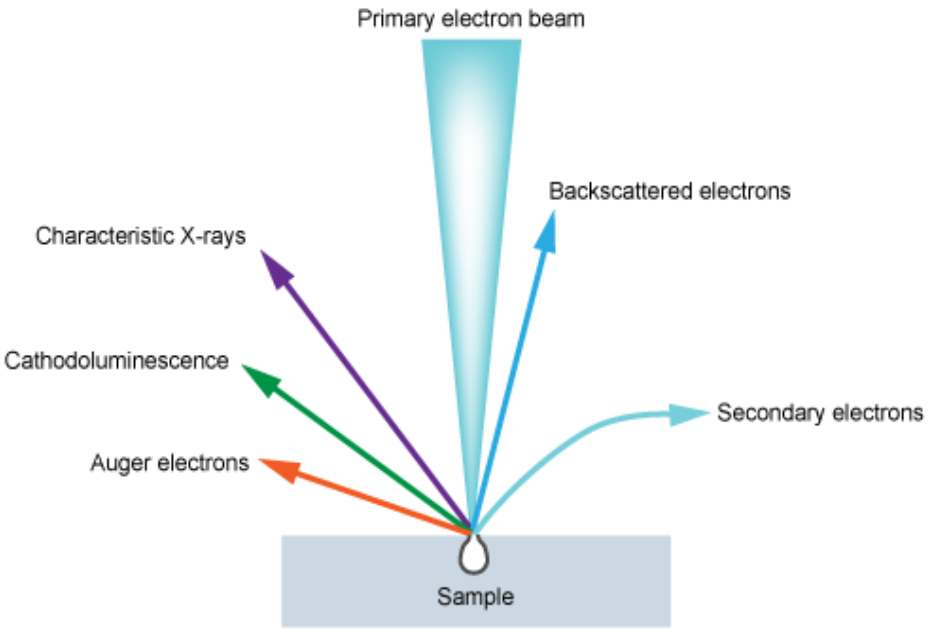

Figure 3.3. The tear-drop model of the electron interaction volume and the volume/depth from which the different signals collect (MyScope, 2015).

3.5.3. Surface area measurement.

The main method of surface area measurement was by physisorption of particular gas onto the adsorbent surface. The adsorption was achieved when a certain component called (adsorbate) in a gas mixture transfers to the surface of a solid called (adsorbent) whereas the others remain in the gas stream. Physisorption is a weak interaction, therefore there is need to minimize the thermal energy of the adsorbate and therefore, physisorption is conducted at low temperature. The attractive force which acts between the adsorbate and the solid surface and known as Van der Waals forces (Rouquerol et al., 2013). The relative pressure and the available solid surface are responsible of the gas physisorption as it is considered non-selective sorption filling the solid layers in order. The adsorbent surface area could be estimated whenever the first layer been filled. The adsorbed volume of adsorbate is proportional to the total surface area of the adsorbent when the mono-layer is saturated. Adsorption/desorption plot are known as the adsorption isotherm. Physisorption isotherms plots are divided into six categories, I-VI as shown in Figure 3.4 (Condon, 2006, Sing and Gregg, 1982).

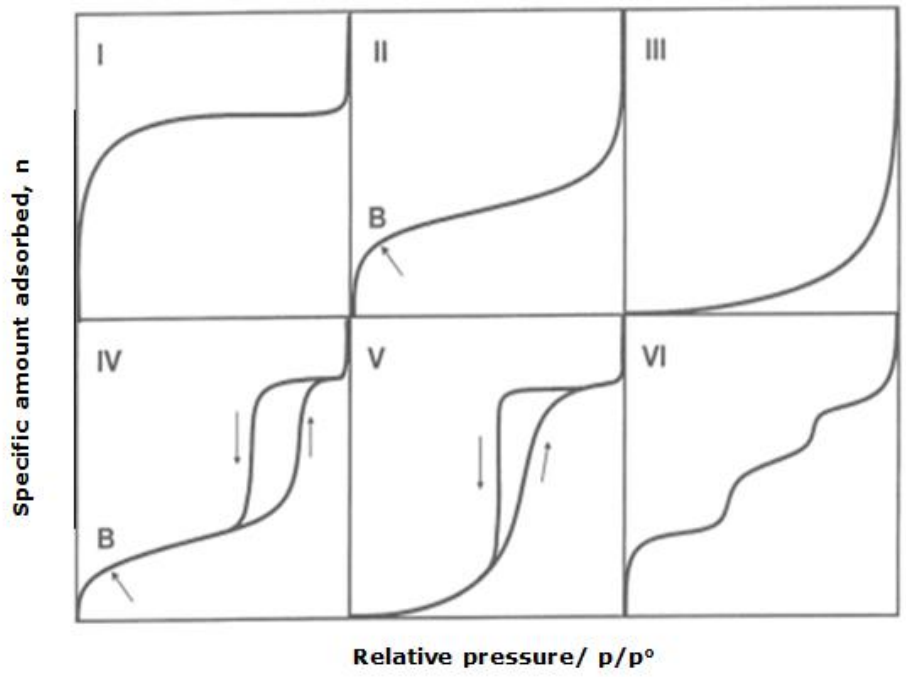

Figure 3.4. The main categories of gas adsorption isotherms according to the IUPAC classification (Rouquerol et al., 2013).

Type I isotherm represents the microporous solids, that have small pores at which Langmuir area can be estimated. Type II is given by non-porous solids or macroporous samples associated with high energy of adsorption (e.g. silica and nonporous alumina). Macroporous or non-porous materials which have a weak interaction between the adsorbent and the adsorbate (e.g.water/ graphite) are shown in type III plot. The mesoporous materials with hysteresis are represented by type IV (e.g. silica and mesoporous alumina). Type V refers to porous materials which have a weak interaction between the adsorbent and the adsorbate (e.g. water /activated carbon). Type VI can attributed to different possibilities of multiple pore sizes within a homogeneous surface (e.g. Kr and NaCl /graphite/ /Kr).

There are a number of models which can be used to analyse the adsorption isotherm in order to calculate the specific surface area , i.e. Langmuir ,BET, Dubinin, etc.(Rouquerol et al., 2013). The Hysteresis loops often appear in the physisorption isotherms of the mesoporous adsorbents. Hysteresis loops are usually associated with capillary condensation (Rouquerol et al., 2013). As the chemical potential of the adsorptive

control the adsorbed amount of the adsorbate, the thermodynamic reversibility of the two branches of adsorption/desorption cannot be satisfied. Accordingly, a stable and reproducible hysteresis appears. The main types of hysteresis loops defined in the IUPAC classification (H1-H4) were shown in Figure 3.5. Type H1 is a narrow and nearly parallel loop. H1 indicates that the adsorbent has uniform pores distributed in a narrow range. Type H2 is a broad loop given by adsorbents which have interconnected networks of wide ranges of pores in different shape and size. H3 is given by the adsorbents with particles in platy shape and pores in a slit-shaped. Type H3 is difficult to form due the limiting desorption curve. Type H4 also had a limiting desorption curve and given by adsorbent which had slit-shaped microspores.

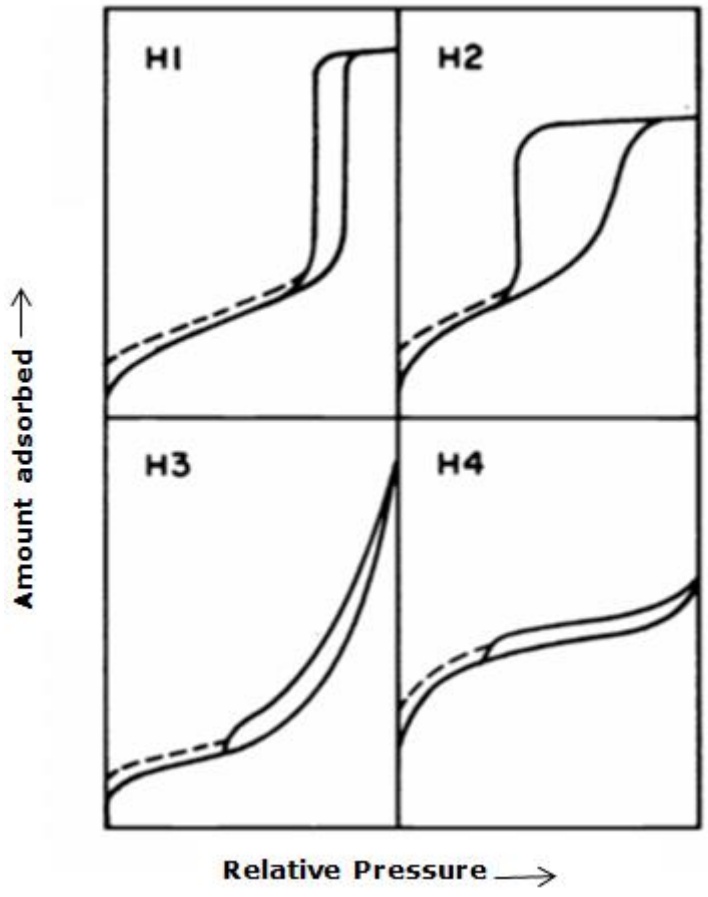

Figure 3.5. Types of hysteresis loops according to the IUPAC classification (Rouquerol et al., 2013).

3.5.3.1 Brunauer-Emmett-Teller (BET) method

The most common method used for the surface area measurement developed by Brunauer, Emmett and Teller (1938) (Richardson, 1999). BET method considered as an extension of Langmuir theory of monolayer adsorption to infinite numbers layers' adsorption. Firstly, equation 3.18 was used to evaluate v_m, the gas volume adsorbed in the monolayer (Rouquerol et al., 2013).

$$\frac{p}{v\ (p_0 - p)} = \frac{1}{v_m c} + \frac{(c-1)p}{v_m c p_0} \tag{3.18}$$

where:

v : Volume of gas adsorbed at pressure p/cm^3.

v_m : volume of gas adsorbed in monolayer/cm^3.

p_0 : saturation pressure of adsorbate gas at the experimental temperature, mmHg.

c : constant related exponentially to the heats of adsorption and liquefaction of the gas.

$$C = \exp\ (\frac{q1 - ql}{RT}) \tag{3.19}$$

where:

$q1$: heat of adsorption on the first layer/J.

ql : heat of liquefaction of the adsorbed gas on all other layers/J.

R : The gas constant (R=8.3144598 $\mathrm{J\,K^{-1}\,mol^{-1}}$)

If equation (3.18) is obeyed, a graph of $\frac{p}{v\ (p_0 - p)}$ versus $\frac{p}{p_0}$ should give a straight line, the slope and the intercept of which can be used to evaluate v_m and c (Rouquerol et

al., 2013). The specific area $a\ (BET)$ is calculated in the second stage by applying equation (3.20) (Rouquerol et al., 2013).

$$a\ (BET) = v_m\ L\ o \tag{3.20}$$

Where:

L : Alvogrado constant (L=6.022140857×10^{23} mol^{-1}).

$a\ (BET)$: the specific surface area /m^2/g.

o: the average cross sectional area occupied by any molecule in the monolayer, it should be given by another method /nm^2.

The surface area of the catalysts/sorbents was calculated by the N_2 adsorption/desorption isotherms at −196 °C, on a Quantachrome Autosorb-1 Automated Gas Sorption System and the accompanying software, Autosorb for Windows V1.24. The parameters for the Autosorb set-up were listed in Table 3.3. The sample was first degassed in vacuum for 3h at 300°C prior to its run. The collected experimental data was used to estimate the surface area by mean of the given equations 3.18, 3.19 and 3.20 (Brunauer et al., 1938).

Table 3.3. BET parameter values.

Parameter	Value
Mass of sample/mg	10-50
Outgas temperature/°C	300
Outgas time/h	3
Bath temperature/°C	-196
Analysis time/min	100
Number of BET points measured	11

3.5.4. Porosity test (mercury porosimetry)

Porosity test is essential to identify the porous structure of many materials (Rouquerol et al., 2013). Porosity is defined as as the "fraction of the bulk volume of the porous sample that is occupied by pore or void space" (Dullien, 2012). This definition states that pores are void spaces in the porous structure. Materials are often classified according to their pore sizes.

Three pore size categories have been defined by the International Union of Pure and Applied Chemistry (IUPAC) where micropores are <2 nm, mesopores are 2-50 nm, and macropores are > 50 nm (Rouquerol et al., 2013). The pores are defined as blind, closed, through and cross-linked pores. The blind pores allow the fluid to enter but not pass through; the closed pores are isolated and inaccessible, whereas the fluid can pass through the cross linked and through pores, see Figure 3.6. The porosity measurement only considers the through, cross-linked and blind pores (Rouquerol et al., 2013). There are variable forms of the pores forms such as cylinder, slit, and cage pores. Mercury intrusion porosimetry is widely used to evaluate the porosity-related features of a material such as pore size and pores distribution.

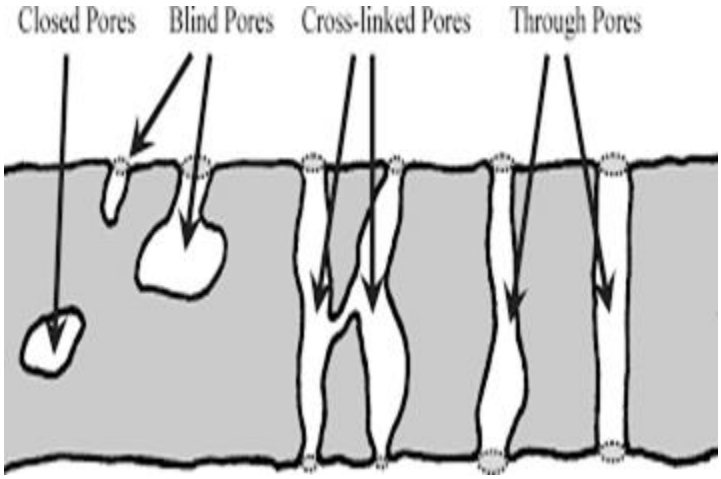

Figure 3.6. Schematic representation of different types of pore (Giesche, 2006).

Porosity and pore size distribution measurements can be achieved by the controlled intrusion of mercury into a porous material under pressure. Mercury intrusion porosimetry is established on the premise that a non-wetting liquid (with a contact angle > 90°) penetrates capillaries if only forced by pressure, see Figure 3.7.

Mercury is a non-wetting liquid; therefore, pressure is needed to force mercury to intrude pores. 0.5-2 g amount of sample was immersed in mercury using Micromeritics Autopore IV Model 9520, which measures a range of pore sizes (0.003 to 360 μm) at a pressure range of up to 413.6 MPa. The sample is first immersed in the mercury and then pressure is applied to sample in order to force mercury to intrude into its cavities and pores. The pressure began at zero as this process was done under vacuum. The amount of pressure needed for mercury intrusion into pores of the sample is inversely proportional to its pores size (Weitkamp et al., 2002). An average of 140° was taken as the contact angle of mercury as for most solids this is between 135° and 142°. The surface tension of mercury at room temperature was obtained from calculated table. The intruded volume of mercury, V and the applied pressure p, were recorded and an intrusion-extrusion curve is obtained as shown in Figure 3.8.

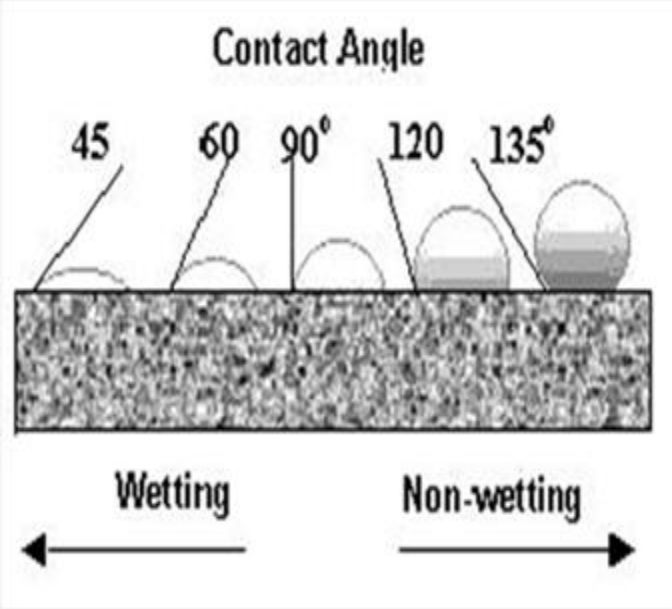

Figure 3.7. Different angles of contact area between wetting and non–wetting liquids and solid surface (Webb, January 2001).

The relationship between the capillary diameter and the applied pressure is described by Washburn (Washburn, 1921) as given in equation 3.21.

$$p = \frac{-4\ \gamma \cos\sigma}{D} \tag{3.21}$$

where:

p : pressure/Pa.

γ : surface tension of the liquid/J/m^2.

σ : contact angle of the liquid/degree.

D : diameter of the capillary/m.

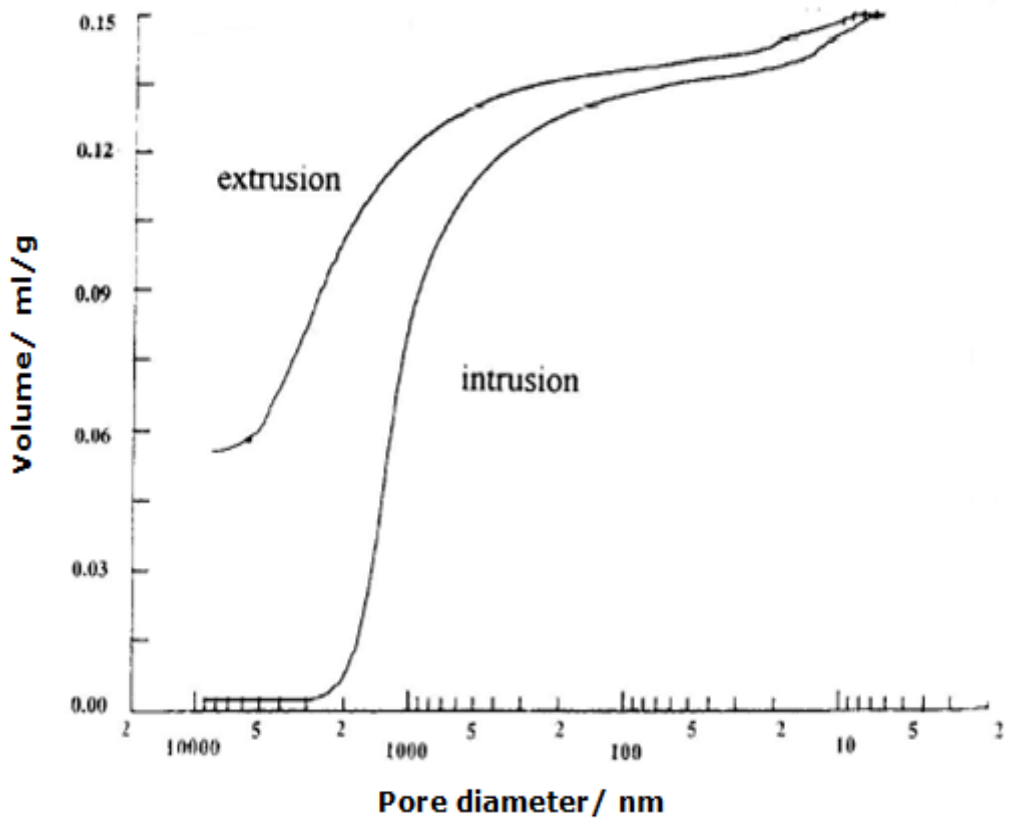

Figure 3.8. Schematic representation mercury intrusion-extrusion curves (Westermarck, 2000).

3.6. Determination of iron oxide reduction temperature

A Netzsch209 F1 Iris is thermal gravimetric analyzer (TGA) was used to measure oxide reduction. It was conducted for the iron oxide catalyst (Fe_2O_3) alone and for the catalyst/sorbent mixture (Fe_2O_3/Ca6Mg2Ce1). The samples were first heated in an alumina crucible at a heating ramp rate of 5°C/min from 25°C up to 900°C. The change in the sample weight was recorded. The amount of the removed oxygen compared with total oxygen content available for reduction in the oxide samples, was used to calculate the reduction efficiency.

3.7. Sorption enhanced ethanol steam reforming test

The production of H_2 from ethanol steam reforming was investigated in a fixed bed reactor (ID =0.65 cm, L=40 cm) placed inside a tube furnace, see Figures 3.9 and 3.10. During all the tests, the loading of sorbent /catalyst was calculated to give an equivalent content of 1g in 6:1 of Ca6Mg2Ce1/Fe_2O_3 weight ratio respectively. The experiments were performed with a steam to ethanol molar ratio of 6. The temperature was raised at a rate of 5°C/min under an atmosphere of inert argon at a flow rate of 30 ml/min as shown in Figure 3.9. The ethanol/water mixture was injected to the reactor through a syringe pump (Cole-Parmer 74900-00,-05) at a predetermined gas hourly space (GHSV, defined as the reactant gas flow rate /reactor bed volume). Then the de-carbonation step was started by purging the reactor thoroughly with argon (Ar) for 1h in 700°C in order to regenerate the adsorbent before a new cycle was commenced. Gas products were analysed by mass spectrometer (Hidden, HPR-20). Two hours after starting the injection of ethanol/water premixed liquid the produced gases were collected in a gas bag and analysed on a gas chromatograph (Clarus 580 Perkin-Elmer). Some experiments were performed by varying the GHSV of ethanol/ steam mixture in the range of at a constant operating temperature of 700 °C. Other experiments were conducted at different operating temperatures of 550, 600,650 and 700°C at constant GHSV in order to explore the optimum operating conditions.

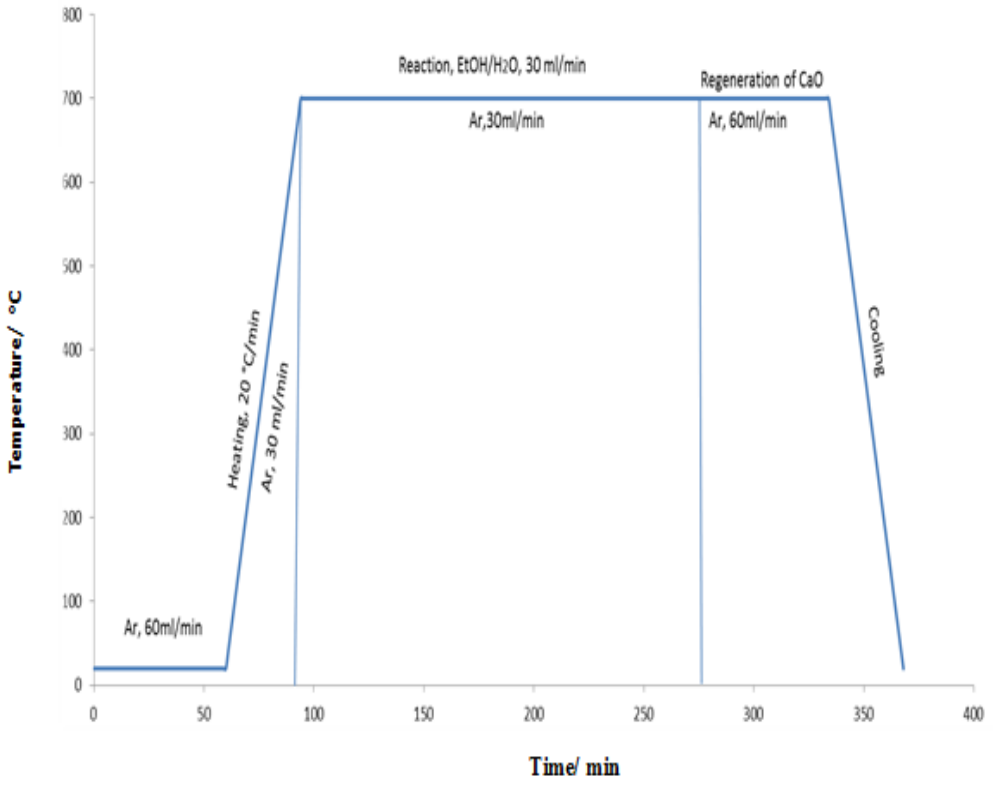

Figure 3.9. Sorption enhanced ethanol steam reforming test conditions for one steam reforming/regeneration cycle.

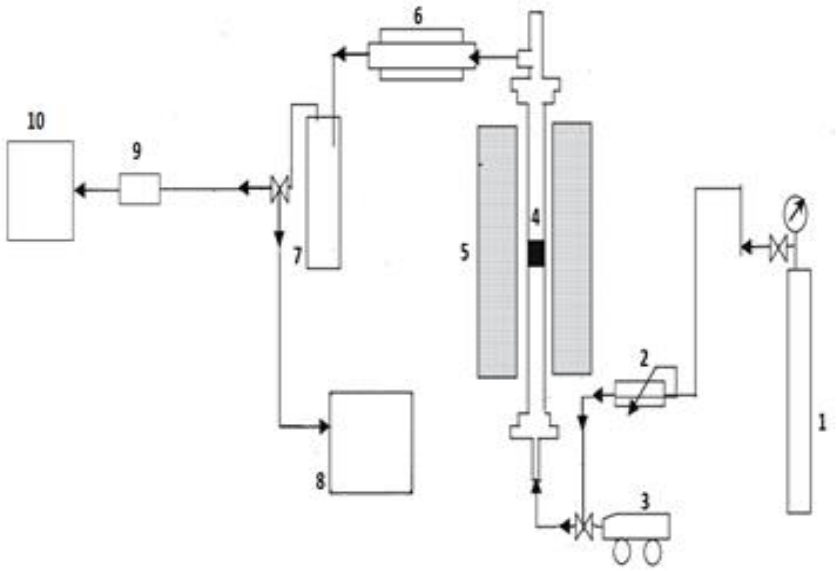

Figure 3.10. Schematic diagram of the reformer rig set up (1) Ar cylinder (2) gas flow controller (3) syringe pump (4) catalyst with or without sorbent (5) tube furnace (6) condenser (7) bubble flowmeter (8) mass spectrometer (9) gas bag and (10) gas chromatograph.

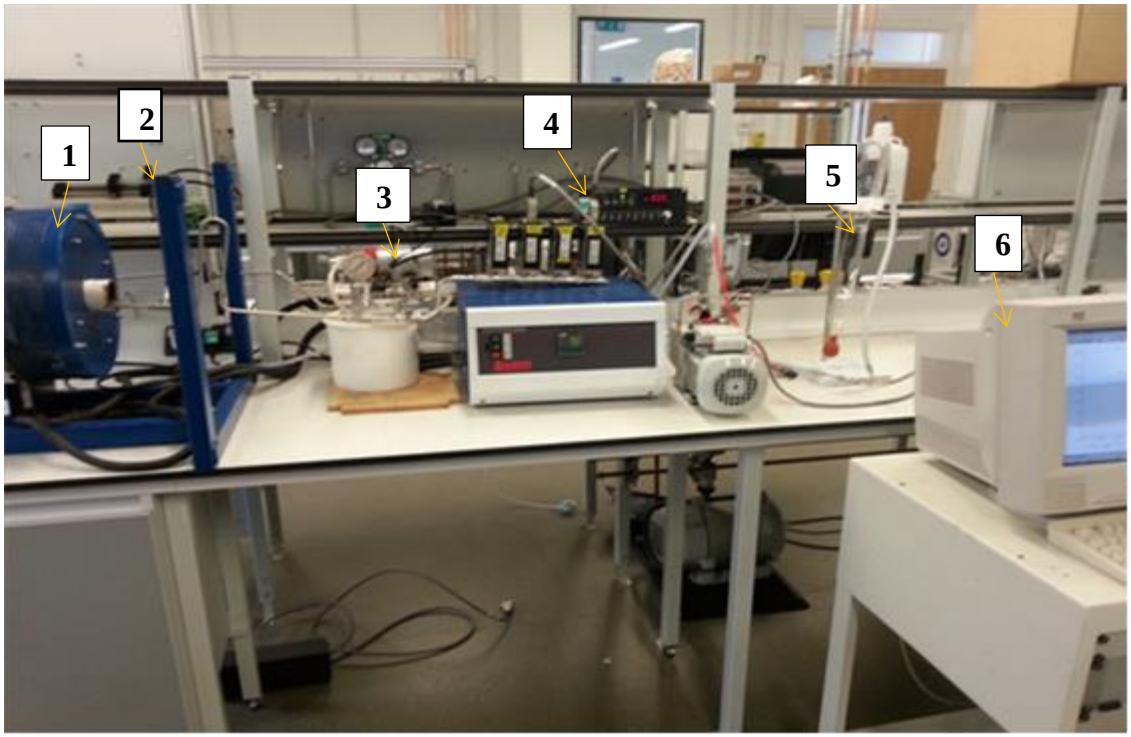

Figure 3.11. Reformer rig set up (1) tube furnace (2) syringe pump (3) condenser (4) gas flow controller (5) bubble flowmeter and (6) mass spectrometer.

3.7.1. Gas analyzing Instruments

3.7.1.1. Hiden HPR20 Mass Spectrometer

Hiden (HPR-20 QIC) is an online gas analyser. It is considered as a semi-quantitative and quality analyser. It consists of four stages: ionization, acceleration, deflection and detection as shown in Figure 3.12. In the ionisation stages, the sample was vaporised and turned into ions then, the ions were hit by electrons (Lehmann, 2011). As a results, ion sample will carry positive charge (Hoffmann, 1996, Guilhaus, 1995). Then, the sample mixture was introduced into a region between two metal plates charged to high voltages, where it was accelerated and spread out according to the amount of charges they had (Hoffmann, 1996, Guilhaus, 1995). The later stage is known as the acceleration stage. In the deflection stage, the ions were shot into a magnetic field, where different ions is deflected and split into different spectra according to their masses and also their

positive electrical charges. After that, in the detection stage the ions were passed through.

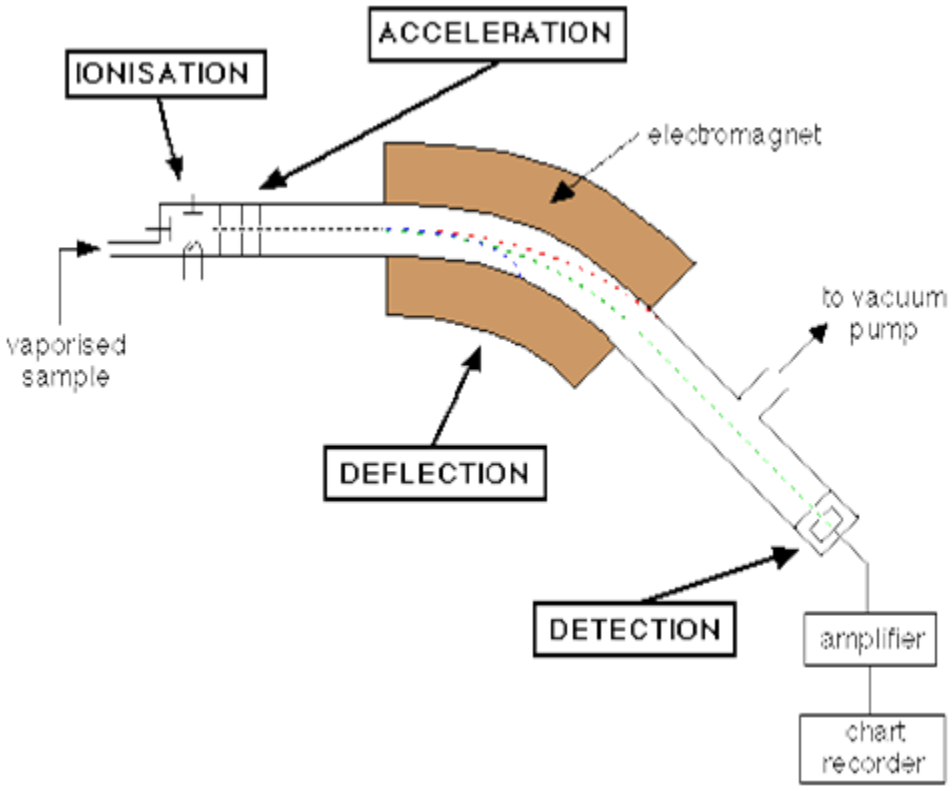

Figure 3.12. Schematic of a mass spectrometer (Chemguide, 2000).

The output from the chart recorder is known as the mass spectrum and usually presented as a vertical stick or bar graph, see Figure 3.13. This bar represents the specific ions as mass/charge (m/z) ratio and the bar length indicates the ion relative intensity or the ion relative abundance. The ion with the highest intense is referred to as base peak and it is given an abundance of 100. The m/z value is equivalent to mass itself when the ions formed have a single charge. The molecular ion usually has the highest mass ion intensity whereas the lower-mass ions intensity is considered as the ion fragments.

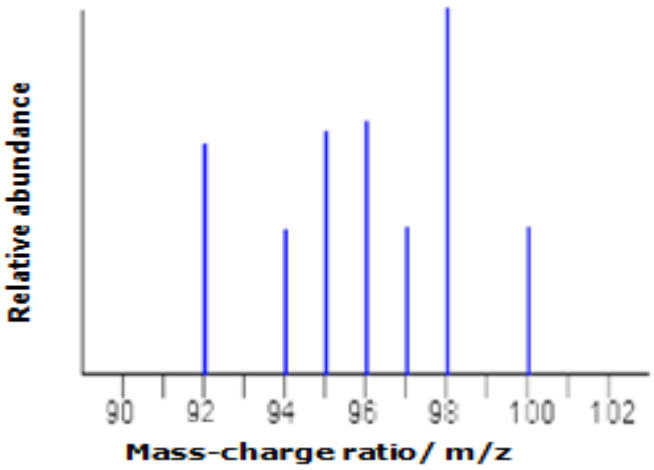

Figure 3.13. The mass spectrum diagram for molybdenum (Chemguide, 2000).

3.7.1.2. Gas chromatograph

Gas chromatography is chemical analytical procedure for detecting different components in a complex liquid or gas sample (analyte), see Figure 3.14. Clarus 580 gas chromatograph (GC) fitted with a thermal conductivity detector (TCD) and flame ionization detector (FID) operating at 200°C was used to analysis the gas sample obtained after ethanol reformation reaction. 5 ml of gas sample were introduced to the GC for hydrocarbon and non-hydrocarbon analysis. Helium was used as the carrier gas in order to sweep gas molecules through the column, where it was adsorbed either onto the packed materials in the column or onto the column walls. The adsorption strength, which governs by the molecules types determine the rate gas progression along the column. Accordingly, each component reaches the column end at different time. Therefore, the different types of molecules in the analyte mixture were separated. The time needed for a component to reach the column end is known as its specific retention time and used to identify its type (Harris, 1999, Karasek and Clement, 2012). Hydrocarbon (HC) gases were identified in FID by injecting 9.1 ml of the sample at 250°C. The oven temperature was programmed from 60°C (13 min hold) to 180°C (12 min hold) at 10°C /min. Each gas was identified quantitatively in comparison to methane as the external gas standard. Non-hydrocarbon (NHC) gases were determined by the

TCD column by injecting 500 microliter of sample of gas at 165°C. The individual gases were measured quantitatively in comparison to the hydrogen which was injected separately as the non-hydrocarbon external gas standard.

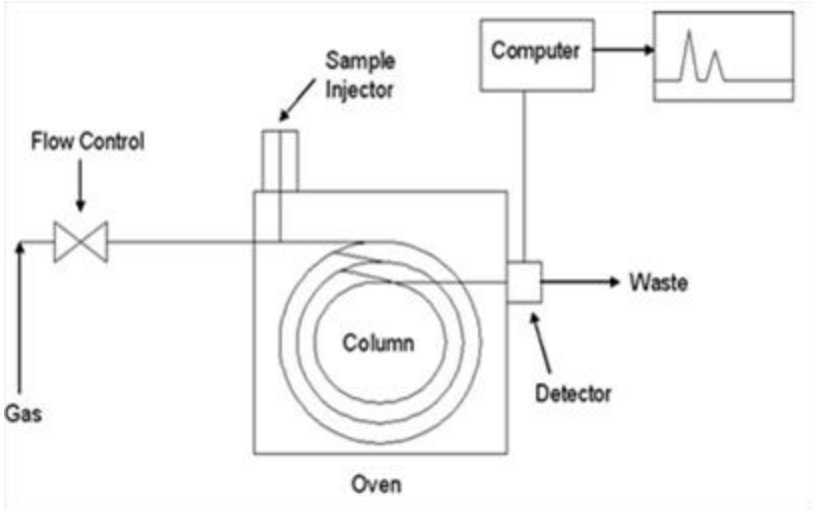

Figure 3.14. Diagram of a gas chromatograph setup (Blan et al, 2013).

3.8. Carbon deposition test

The carbon deposition on the surface of the used catalyst was investigated in TGA (SDT-Q600-TA instrument). The used catalyst sample was placed in an aluminium crucible and then introduced to the TGA. During the TGA test, the sample was heated from 25°C to 900°C at a ramp rate of 10°C/m in air with a flow rate of 50 ml/min. The recorded weight loss is equivalent to the weight of the deposited carbon removed.

CHAPTER FOUR

CO_2 capture and characterisation tests of the prepared CaO-based sorbents and the sorbent/catalyst mixture.

4.1. Introduction

The CO_2 uptake capacities of the prepared CaO- based sorbents were evaluated using thermo-gravimetric (TGA) analyzer. First, the optimum calcination temperature was determined. Then, the prepared sorbents were exposed to 100% CO_2 gas stream at 700°C and atmospheric pressure. The CO_2 capture results of the prepared sorbents are shown in section (4.3). According to their capture results, two groups of the sorbents were selected for further characterisation and carbonation/de-carbonation cycling tests. The prepared calcium oxide CaO was used as a bench mark. Modelling results of the CO_2 uptake kinetic were displayed and discussed in section (4.4). The characterisation tests were conducted to study the sorbent textural effect on CO_2 uptake capacity. The characterization results were discussed in section (4.5). Cycling tests and the characterisation of the sorbents after cycling were presented in section 4.6-4.7. The preparation and characterisation results of the iron oxide catalyst and CaO-based sorbent mixture were shown in section (4.8). Finally, summary of this chapter is presented in section (4.9).

4.2. Determination of the calcination temperature

Calcination is a thermal treatment applied to the sorbents or the catalysts (Perego and Villa, 1997). It is normally performed in the presence of air at temperatures below the melting point of the catalyst/sorbent. It leads to the modification or stabilisation of the mechanical properties of the catalyst/sorbent through phase transition or thermal decomposition. The volatile fraction and the chemically bonded CO_2 or water are removed during calcination (Perego and Villa, 1997). It was reported that excessive temperature may lead to the catalyst/sorbent sintering (Men and Yang, 2012). Sintering

alters the catalyst/sorbent surface area structure and may affect its activity (Argyle and Bartholomew, 2015). Accordingly, an optimum calcination temperature is desired. Thermogravimetric analysis (TGA) was conducted to determine the optimum calcination temperature. 5 g of the sorbent was exposed to air at 10°C/min heating rate ramping from 25 °C to 800 °C. It was observed that the mass loss started at 80 °C and it was stabilised over 600 °C, see Figure 4.1.

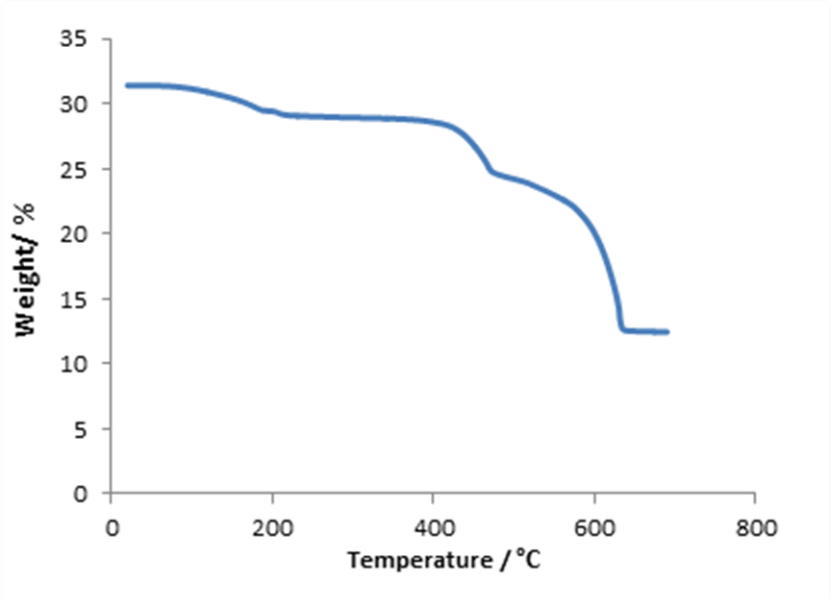

Figure 4.1. TGA profiles for the determination of the calcination temperature for the Ca6Mg2Ce1 at heating ramp of 10 °C /min from 25 °C to 700 °C in air and at atmospheric pressure.

The mass loss of the sample up to 600 °C was mostly likely from dehydration, as water of crystallisation in the sample started to be released at about 400 °C and finished at about 630 °C. This weight loss was due to the thermal decomposition of $Ca(OH)_2$ as $Ca(OH)_2$ decomposes to CaO at 450- 500 °C (Criado et al., 2014). Similar results were found and discussed in section (5.2.4) of the TGA and XRD results for the used catalyst/sorbent mixture sample. Accordingly, a calcination temperature of 650 °C for 3 hours was applied to the all of the prepared samples.

4.3. Carbonation test.

The preliminary results of CO_2 uptake capacities of all prepared sorbents were based on the first part of carbonation/de-carbonation cycle i.e. the carbonation step. All the prepared sorbents were exposed to a 100% CO_2 gas stream for 1 h at 700 °C and atmospheric pressure in a TGA. It was reported that the sorbent porosity which reflects in its CO_2 uptake capacity, decrease as the carbonation reaction extended and reach a steady state (Wu et al., 2010, Yu et al., 2012). Therefore, the carbonation and de-carbonation reactions time was set at 60 min to complete the fast stage and allow the diffusion stage to stabilise as discussed later in section (4.4). It had also been established that CaO carbonation reaction is limited by the formation of $CaCO_3$ product layer which prevents the completion of carbonation reaction (Park and Yi, 2012a). Therefore, less than 80% of the calcium utilisation could be achieved (Montes-Hernandez et al., 2012). CO_2 uptake capacities of all the prepared samples are presented in Table 4.1. It was observed that, although Ca11Mg2Ce1 and CaO had high calcium weight percentages 72 wt. % and 100 wt. % respectively their calcium utilisations were low, 30 wt. % and 18 wt. % respectively. Ca1Mg2Ce1 sample had a low calcium percentage uptake capacity but its calcium utilisation was very high at 69%. These results suggest that the high calcium conversion in the sorbent did not relate to its calcium content only but also to its porous structure, as later discussed in the section (4.5). The thermogravimetric analyser, TGA),SDT-Q600-TA instrument, provides a balance sensitivity of 0.1 μg and calorimetric accuracy of ± 2%.The CO_2 uptake tests were repeated to investigate the accuracy of the results, the error difference was found to be ± 1%.

Table 4.1. CO_2 uptake capacities for all the prepared sorbents in weight and molar percentage bases.

Sample	CO_2 uptake in Weight/ %	CO_2 uptake in /molar (*) %
Ca4Mg2Ce1	25	66
Ca6Mg2Ce1	29	66
Ca3Mg2Ce1	10	33
Ca2Mg2Ce1	16	42
Ca1Mg2Ce1	7	69
Ca7Mg2Ce1	6	12
Ca11Mg2Ce1	17	30
CaO	14	18

(*) mole CO_2/mole CaO

According to their CO_2 uptake capacities, two groups were selected for further characterisation and carbonation/de-carbonation cycling tests. The prepared CaO was used as the bench mark. The first group had higher CO_2 uptake capacities Ca6Mg2Ce1 and Ca4Mg2Ce1 while the second group had relatively low CO_2 uptake capacities Ca11Mg2Ce1 and Ca1Mg2Ce1, see Table 4.1. Ca11Mg2Ce1 had high CaO molar content, whereas Ca1Mg2Ce1 had low CaO molar content. It was observed that the CO_2 uptake capacities of Ca4Mg2Ce1 and Ca6Mg2Ce1 25 wt.% and 29wt.% respectively were in the acceptable range for sorption enhanced steam reforming (SESR) processes, i.e 20-40 wt. % (Park et al., 2012, Yi et al., 2005 and Abanades et al., 2004).

Table 4.2. CO_2 uptake capacities in weight percentage and molar bases of the selected sorbents.

Sample	CaO percentage in sample /wt. %	CO_2 uptake by weight (wt CO_2/wt $Ca_x Mg_y Ce_z$) /wt. %	CO_2 uptake by weight (wt CO_2/wt CaO) /wt. %	CO_2 uptake by moles* (CO_2 moles/CaO moles) /mol.%
Ca4Mg2Ce1	46	25	52	66
Ca6Mg2Ce1	56	29	52	66
CaO	100	14	14	18
Ca11Mg2Ce1	72	17	24	30
Ca1Mg2Ce1	13	7	54	69

* Based on CaO reacts with 78% wt CO_2 to form $CaCO_3$; wt: weight of gas or oxides per gram.

4.4. Kinetics of CO_2 uptake reaction

Physical adsorption (physisorption) and chemical adsorption (chemisorption) are the principal adsorption phenomena. Physisorption is initiated by secondary Van der Waals attractive forces such as induced dipoles and dipole-dipole interaction. Physisorption is usually used for the measurement of adsorbent porosity and surface area. Alternatively, chemisorption involves electron transfer between adsorbent (the solid) and adsorbate (the fluid) and it is similar to chemical reaction. Experimental conditions such as temperature, pressure and the adsorbent properties affect the rate of chemisorption. Derouane (2006) reported that chemisorption and physisorption are overlap in microporous sorbents (Hedin et al., 2013, Derouane, 1998). In this study, the terminology "sorption" is used to describe the CO_2 uptake reaction. Two principle different stages are well known for CO_2 uptake in the literature (Witoon, 2011, Lu et al., 2009). These stages were identified as the rapid surface chemical reaction stage which usually occurs within 3 min and the slow diffusion-controlled stage. In the surface chemical reaction stage, CO_2 initially reacts with the CaO outer surface to form a $CaCO_3$ layer which covers the CaO core (Witoon, 2011). In the slow diffusion-controlled, the carbonation reaction occurs in the CaO core, as CO_2 diffuses through the formed $CaCO_3$

layer to reach the CaO core. Figure 4.2 for Ca3Mg2Ce1 TGA profile of CO_2 uptake shows that in the fast the carbonation reaction 76% of the total CO_2 uptake occurs within the first 5 minutes of the contact time. This stage contributed to the maximum slope obtained before the diffusion controlled stage. (Abanades and Alvarez, 2003) reported that the high rate of the carbonation continues until $CaCO_3$ layer thickness reaches 50 nm. After this point, a significantly slower CO_2 uptake rate occurs due to the diffusion of the CO_2 through the carbonate layer to react with CaO core. As the reaction proceeds further to the CaO ultimate carbonation conversion, the product-layer diffusion slows down the carbonation reaction to near zero (Symonds et al., 2009). However, in this work it was observed that CO_2 uptake reaction profile of Ca6Mg2Ce1, Ca4Mg2Ce1 and Ca1Mg2Ce1 could be divided into three phases. The latter observation suggests that the CO_2 uptake kinetics of these samples could be modelled by three different kinetic models, see Figure 4.3.

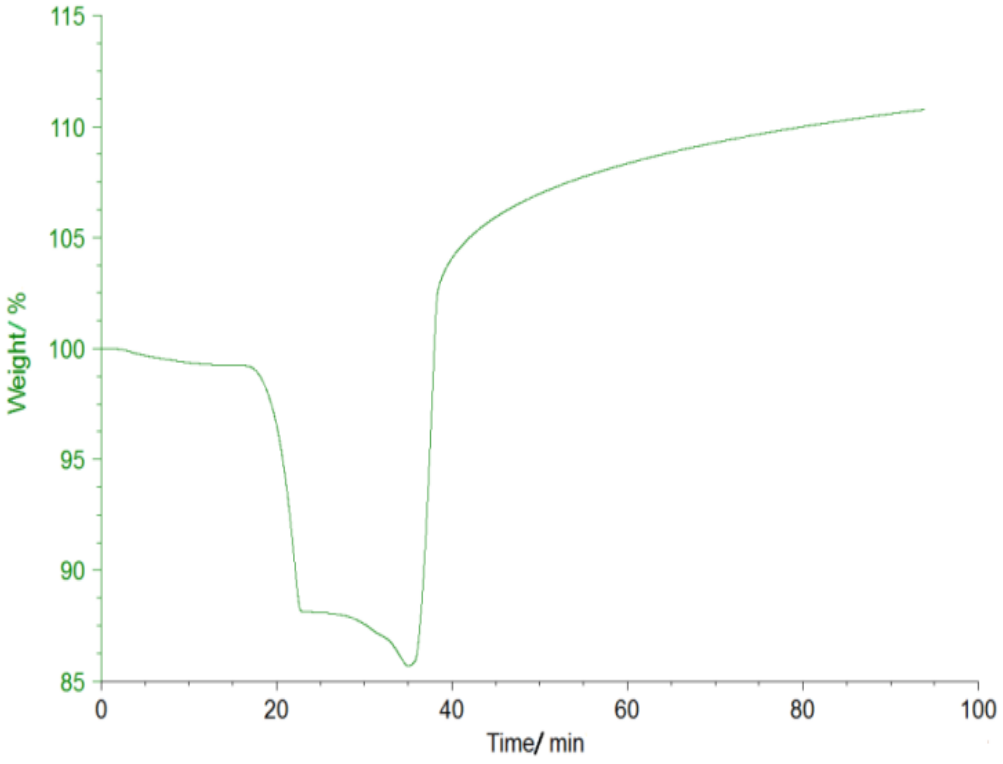

Figure 4.2. TGA profile of Ca6Mg2Ce1 for CO_2 uptake at 700 °C and atmospheric pressure.

The experimental data for the CO_2 uptake were obtained from TGA experiments and used for the evaluation of the conversion degree (α) as shown in equation 3.3. Kinetic modelling of the experimental data of a particular reaction describes the reaction type and interprets it into mathematical rate equation (Khawam and Flanagan, 2006). The kinetic models for CO_2 adsorption of the selected sorbents were determined by the means of model fitting method. The model fitting method is widely used to investigate the kinetics of gas-solid reaction (Meng, 2011). A set of reaction kinetic models described by (equation 3.4-3.9) was used to determine the model which gave the best description of the CO_2 uptake kinetic (Brown et al., 1980). The left sides of these equations were plotted against time, with the linear trend lines plotted to determine the best fit to the experimental data.

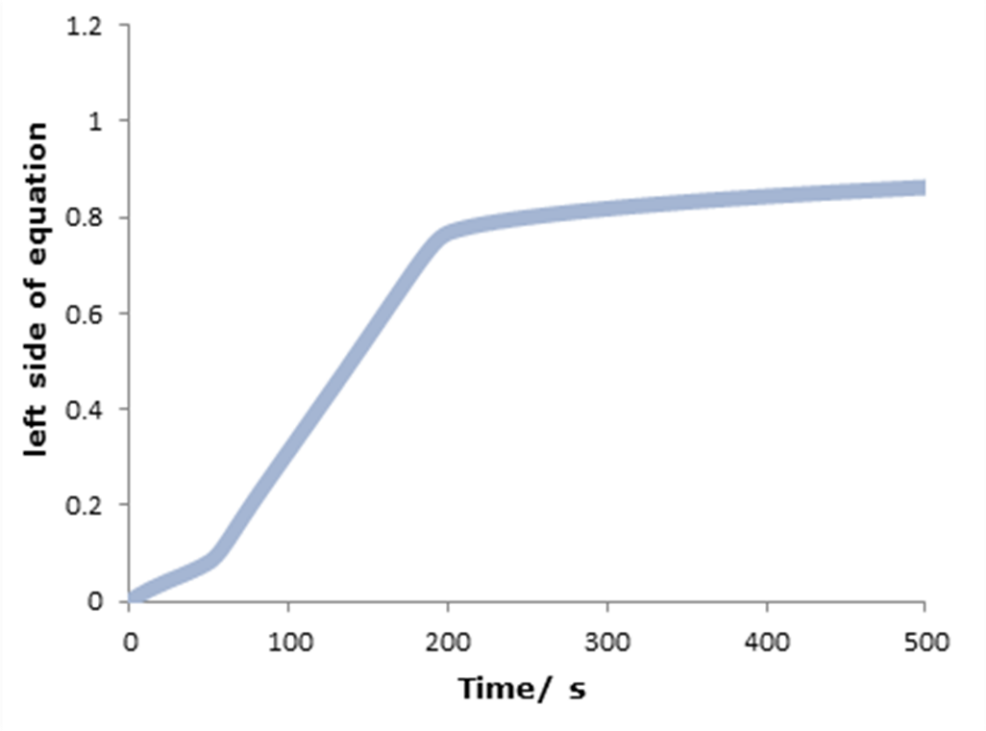

Figure 4.3. Johnson-Mehl-Avrami (JMA2) model fitting stages of Ca6Mg1Ce1.

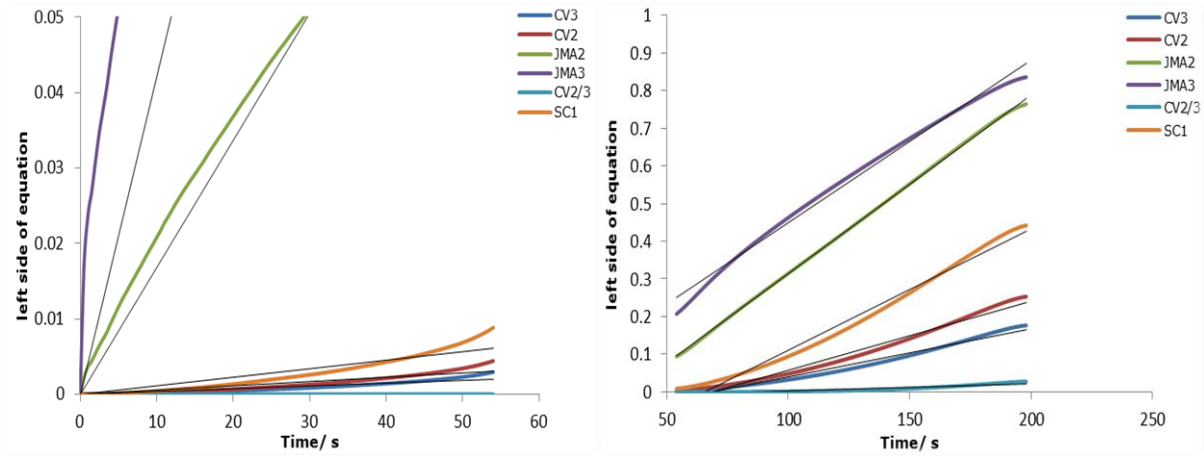

(A) (B)

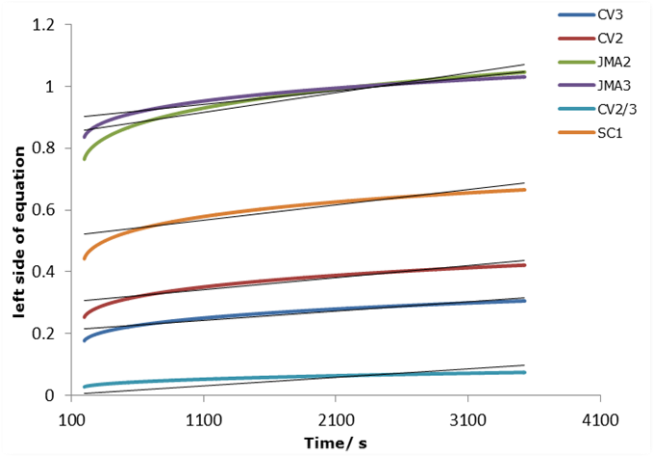

(C)

Figure 4.4. Kinetic models of Ca6Mg2Ce1 sample A (0-54 s, R^2= 0.9894) B (54-198 s, R^2=0.9998) C (198-3480 s, R^2=0.9449) fitted to experimental adsorption straight lines represent the linear best-fit line for each of the models.

Figure 4.4 shows examples of the fitting models for (Ca6Mg2Ce1). It was found that the JMA (Johnson-Mehl-Avrami) model best fitted the CO_2 uptake mechanism in the initial stage for all samples except the first stage in Ca4Mg2Ce1, see Table 4.3. The JMA model suggests that the reaction kinetics were governed by the nucleation and the growth of a new phase nuclei ($CaCO_3$) independent of the location (Selvam et al., 1986a, Liang et al., 1999b). After 2-5min, the JMA2 underestimated the CO_2 uptake, where a three-dimensional diffusion (tridimensional particle shape) contracting volume model with

three dimensional growth of existing nuclei with decreasing velocity of $CaO/CaCO_3$ interface movement, CV2/3, appeared to fit best the CO_2 uptake data in the final stages of the all samples. The corresponding best fitted models of the different kinetics stages for all the selected sorbents were listed in Table 4.3.

Table 4.3. The different fitting models for selected models.

Sample	Time Interval/s	R^2	Fitting models
Ca6Mg2Ce1	0- 54	0.9894	JMA2
	54-198	0.9998	JMA2
	198-3480	0.9449	CV2/3
Ca4Mg2Ce1	0-120	0.9294	SC1
	120-258	0.9987	JMA2
	258-3480	0.8978	CV2/3
CaO	0-126	0.999	JMA2
	126-3480	0.8694	CV2/3
Ca11Mg2Ce1	0-180	0.9969	JMA2
	180-3480	0.9224	CV2/3
Ca1Mg2Ce1	0-150	0.9956	JMA3
	150-1380	0.9553	CV2
	1380-3480	0.9603	CV2/3

4.5. Sorbent characterisation

4.5.1. X-ray diffraction (XRD)

XRD patterns of the selected sorbents were collected to examine the phase changes in the sorbents before and after CO_2 uptake, see Figure 4.5 and 4.6, respectively. All of the five fresh samples before CO_2 uptake showed similar profiles with three or four peaks of CaO, MgO, CeO_2 and $Ca(OH)_2$ regardless of the weight percentage of the precursor. The appearance of the $Ca(OH)_2$ peak may have been to moisture contamination of the sample. As $Ca(OH)_2$ decomposed to CaO at 450- 500°C (Criado et al., 2014). $Ca(OH)_2$

presence in the fresh sample may not have affected the sorbent reactivity in the carbonation/de-carbonation reactions (700°C) and in the ethanol sorption enhanced process, which were performed at a temperature range of 550-700°C.

Examination of the CaO d-spacing in all the selected samples indicates that diffraction lines of CaO did not change significantly upon the addition of MgO and CeO_2 to the CaO-based sorbents in the different weight percentage as CaO peak observed at 37.5° had d-spacing of (d=2.40731 nm, d=2.40633 nm, d=2.40545 nm, d=2.40688 nm, d=2.40427 nm) in Ca4Mg2ce1, Ca6Mg2Ce1, CaO, Ca11Mg2Ce1 and Ca1Mg2Ce1 respectively, corresponding to (200) plane of d-spacing (d=2.40587 nm)). After CO_2 uptake, as shown in Figure 4.6, three samples yielded the patterns of $CaCO_3$ The absence of magnesium carbonate ($MgCO_3$) in the samples after CO_2 uptake confirmed MgO presence as a structural support, as MgO did not react with CO_2 at a temperature over 400°C (Park and Yi, 2012a). It was also noticed that the CaO phase was detected in all samples after carbonation, see Figure 4.6, except for Ca1Mg2Ce1 which may have been due to the low CaO content in this sample only 13%, see Table 4.2.

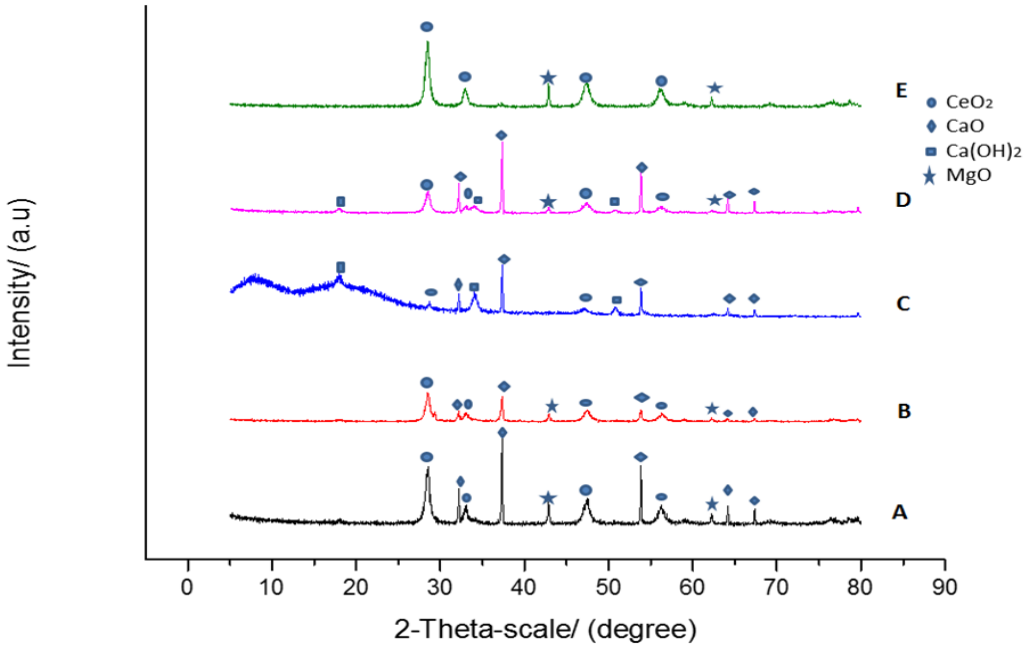

Figure 4.5. XRD patterns of the sorbents before CO_2 uptake (A) Ca6Mg2ce1 (B) Ca4Mg2Ce1 (C) CaO (D) Ca11Mg2Ce1 and (E) Ca1Mg2Ce1.

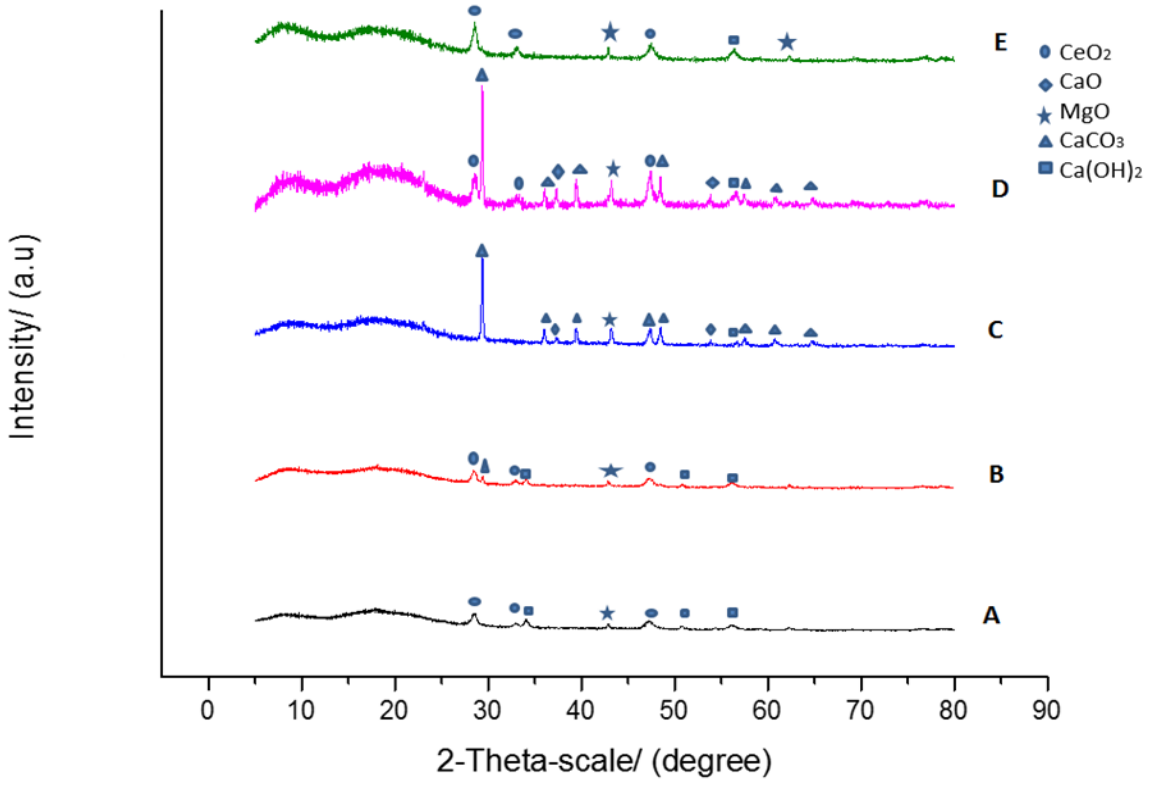

Figure 4.6. XRD patterns of the sorbents after CO_2 uptake (A) Ca4Mg2ce1, (B) Ca6Mg2Ce1, (C) CaO (D) Ca11Mg2Ce1 (E) Ca1Mg2Ce1.

The scherrer equation as given by equation 3.11 was used to calculate the crystallite size of CaO, Ca $(OH)_2$, MgO and CeO_2 the results are displayed in Table 4.4.

Table 4.4. The crystallite sizes of sorbents components before CO_2 uptake.

Sample	CaO crystallite size/nm	$Ca(OH)_2$ crystallite size/nm	MgO crystallite size/nm	CeO_2 crystallite size/nm
Ca4Mg2Ce1	219	N/A	55	15
Ca6Mg2Ce1	408	126	62	14
Ca11Mg2Ce1	107	17	55	12
Ca1Mg2Ce1	60	N/A	61	15
CaO	116	24	N/A	N/A

XRD analysis of the selected samples treated at 650°C calcination temperature revealed that the preparation and calcination procedure were quite enough to convert the nitrate

precursor in to metal oxides as no nitrate phases were detected. XRD patterns, confirmed that CaO had sharp crystalline peaks. The crystallite size of CaO before CO_2 uptake was calculated to be much larger than those of CeO_2 and MgO. These results were consistent with EDX images; see Figure 4.9, where the calcium rich area had a large grain while the CeO_2 and MgO rich areas had smaller grain sizes. The dispersion of these small grain sizes of CeO_2 and MgO between CaO grains may provide a porous surface which favoured the gas–solid reactions and resulted in a high activity of the sorbent. This observation is consistent with (Zhou et al., 2012) who reported that the sorbents with small grains and porous surfaces exhibit high CO_2 capture performance.

4.5.2. Scanning electron microscopy (SEM)

The SEM micrographs obtained from the fresh calcium based sorbents are shown in Figure 4.7. The SEM images of the samples which exhibited a higher reactivity, i.e. Ca6Mg2Ce1 and Ca4Mg2Ce1, see Figure 4.7, showed significant differences in the surface topography from those of the poor CO_2 uptake group, i.e. Ca11Mg2Ce1, CaO and Ca1Mg2Ce1 which are shown in Figure 4.8. The Ca6Mg2Ce1 and Ca4Mg2Ce1 samples had more porous surfaces and grains with different size compared to the group including Ca11Mg2Ce1, CaO, and Ca1Mg2Ce1. The Energy-dispersive X-ray (EDX) image, see Figure 4.9, shows a dark and smooth surface with fewer pores which is the calcium rich area, whereas, the lighter area with small particle size is the magnesium and cerium rich area.

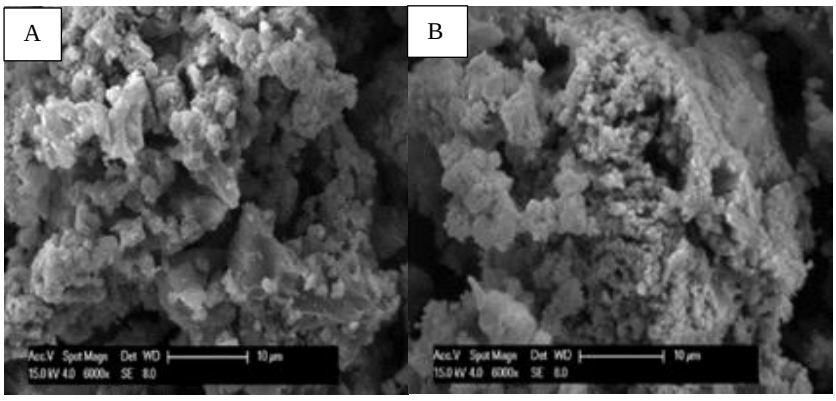

Figure 4.7. SEM images of (A) Ca4Mg2Ce1 and (B) Ca6Mg2Ce1 before CO_2 uptake.

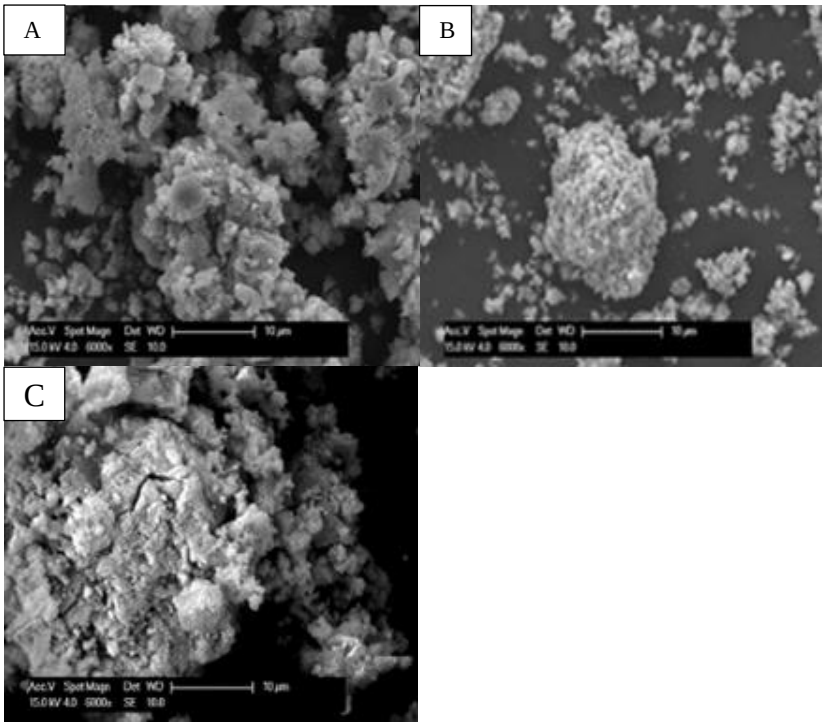

Figure 4.8. SEM images of (A) CaO (B) Ca11Mg2Ce1 (C) Ca1Mg2Ce1 before CO_2 uptake

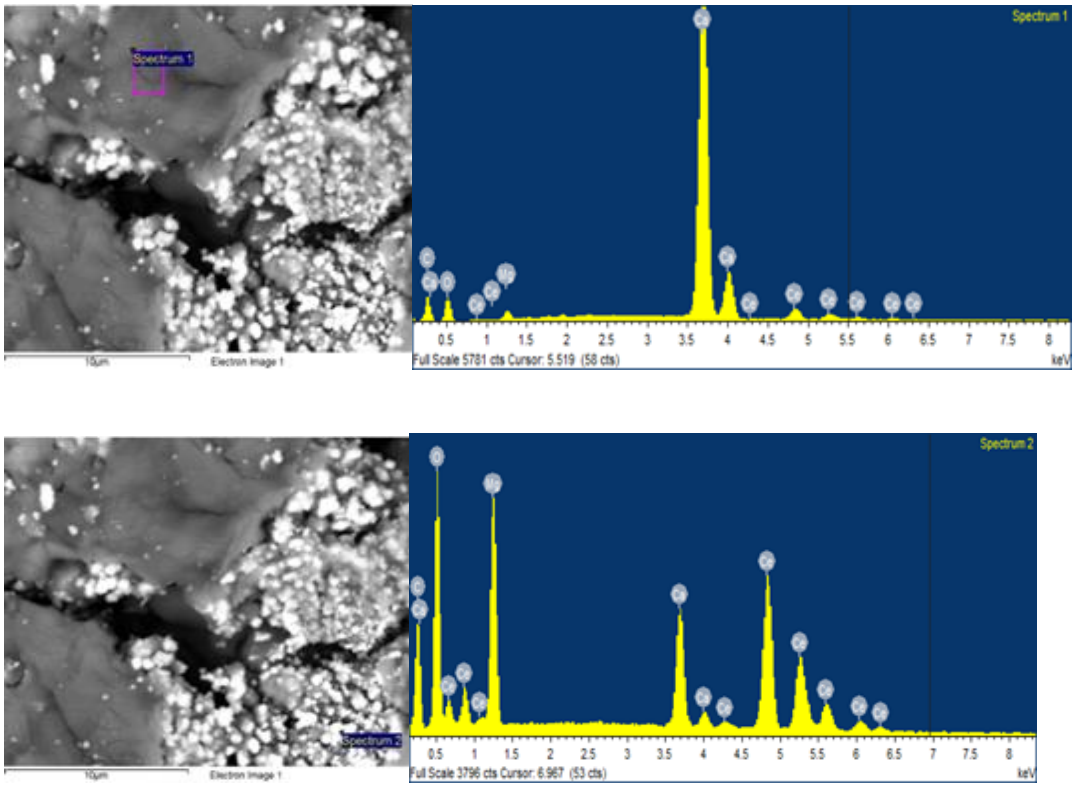

Figure 4.9. EDX images of Ca6Mg2Ce1 sample.

It may be concluded that the sorbents with a higher number of small grains and porous surface display initial high CO_2 uptake. MgO and CeO_2 as the inert elements dispersed among CaO particles and separate the CaO particles and provide micro-voids in the sorbent for the CO_2 pathway. In addition to that, MgO and CeO_2, as inert oxides, dispersed between the CaO particles, prevented the agglomeration and size growth during the multiple carbonation/de-carbonation cycles, as previously reported by (Zhou et al., 2012). Therefore, it was concluded that the CaO content and the inert percentage in the CaO-based sorbent should be optimised to have a substantial CO_2 uptake capacity and reasonable stability during the carbonation/de-carbonation cycles.

4.5.3. Measurement of surface area and porosity

It is well known that CO_2 uptake capacity and stability of the sorbent reactivity during carbonation/de-carbonation cycles are closely related to its micro-morphology (Blamey et al., 2010). Particularly, CO_2 uptake capacity of the sorbents is dependent on the presence of micropores and mesopores in the surface topography (Fennell et al., 2007). Porosity and pore size distribution for the selected sorbents were evaluated using the Micromeritics Autopore IV Model 9520, which measured a range of pore sizes (0.003 – 360) μm at pressure range up to 413.6 MPa. The surface area measurements were performed for the selected samples on a Quantachrome Autosorb-1 automated. Figure.4.10 clearly shows that the best CO_2 uptake groups for the samples before CO_2 uptake have higher porosity percentage, which substantiated the previous observation from SEM images, see Figure 4.7 and 4.8 that a high porosity resulted in higher CO_2 uptake. Although, Ca4Mg2Ce1 and CaO samples have relatively similar porosity percentages of 72% and 71% respectively, Figure 4.11 revealed the difference in the pore size distribution among the two samples and confirms that the Ca4Mg2Ce1 has a smaller pore size volume compared to that of CaO. The surface area measurement results shown in Figure 4.10, gives no clear correlation between best CO_2 uptake and large surface area in samples before CO_2 uptake, which is the reverse of what was expected i.e. large surface area was expected to be the principal factor for the higher

CO_2 uptake capacity. These results were discussed further in the cycling section (4.6) and (4.7).

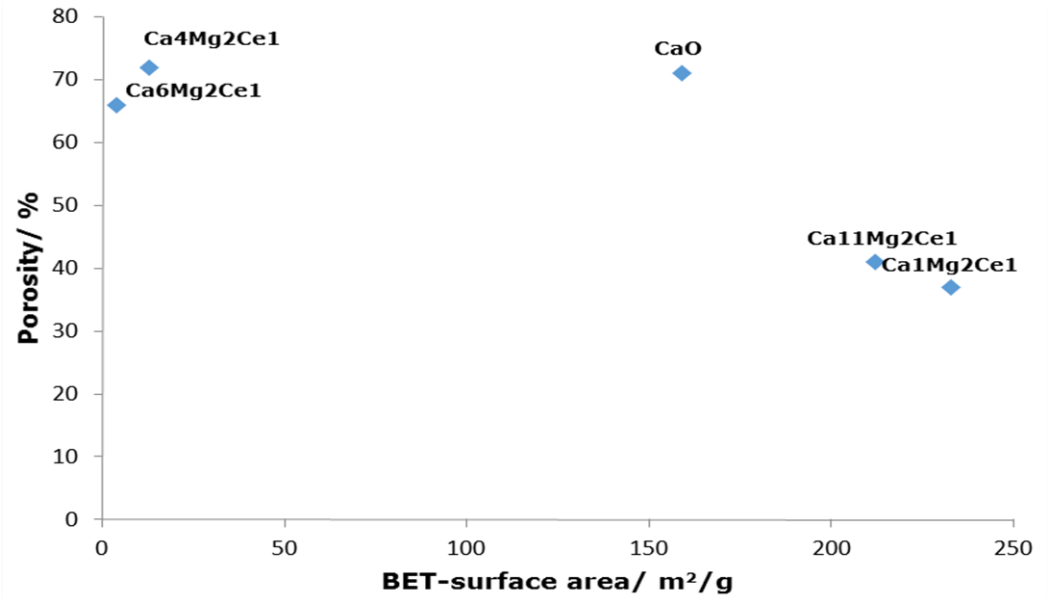

Figure 4.10. Porosity verses BET surface area results for the prepared sorbents before CO_2 uptake.

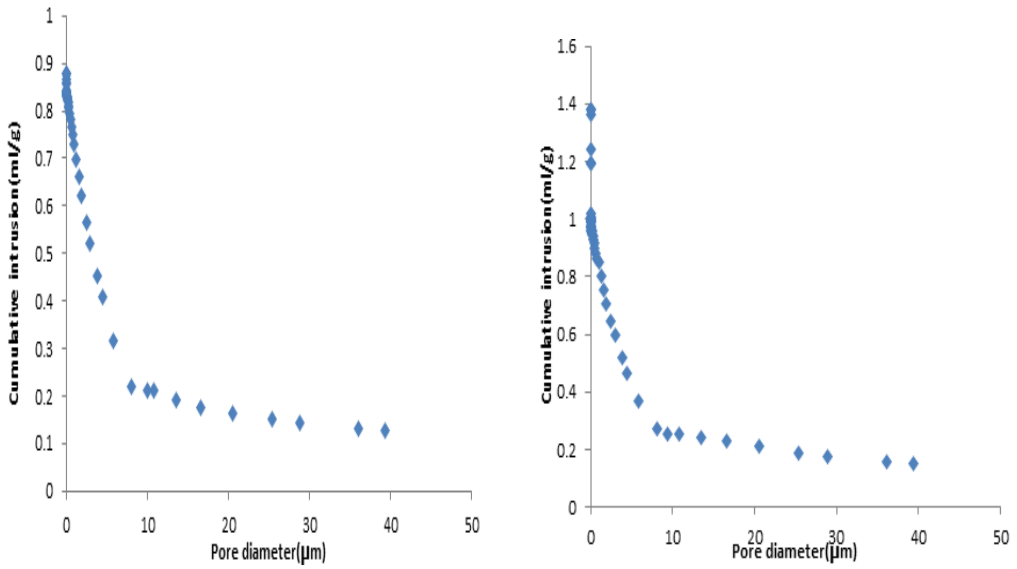

(A) (B)

Figure 4.11. Pore size distribution of: (A) Ca4Mg2Ce1 and (B) CaO before CO_2 uptake.

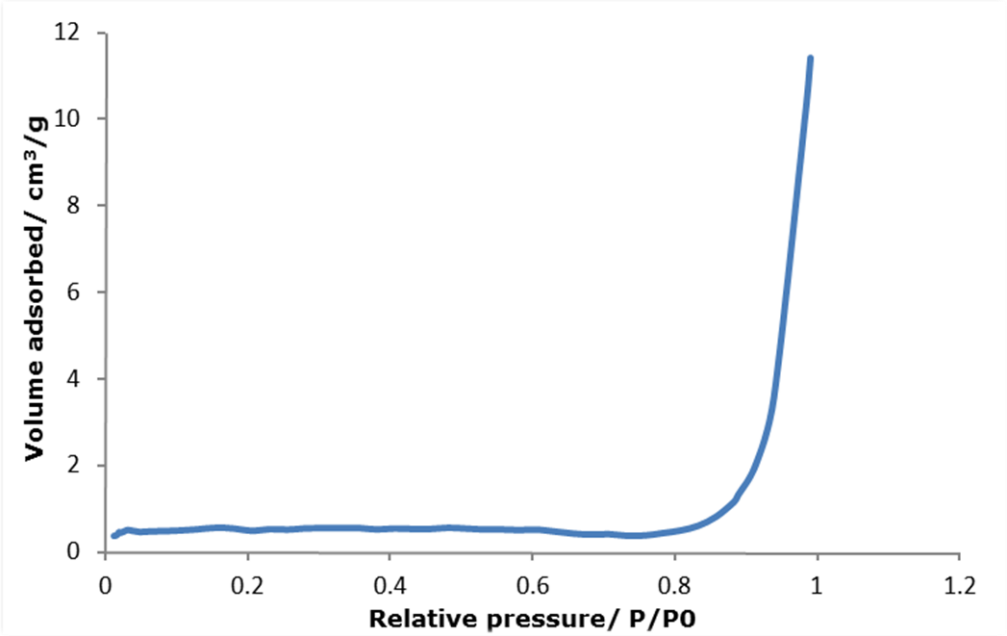

Figure 4.12. Nitrogen adsorption isotherm of Ca6Mg2Ce1 obtained by BET.

It was observed from Figure 4.12 that the nitrogen adsorption started to increase at a relative pressure (p/p_0>0.8). According to the IUPAC isotherms classification discussed in section (3.6.3), the Ca6Mg2Ce1 sorbent was likely to be of Type III which represents the macroporous (>50μm) materials that have weak interaction between the adsorbate and the adsorbent. These results suggest that the most of the pores are in the macro-porous range.

4.6. Sorbent behavior in carbonation/de-carbonation multi-cycle test

The reversibility of carbonation/de-carbonation reactions, see equation (2.8) is limited by the sintering process which leads to gradual decay in the sorbent CO_2 uptake capacity (Shimizu et al., 1999, Abanades et al., 2004). However, the practical use of the sorbent depends on its reactivity and stability during multiple cycles (Manovic and Anthony, 2007). In this study, multiple carbonation/calcination cycles were performed in the TGA to investigate the changes in the sorbents activities upon cycling. The de-carbonation reaction was theoretically done at 850°C (Kyaw et al., 1996). TGA was used to

investigate the decomposition temperature of $CaCO_3$ and thus determine the optimum de-carbonation temperature. The flow rate of CO_2 was 50 ml/min for the carbonation reaction while 300 ml/min of N_2 was used for the de-carbonation step at 700°C. Figure 4.13 shows that the purging N_2 gas in 300 ml/min flow rate at 700°C was enough to level out the CO_2 uptake curve and assure the complete $CaCO_3$ decomposition back to CaO. Therefore, carbonation and de-carbonation reactions were carried out at 700 °C. The data obtained in the CO_2 uptake capacities over successive carbonation/de-carbonation cycles is shown in Figure 4.14. It was noticed that all samples exhibited an increase in CO_2 uptake capcity after the the first cycle. Ca11Mg2Ce1 and CaO had a dramatic CO_2 uptake capacity increase after the first cycle. Ca11Mg2Ce1 increased from 17 wt.% to 54 wt.% whereas CaO increased from 14 wt.% to 53 wt.%. After one cycle, all the selected samples showed a noticeable decline in the CO_2 uptake capacities but at different rates.

Particularly, CO_2 uptake capacities for Ca11Mg2Ce1 dropped rapidly from 54 wt.% after the first cycle to 39 wt.% in the 25 cycles, which corresponded to changes in the maxium carbonation conversion from 92 % to 69 %. While, the CO_2 uptake capacities of CaO dropped from 53 wt.% after the first cycle to 43 wt.% in the 25 cycles, which corresponding to a reduction in the maxium carbonation conversion from 68 % to 55 %. The CO_2 uptake capacities for Ca6Mg2Ce1 decreased from 30 % after the first cycle to 25 wt % in the 25 cycles. Whereas, the CO_2 uptake capacities of Ca4Mg2Ce1 decreased from 28.wt % after the first cycle to 22 % in the 25 cycles. After 45 cycles, the overall decay of the CO_2 uptake capacities from the capacity of the first cycle was calculated to be 25 % for Ca6Mg2Ce1 , 29 % for Ca4Mg2Ce1 and 39 % for CaO.

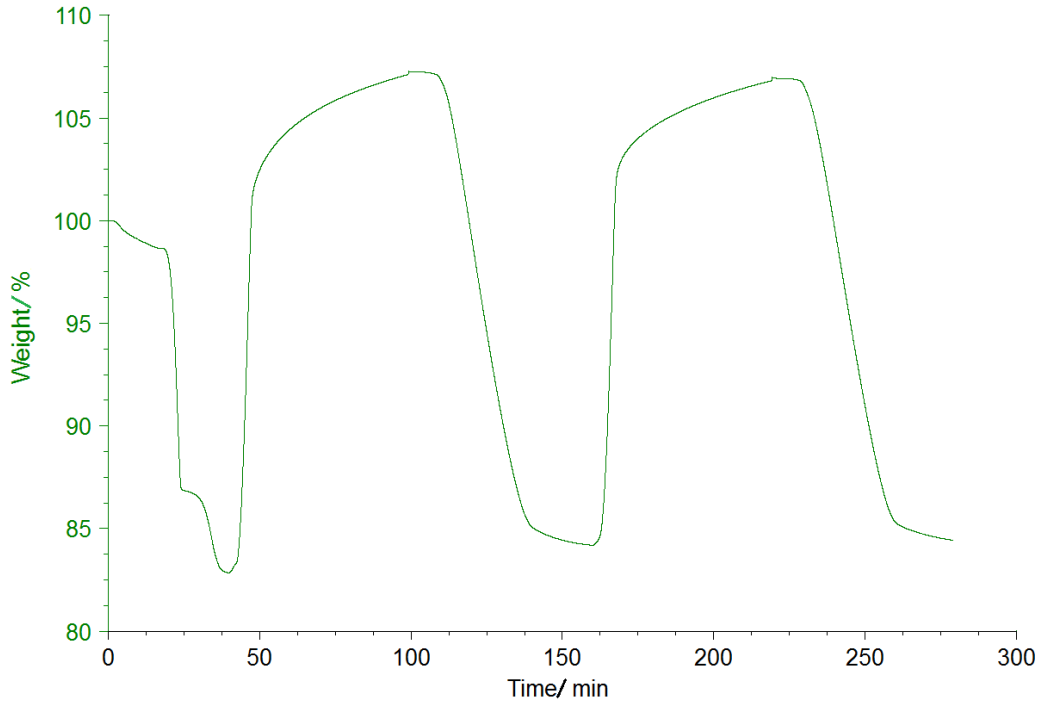

Figure 4.13 Carbonation/ de-carbonation curves of Ca6Mg2Ce1 sample at 700 °C.

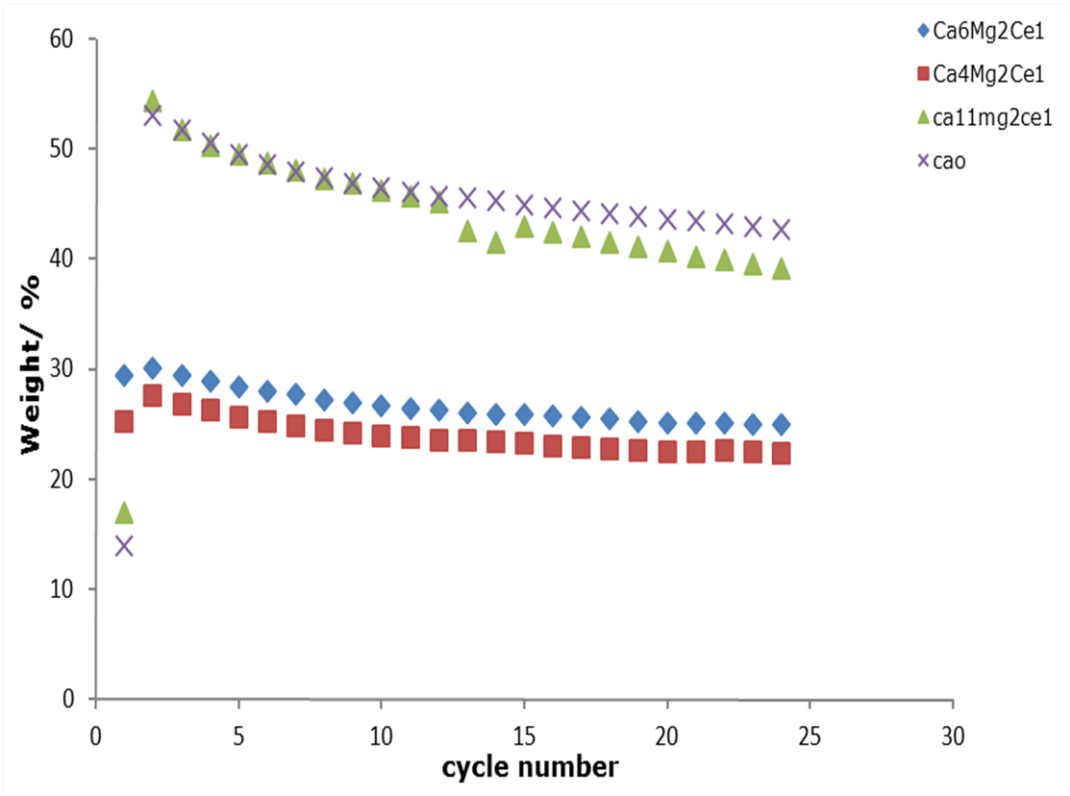

Figure 4.14. The sorbents CO_2 uptake capacities in weight percentage over 25 cycles in carbonation conditions:700°C, 60 min in CO_2 flow rate of 50 ml/min and de-carbonation conditions: 700°C, 60 min in N_2 flow rate of 350 ml/min.

Table 4.5. The sorbent's CO_2 uptake capacities in molar percentages over 45 cycles.

Sample	Molar CO_2 uptake capacity (*)/ mol %	Molar CO_2 uptake capacity (*) (After 1 cycle)/ mol %	Molar CO_2 uptake capacity (*) (After 25 cycles)/ mol %	Molar CO_2 uptake capacity (*) (After 45 cycles)/ mol %
Ca4Mg2Ce1	66	72	58	58
Ca6Mg2Ce1	66	68	57	55
Ca11Mg2Ce1	30	92	69	N/A
CaO	18	68	55	50
Ca1Mg2Ce1	69	78	N/A	N/A

* Based on CaO reacts with 78% wt CO_2 to form $CaCO_3$

From Figure 4.14 and Table 4.5, it was concluded that the stability of CO_2 uptake capacity results from small grains and porous surfaces. These results indicate that MgO and CeO_2 addition helped to achieve this stability. The addition of these inerts with certain percentage to CaO can effectively prevent the agglomeration and size growth of the CaO during carbonation /de-carbonation multi-cycles as previously discussed in section 4.3 and 4.5. However, the CaO content affects the sorbent reactivity. A very high CaO content is not favorable due to low content of inert material whereas, low content of CaO results in less amount of the active CaO and accordingly less CO_2 uptake capacity. In spite of the reasonable sorbent stability of Ca6Mg2Ce1, as it maintained their CO_2 uptake capacity over 45 cycles, see Figure 4.15, it is necessary to compromise the overall CO_2 uptake capacity with the sorbent stability during cycling.

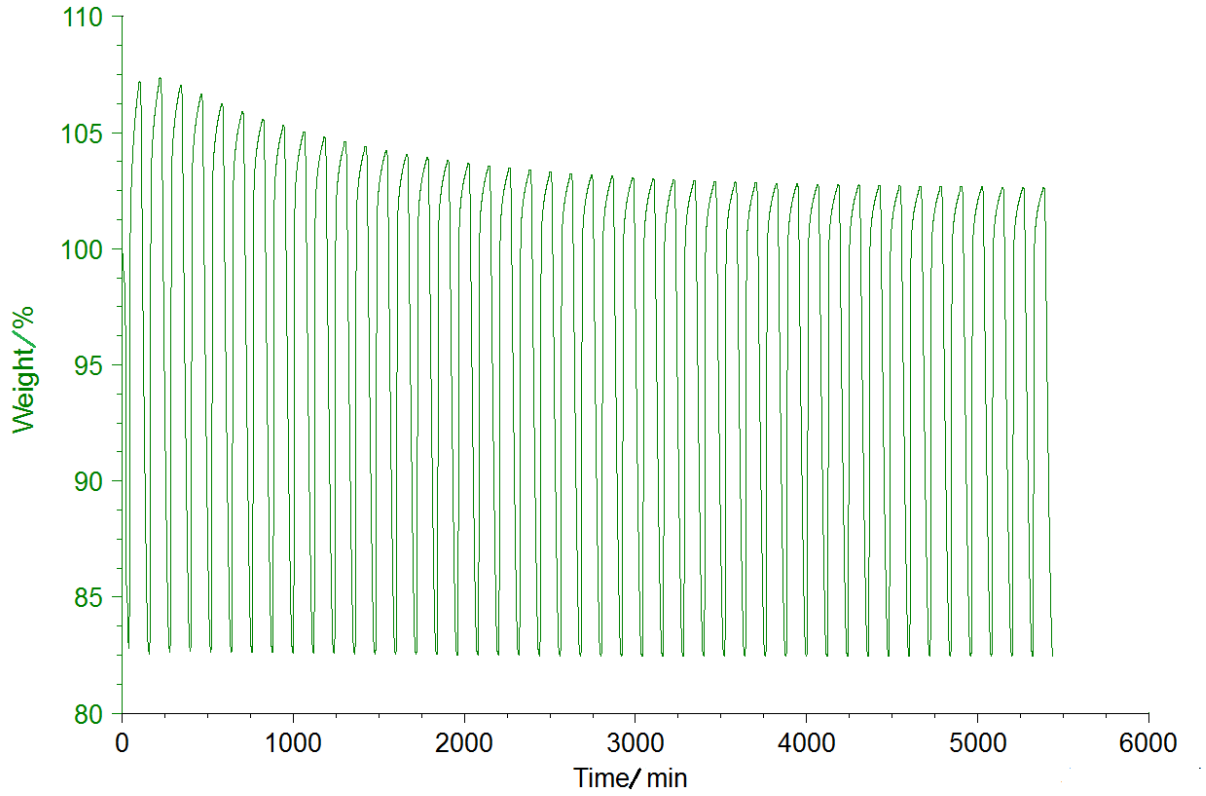

Figure 4.15. TGA profile of Ca6Mg2Ce1 over 45 cycles of carbonation/de-carbonation in carbonation conditions:700°C, 60 min in CO_2 flow rate of 50 ml/min and de-carbonation conditions: 700°C, 60 min in N_2 flow rate of 350 ml/min.

The improved stability of Ca6Mg2Ce1 sample during 45 cycles of carbonation/de-carbonation suggests its potential for the enhancement of ethanol steam reforming. The increase of the CO_2 uptake capacities in all samples after the first cycle indicates a microstructure change after the first de-carbonation reaction. The CO_2 driving off in de-carbonation reaction and changes in the surface particle sizes from $CaCO_3$ back to CaO may result in the formation of micro-cracks on the surface which would facilitate CO_2 movement during the next carbonation steps.

4.7. Characterisation of the sorbents after cycling.

In order to relate the changes in CO_2 uptake capacities of the prepared sorbents to the changes of their textural and crystalline features, XRD, SEM, BET and porosity tests were conducted for the selected sorbent after 1 cycle, 25 cycles and 45 cycles. As each cycle

consists of carbonation and de-carbonation steps, the examined samples were in the de-carbonated phase.

4.7.1. X-ray diffraction (XRD)

Powder X-ray diffraction (XRD) patterns of the selected sorbents during cycling were reordered and displayed in Figures 4.16-4.20. It was observed that CaO, MgO and CeO_2 peaks in all of the samples displayed intensity after the first cycle compared to the sample before the carbonation reaction. (Matjushi et al., 1997) reported that as the crystallinity decreased i.e. the peaks become broader and less intense, which indicate the gradual conversion to an amorphous structure in all the prepared samples. The CaO, MgO and CeO_2 peaks in the cycled samples appeared at the same values of 2θ (degrees) in the samples before cycling indicating no change in the unit cell. It was noticed that CaO carbonate was present in all of the cycled samples, except the 45 cycles of Ca4Mg2Ce1. CaO also did not appear in the first cycle of Ca1Mg2Ce1.

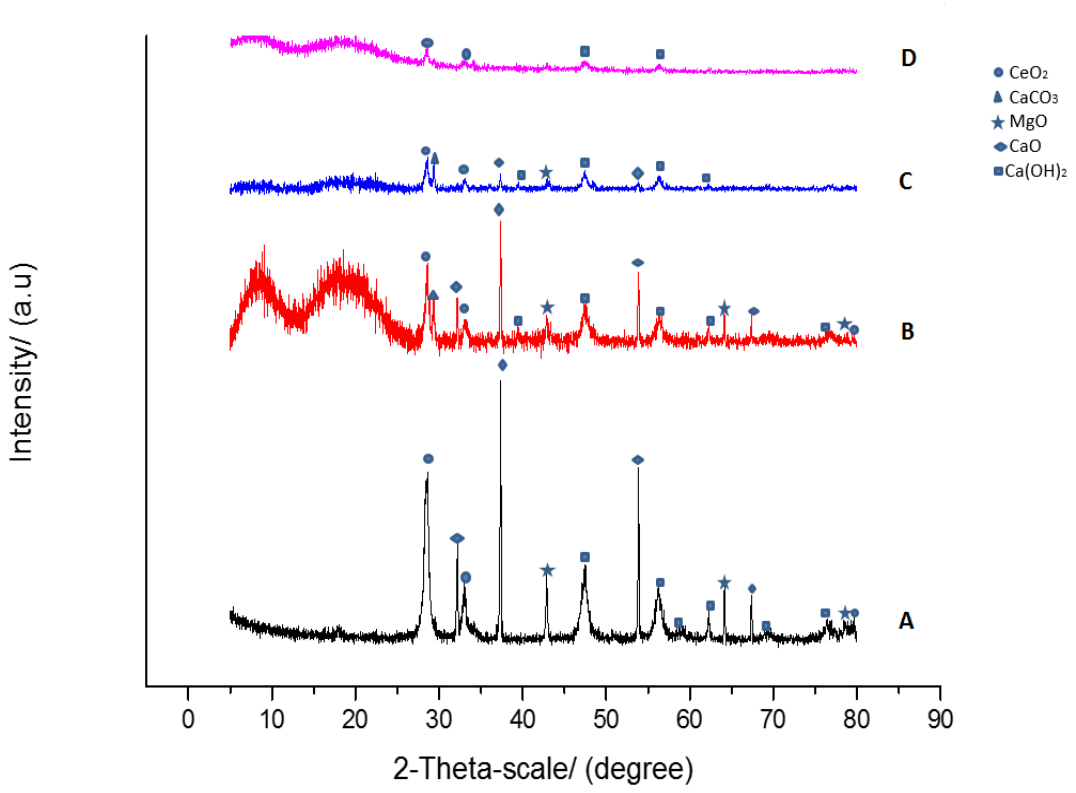

Figure 4.16. XRD patterns of Ca4Mg2Ce1, fresh sample (A) after first cycle (B) after 25 cycles (C) after 45 cycles (D) before CO_2 uptake.

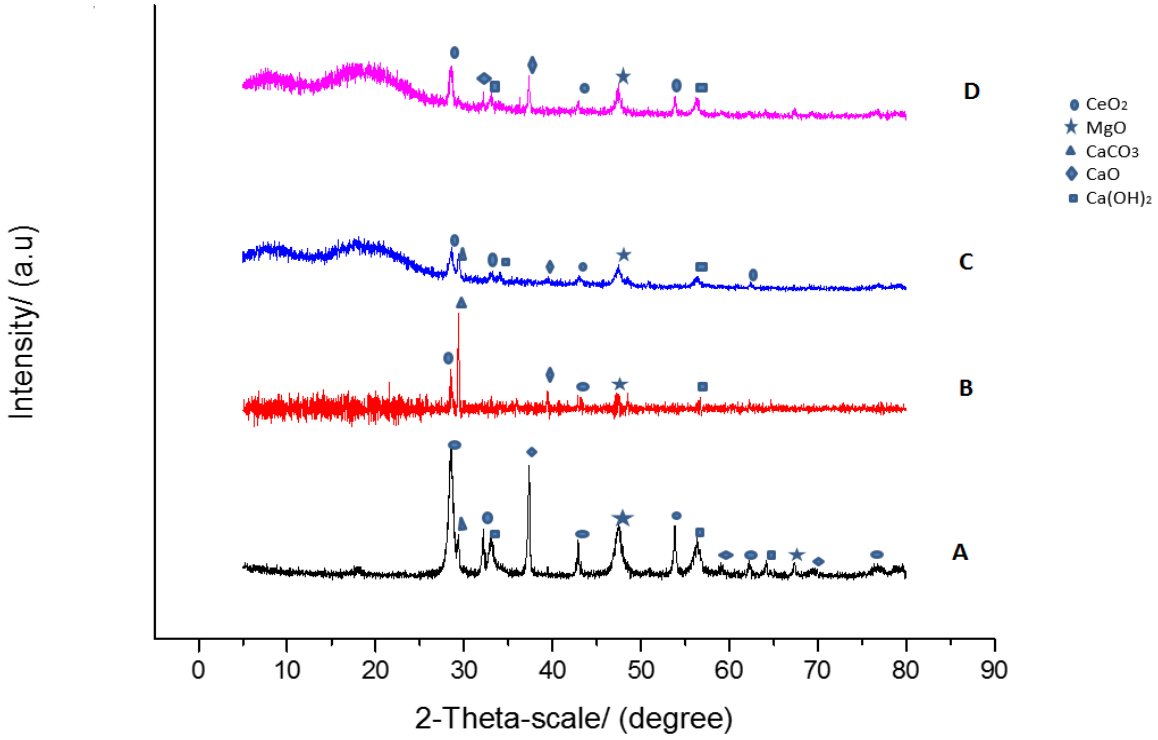

Figure 4.17. XRD patterns of Ca6Mg2Ce1, fresh sample (A) after first cycle (B) after 25 cycles (C) after 45 cycles (D).

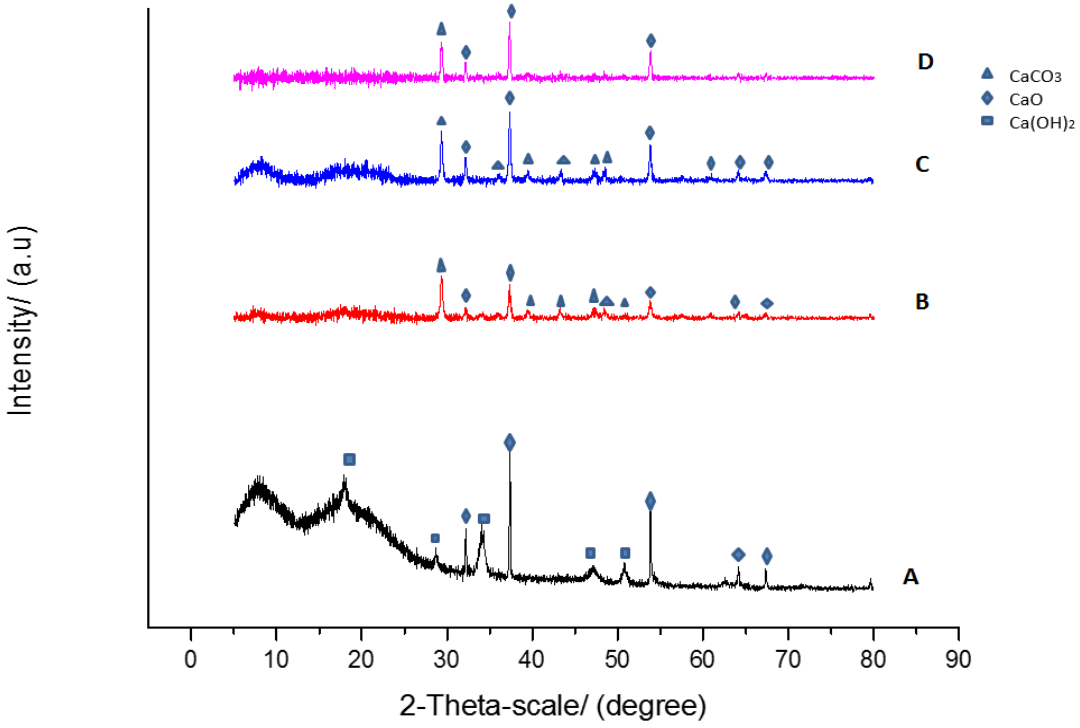

Figure 4.18. XRD patterns of CaO, fresh sample (A) after 1cycle (B) after 25 cycles (C) after 45 cycles (D).

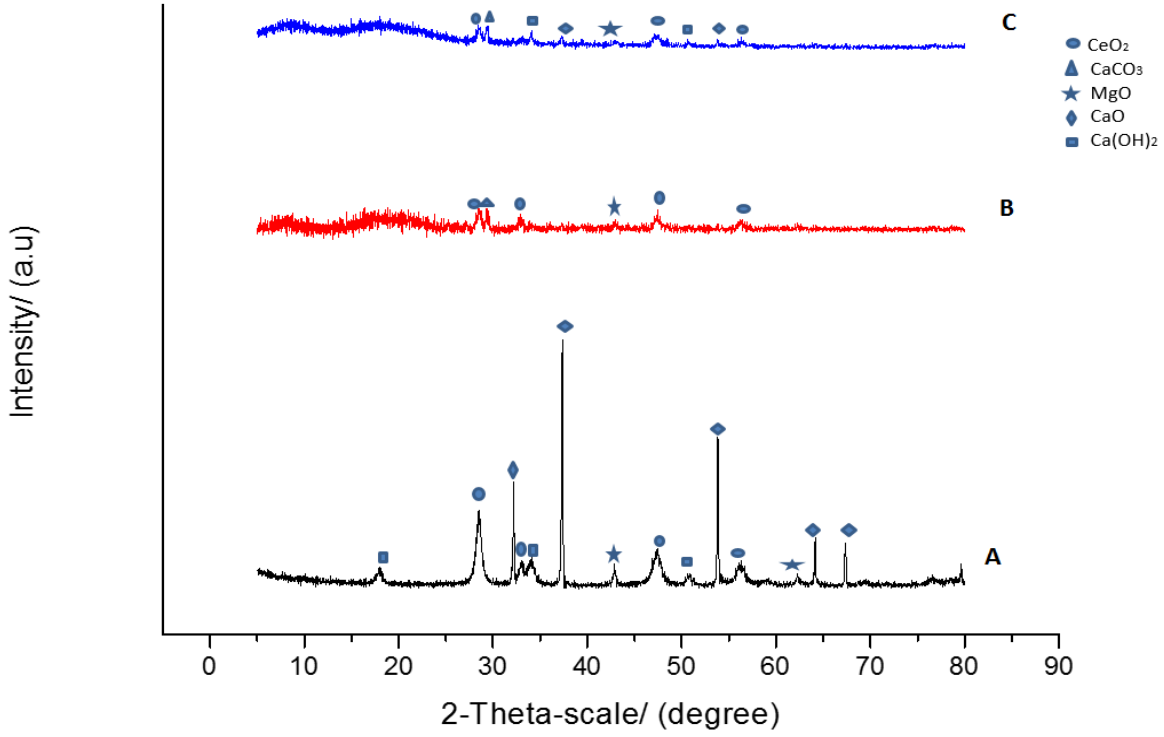

Figure 4.19. XRD pattern of Ca11Mg2Ce1, fresh sample (A) after 1cycle (B) 25 cycles (C).

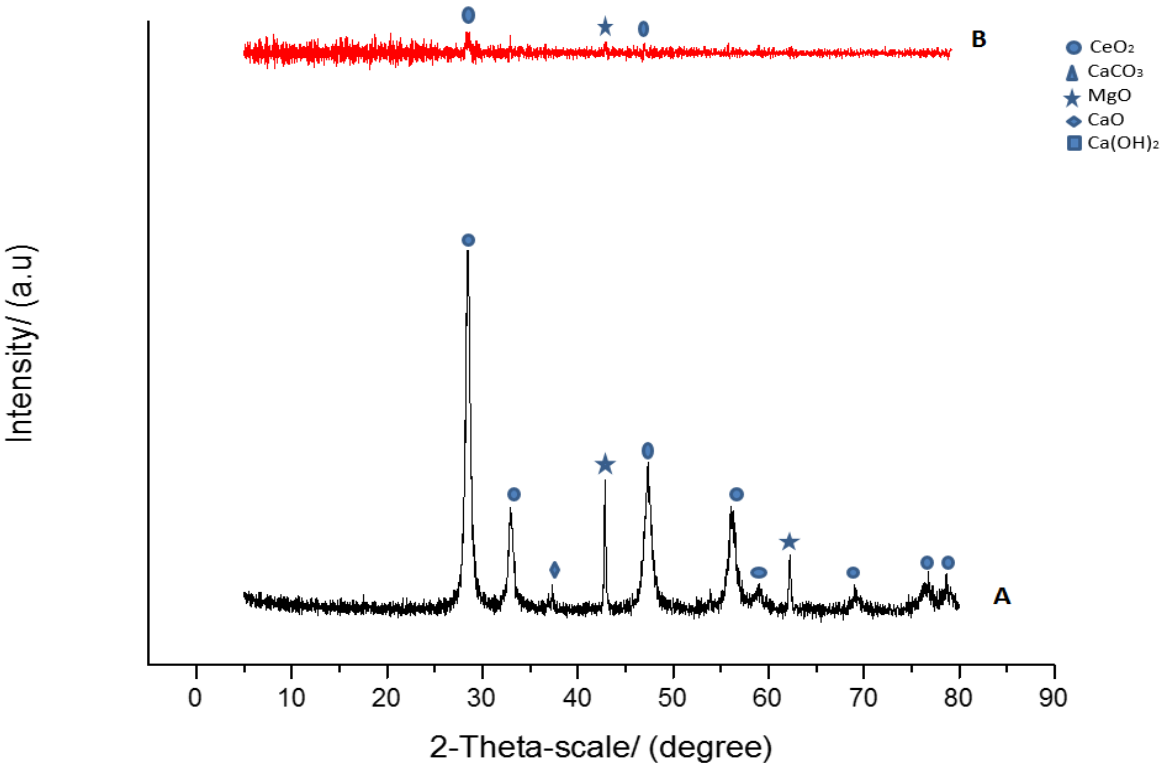

Figure 4.20. XRD pattern of C1Mg2Ce1, fresh sample (A) and after 1cycle (B).

Table 4.6. The crystallite sizes of the adsorbents components before CO_2 uptake and after the first cycle.

sample	CaO crystallite size/nm	CaO crystallite size after the first cycle/nm
Ca4Mg2Ce1	219	133
Ca6Mg2Ce1	408	188
Ca11 Mg2 Ce1	107	61
CaO	116	47

It can be observed from Table 4.6 that for all samples, the crystallite sizes of CaO after the first cycle was approximately half of the value for the sample before CO_2 uptake. It may also be observed that the CaO peak intensity values corresponding to the CaO crystallite sizes of these samples during cycling. The decrease of the CaO crystallite size confirmed the significant changes of CaO crystalline structure after the first carbonation/de-carbonation cycle as it was gradually converted to an amorphous structure.

4.7.2. Scanning electron microscopy (SEM)

The SEM micrographs obtained for the cycled samples were shown in Figures 4.21- 4.25. The significant difference in the surface micro-morphology of all samples after cycling can be observed. The SEM images of the samples which exhibit relatively stable reactivity, i.e. Ca6Mg1Ce1, Ca4Mg1Ce1, see Figure 4.21 and 4.22, maintain their rough and porous surface feature after 25 cycles. On the contrary, CaO and Ca11Mg2Ce1 exhibited smoother surface after 25 cycles compared to their images after the first cycle, see Figure 4.23-4.24. Ca1Mg2Ce1 with low CaO content samples had also preserved its porous surface after the first cycle but, due to its low CO_2 uptake, no further cycling experiments were done for this sample, see Figure 4.25.

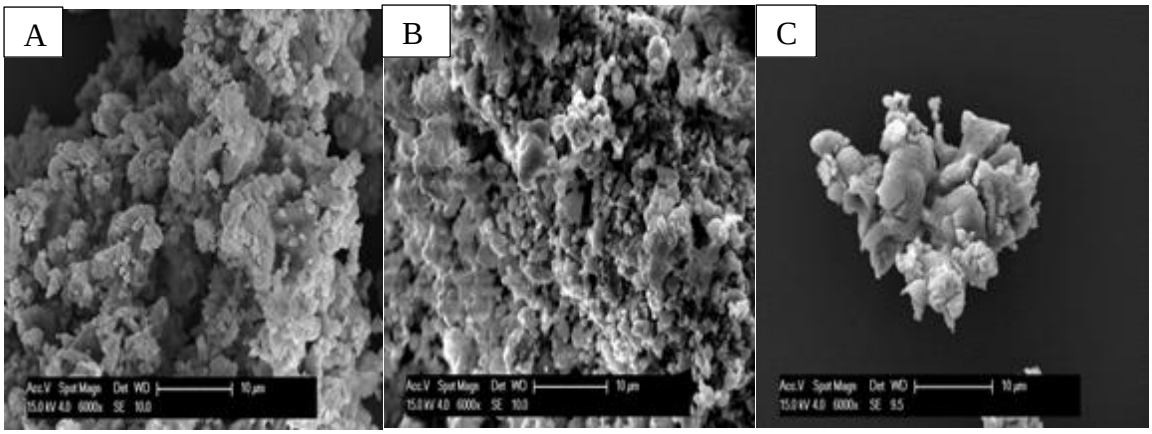

Figure 4.21.SEM images of Ca6Mg2Ce1 (A) after first cycle (B) after 25 cycles (C) 45 cycles.

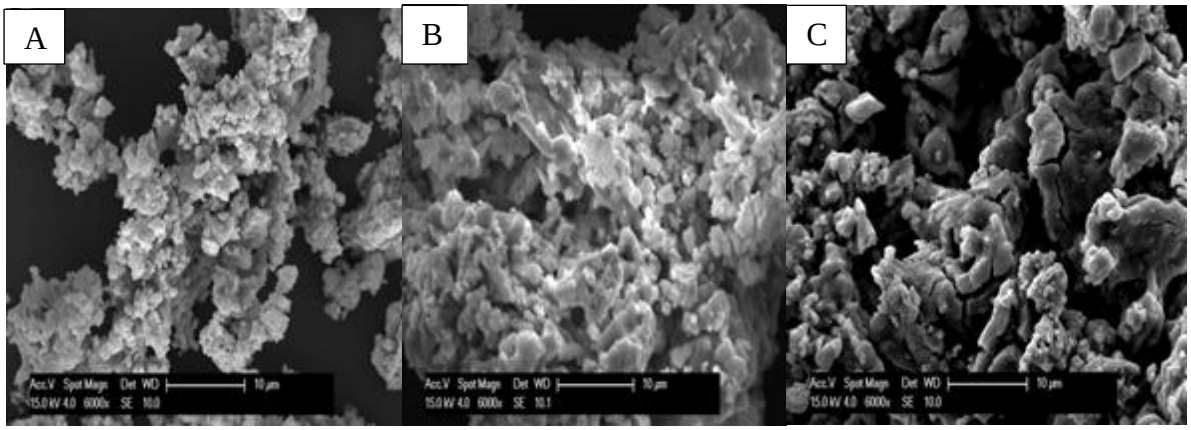

Figure 4.22. SEM images of Ca4Mg2Ce1 (A) after first cycle (B) after 25 cycles (C) after 45 cycles.

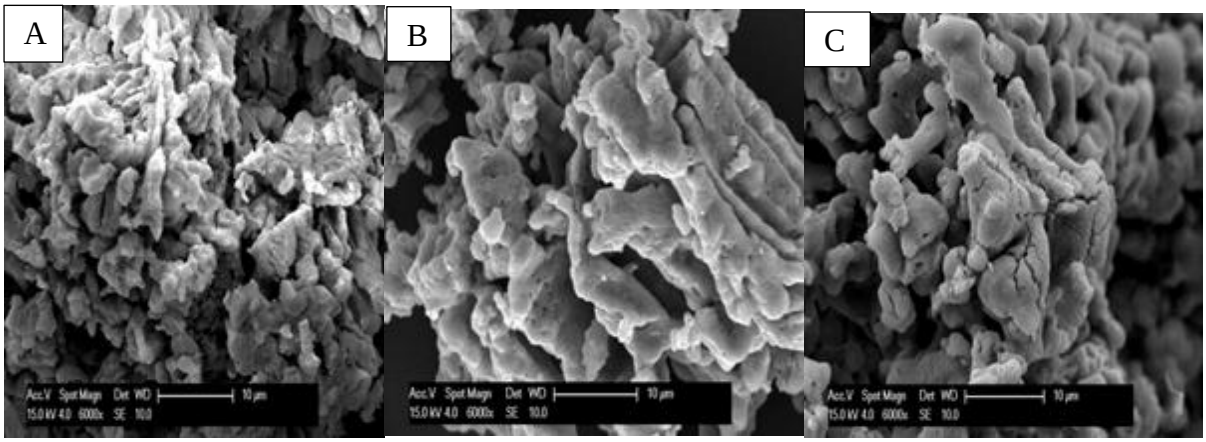

Figure 4.23. SEM images of Ca11Mg2Ce1 (A) after first cycle and (B) after 25 cycles.

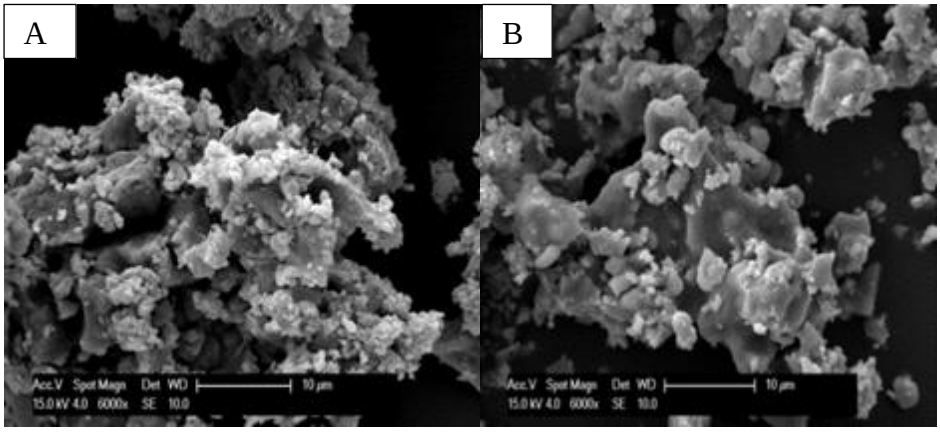

Figure 4.24. SEM images of Ca11Mg2Ce1 (A) after first cycle and (B) after 25 cycles.

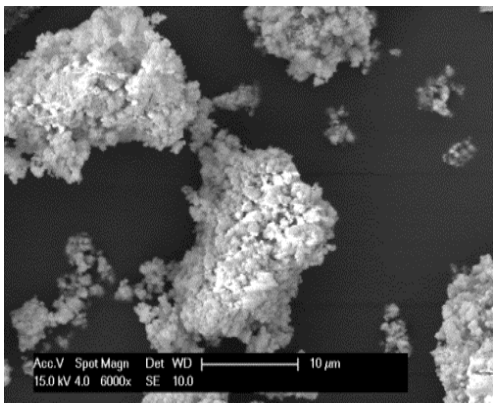

Figure 4.25. SEM images of Ca1Mg2Ce1 after the first cycle.

Generally, the SEM images of all the sorbents after cycling showed larger grains and smoother surfaces. Particularly, smooth surface appeared after 25 cycles in CaO and Ca11Mg2Ce1 which may have been to the rapid deactivation of these sorbents with higher CaO content. Whereas, the smooth surfaces became obvious after 45 cycles in samples Ca6Mg2Ce1 and Ca4Mg2Ce1. The smooth surface indicates that the surface particles merged together due to the CaO sintering. The CaO sintering led to a decay in the sorbent activity during the carbonation/ calcination cycles (Manovic and Anthony, 2009). Large cracks were observed after 45 cycles in Ca6Mg2Ce1, Ca4Mg2Ce1 and CaO. The size of the cracks was less than 10 µm. These cracks may have resulted from the reversible particles size changes of CaO converting to $CaCO_3$, during the multiple carbonation/de-carbonation cycles, in addition to the CO_2 driving off after the de-

carbonation reaction. The carbonated CaO ($CaCO_3$) molar volume (36.93 cm^3/mol) is estimated to be double of the CaO molar volume (16.7 cm^3/mol).

4.7.3. Measurement of surface area and porosity.

The surface areas for the selected samples after the first cycle, 25 cycles and 45 cycles were obtained using the Brunauer-Emmett-Teller (BET) method, as described previously in section (3.5.3). Whereas, the porosity values after cycling were measured using the mercury intrusion porosimetry in section (3.5.4). Figures 4.26,4-27and 4-28 shows that after the first cycle, the surface areas of Ca11Mg2Ce1, CaO and Ca1Mg2Ce1 samples decreased dramatically from 150, 212 and 230 m^2/g respectively to 11, 2 and 3 mg^2/g respectively. The surface values in all samples remained relatively low, less than (6 mg^2/g) after 25 and 45 cycles. After the first cycle, the porosity of Ca6Mg2Ce1 and Ca4Mg2Ce1 had a slight decrease from 66% and 72% to 51% and 57% respectively. Whereas, Ca11Mg2Ce1 and CaO porosities dropped sharply from 71% and 41% after the first cycle to 38% and 18%, respectively. It was observed that the porosity of a fresh C6Mg2Ce1 sample (66%) remained relatively stable over 45 cycles calculated as 51 %, 50 %, 47 % after 1, 25, 45 cycles respectively. The stable porosity of the Ca6Mg2Ce1 sample confirmed the observed relationship between the porosity and the stability of CO_2 uptake capacity over the multiple carbonation/de-carbonation cycles. Further investigation of pore distribution changes in the selected samples during cycling are discussed in section (4.7.3.1).

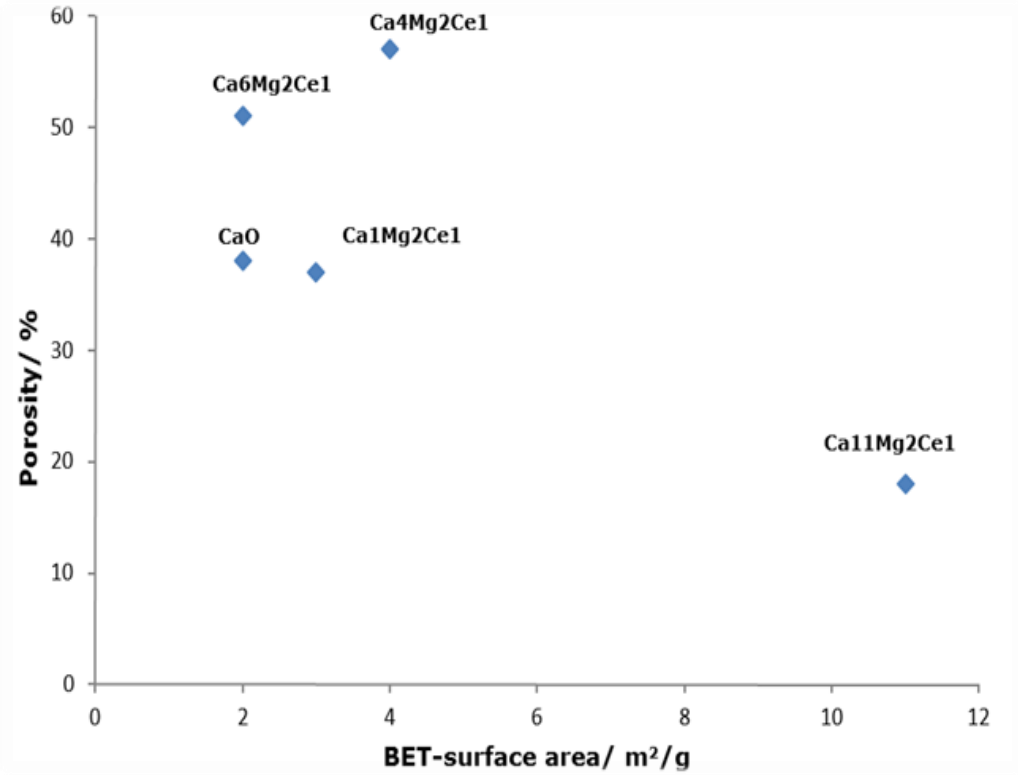

Figure 4.26. BET and porosity test of the selected sorbents after the first cycle.

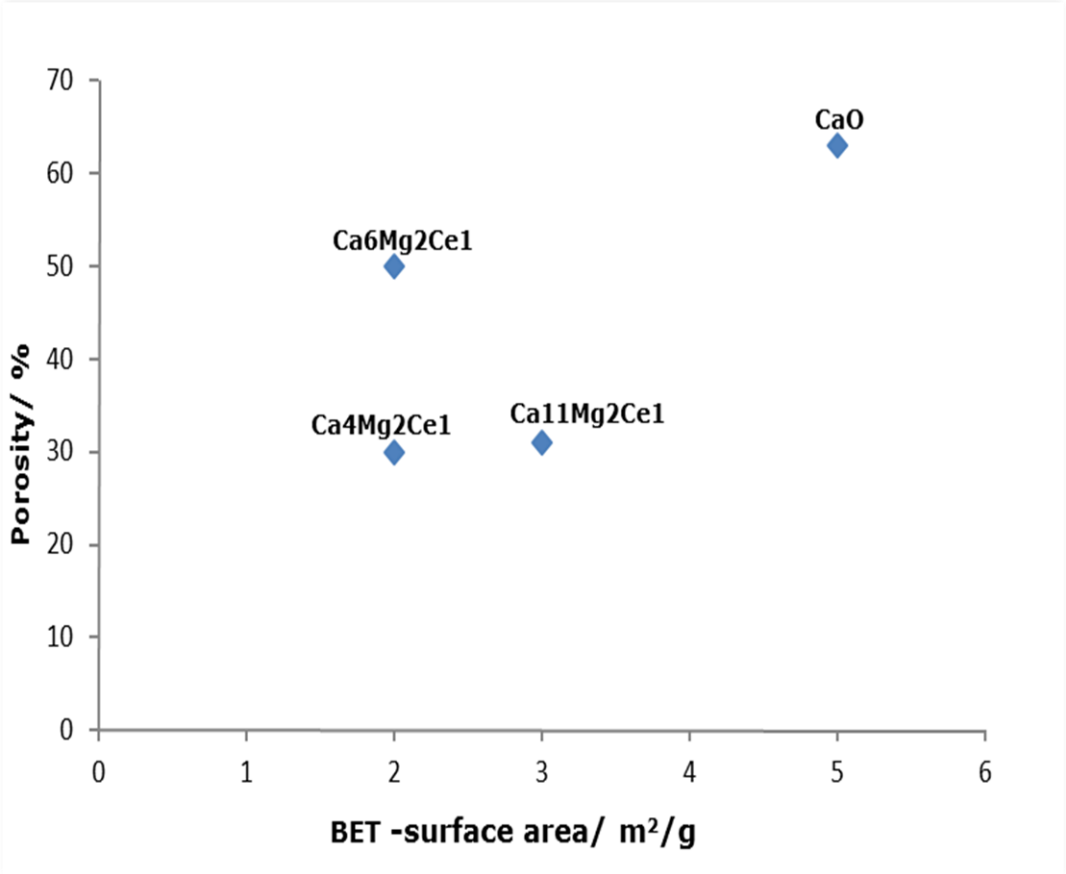

Figure 4.27. BET and porosity test of the selected sorbents after 25 cycles.

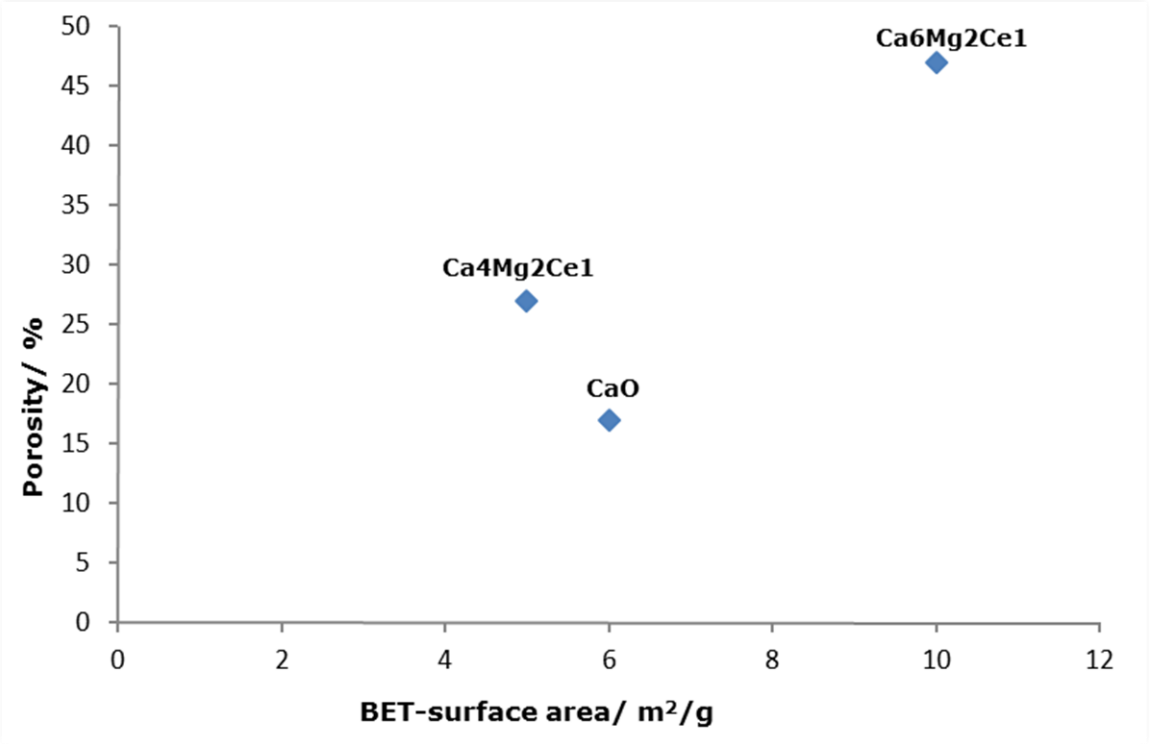

Figure 4.28. BET and porosity test of the selected sorbents after 45 cycles.

4.7.3.1. Pore size distribution (PSD)

PSD can provide a breakdown in the type of pores between micropores, mesoporous and macropores presence. Adsorption/absorption capacity of porous solids are closely related to the pore size distribution (PSD)(Lopez-Ramon et al., 1997). The adsorption isotherm is related to PSD according to:

$$N(P) = \int_0^\infty \rho(P, w) f(w) dw \quad (4.1)$$

where:

$N(P)$: the number of the adsorbed moles per unit mass of the adsorbent at pressure *p*/pa.

$\rho(P,w)$: the adsorbate density in a pore width w at pressure p" single-pore isotherm function"/g/cm^3.

$f(w)$: the PSD, strictly dV/dw where V is the total pore volume/cm^3 (Lopez-Ramon et al., 1997).

The PSD was calculated by varying $f(w)$ until equation (4.1) was closely satisfied.

Pores size distribution (PSD) for the selected sorbent was monitored over the cycling. The data were obtained from mercury intrusion and are shown in Figures 4.27. It was observed from Figure 4.29 that, the cumulative volume of the intruded pore in the range >10 μm was larger than the cumulative volume of intruded pore in the range <10 μm, which may indicate that smaller pores are larger in number compared to wide pores. In all samples, the maximum cumulative volume of the intruded pores in both the range >10 μm, and <10 μm increased after the first cycle then decreased after 25 cycles and then increased slightly again after 45 cycles. It is worth mentioning that the large cracks seen in the scanning electron microscopic micrographs after 45 cycles in the all samples were reflected in the MIP measurements in the small range from in the range 1-10μm.cumulative cumulative

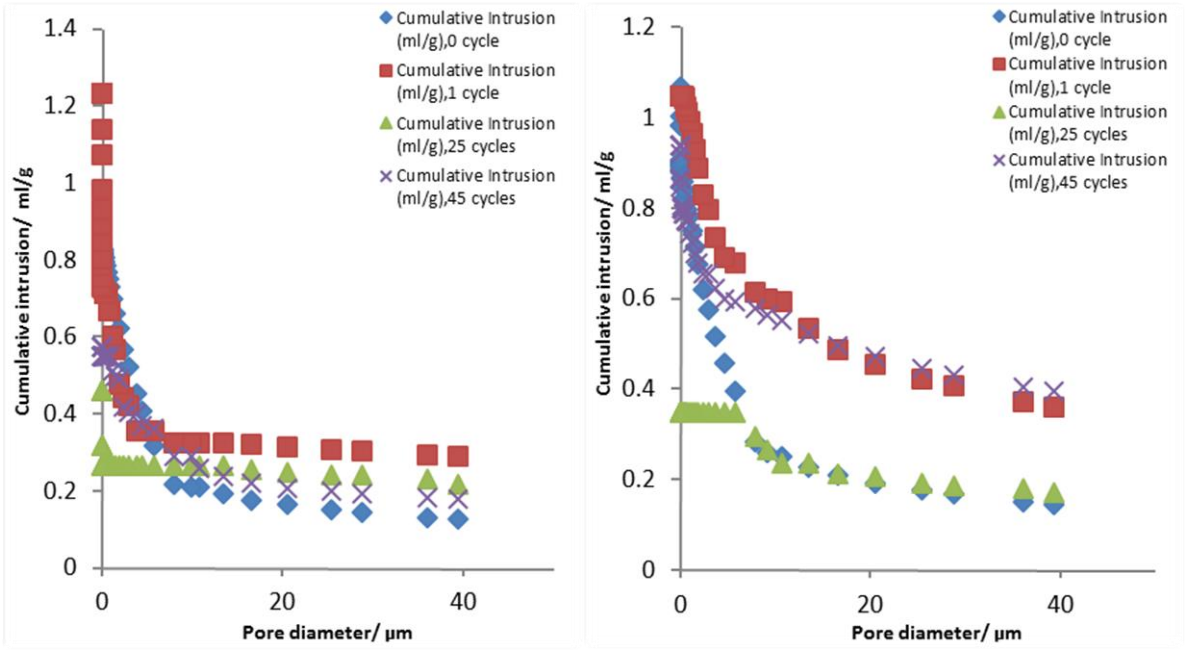

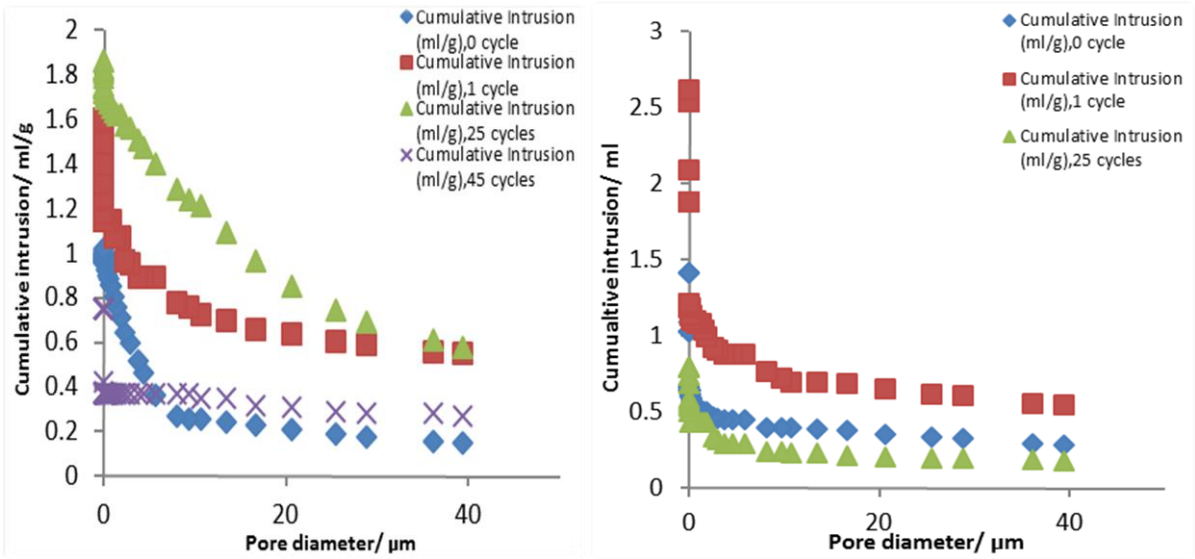

Figure 4.29. Pore cumulative intrusion volume vs pore diameter of the selected sorbents after cycling (A) Ca4Mg2Ce1, (B) Ca6Mg2Ce1,(C) CaO and (D) Ca11Mg2Ce1.

Smaller pores in the range 1-10µm displayed more changes after cycling compared to pores <10µm which may indicate that pores within the range of 0-10µm were the most affected region by the size changes during cycling. This could be explained by the premise that the smallest pore exposed to pore blocking by the increase in of carbonate

layer (Lu et al., 2008b). The sorbent pores were progressively blocked or became inaccessible due to their filling with the product $CaCO_3$ during the multiple cycles. The change in pores size resulted in lower CO_2 uptake. It was reported that the cycled limestone usually display growing macrospores accompanied with the smaller pores shrinkage (Abanades and Alvarez, 2003, Sun et al., 2007b). The growth in the larger pores and shrinkage of the smaller pores indicates the occurrence of the intermediate stage solid-state sintering (German, 1996, Sun et al., 2007a). In addition to that, the presence of CO_2 was reported to accelerate sintering (Sun et al., 2007a, Borgwardt, 1989, Ewing et al., 1979, Beruto et al., 1984). Sintering of CaO due to the extended thermal exposure during cycling may also cause the pores' closure.

4.8. Catalyst/sorbent mixture preparation and characterization

The iron oxide (Fe_2O_3) catalyst was mixed with the Ca6Mg2Ce1 sorbent using the co-precipitation method described in section (3.1). The catalyst /sorbent mixture was first prepared in 1:1 and then in 1:6 weight percentage. All the characterisation tests were done in 1:1 weight percentage of catalyst /sorbent mixture. While the SESR tests were conducted by using the catalyst /sorbent mixture of 1:6 weight percentages. The mixed sorbent Ca6Mg2Ce1 with Fe_2O_3 catalyst was exposed to 100% CO_2 stream to investigate the effect of adding Fe_2O_3 catalyst on CO_2 uptake capacity of the sorbent, see Table 4.7. Table 4.7 also shows the comparison results between the BET surface area and porosity measurements between the Ca6Mg2Ce1 alone and Ca6Mg2Ce1 mixed with Fe_2O_3. XRD patterns for sorbent/catalyst mixture before and after CO_2 uptake are shown in Figure 4.30. $Ca_2Fe_2O_5$ appearance as transition phase was observed in the sample before CO_2 uptake. Figure 4.31 shows the SEM images of the Fe_2O_3/Ca6Mg2Ce1 mixture, where no significant textural difference was observed on the Fe_2O_3/Ca6Mg2Ce1, compared to Ca6Mg2Ce1 alone.

Table 4.7. Comparison results of CO_2 uptake, BET surface area and porosity measurements for Fe_2O_3 and Fe_2O_3 /Ca6Mg2Ce1 mixture.

Sample	CO_2 uptake/ wt. %	Surface Area / m^2/g	Porosity/%
Ca6Mg1Ce2	30	4	66
Fe_2O_3/Ca6Mg2Ce1	8	9.4	65

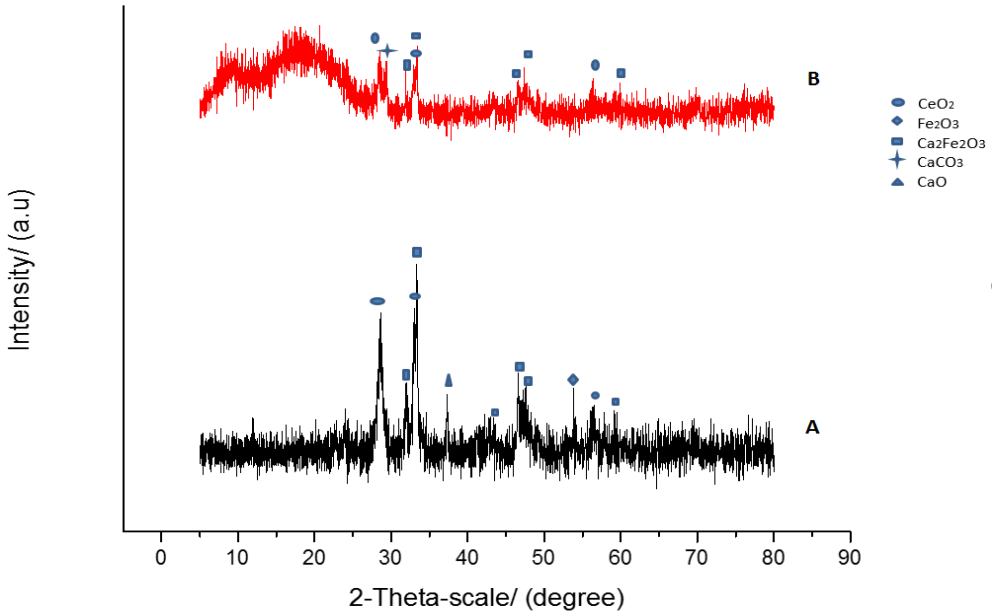

Figure 4.30. XRD patterns of Fe_2O_3/Ca6Mg2Ce1 mixture (A) before CO_2 uptake (B) after CO_2 uptake 25 cycles.

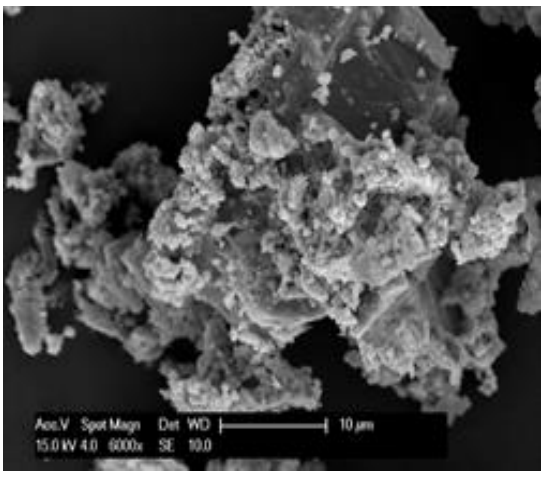

Figure 4.31. SEM image of the Fe_2O_3/Ca6Mg2Ce1 mixture sample before steam reforming reaction.

As the Fe_2O_3/Ca6Mg2Ce1 mixture was prepared in weight percentage of 1:1. TGA, BET and surface area results were in the expected range for the half amount of the sorbent Ca6Mg2Ce1 alone. The latter results revealed that the mixed Fe_2O_3/Ca6Mg2Ce1 has very close surface area measurement and same porosity as the Ca6Mg2Ce1 sorbent alone. It could be concluded that the addition of Fe_2O_3 to Ca6Mg2Ce1 using co-precipitation method did not affect the sorbent properties.

4.8.1. Iron oxide catalytic reducibility test

Catalyst reducibility was investigated by temperature programmed reduction (TPR) using H_2 as reducing agent to determine the minimum temperature for the iron oxide (Fe_2O_3) reduction to metallic iron (Fe). It had been reported that Fe_2O_3 reduction undergoes two-stage reduction to Fe_2O_3 converts to Fe_3O_4 and then Fe_3O_4 converts to Fe (Yamaguchi et al., 2011, Galvita and Sundmacher, 2007). Similarly, in this study, Fe_2O_3 showed two distinct reduction peaks at 279°C and 327°C as shown in Figure 4.32 indicating stages I and II. At 534 °C, 30% of sample weight was reduced, which referred to the total oxygen content in Fe_2O_3, see Figure 4.32. Figure 4.33, shows Fe_2O_3/Ca6Mg2Ce1 reduction profile. XRD tests were performed to investigate the changes in iron oxide phases for the samples before and after the reduction, see Figure 4.34 and 4.35.

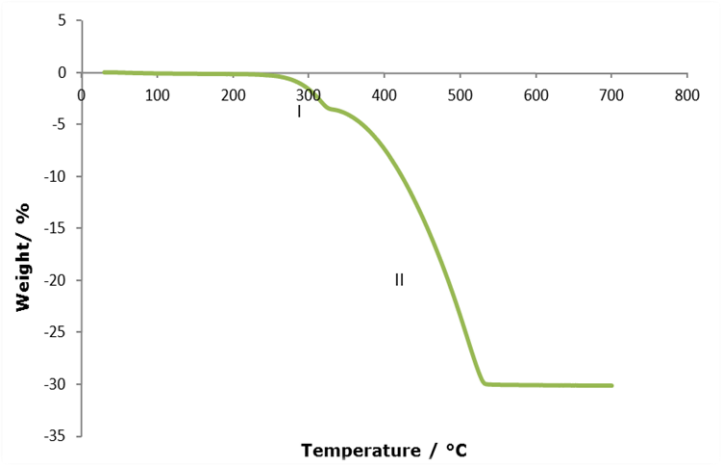

Figure 4.32. The reduction profile of (A) Fe_2O_3 obtained under temperature programmed with a ramping rate of 5°C/min to 900 °C under H_2 gas.

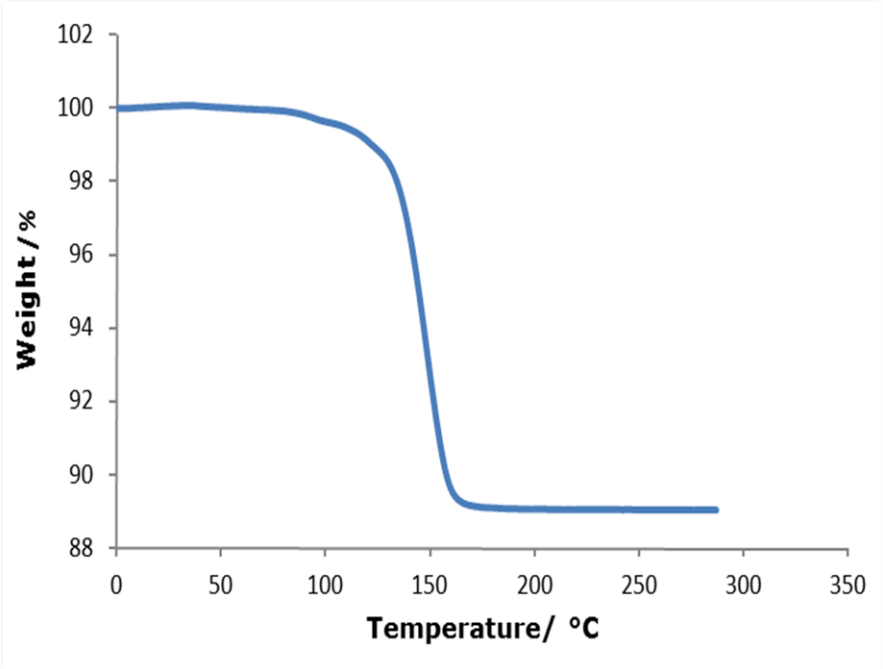

Figure 4.33. The reduction profile of Fe_2O_3/Ca6Mg2Ce1 obtained under temperature programmed with a ramping rate of 5°C/min to 900 °C under H_2 gas.

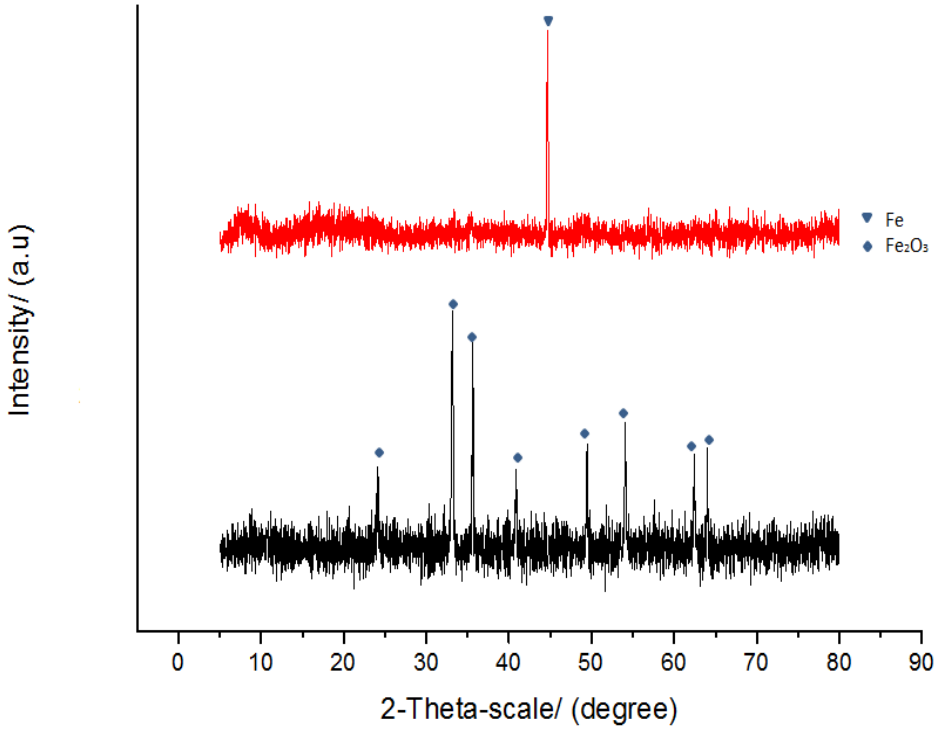

Figure 4.34. XRD patterns for Fe_2O_3 (A) before and (B) after temperature programmed with ramping rate of 5°C /min to 900 °C under H_2 gas.

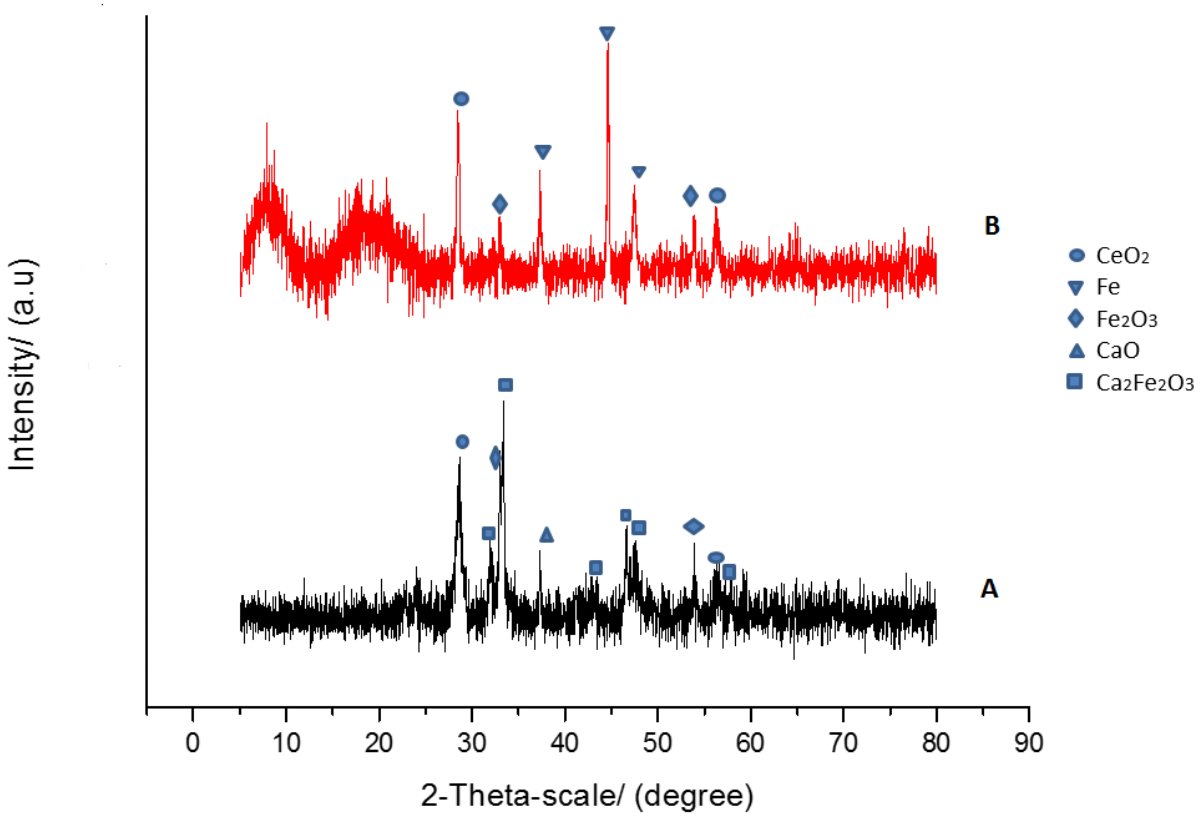

Figure 4.35. XRD patterns for Fe_2O_3/Ca6Mg2Ce1 (A) before and (B) after temperature programmed with ramping rate of 5°C/min to 900 °C under H_2 gas.

Figure 4.32 shows that 30% weight reduction of Fe_2O_3 alone sample was achieved which corresponding to 100% oxygen content removal in Fe_2O_3 (i.e. 30%). The reduction profile of Fe_2O_3/Ca6Mg2Ce1 sample obtained under the same reduction conditions in the TGA. It was observed that the Fe_2O_3/Ca6Mg2Ce1 reduction stabilized at 600 °C, with weight reduction percentage of 11%. As Fe_2O_3/Ca6Mg2Ce1 was done in 1:1 weight percentage, the weight reduction was expected to be 15 %. Figure 4.33 shows that only 11% weight reduction was achieved. This percentage was corresponding to 73% reduction of oxygen content of Fe_2O_3 in the mixed Fe_2O_3/Ca6Mg2Ce1. These results suggest that not all the oxygen content of Fe_2O_3 in the mixed Fe_2O_3/Ca6Mg2Ce1 was reduced. The XRD results reveal the presence of Fe_2O_3 phase in iron oxide alone sample and transition phase of $Ca_2Fe_2O_5$ in Fe_2O_3/Ca6Mg2Ce1 sample before the reduction tests, see Figures 4.34 and 4.35. $Ca_2Fe_2O_5$ belongs to the compound group with the general

formula of $A_2B_2O_5$ (A = Ca, Sr; B = Fe, Al). $Ca_2Fe_2O_5$ has also used in the field of catalysis (da Silva and Sombra, 2011).

$Ca_2Fe_2O_5$ may be responsible for the non-completion of total oxygen reduction as two oxygen molecules reacted with two molecules of Ca from $Ca_2Fe_2O_5$ to form two molecules of CaO, see equation 4.2 and 4.3. These results indicate that 73% of the reducible oxygen was in form of the Fe_2O_3 phase while 27% was in $Ca_2Fe_2O_5$. The later observation suggests that CeO_2 and the other oxides i.e. CaO and MgO show negligible oxygen reduction in the studied condition.

$$Fe_2O_3 + 3H_2 \rightarrow 2Fe + 3H_2O \quad (4.2)$$

$$Ca_2Fe_2O_3 + H_2 \rightarrow 2CaO + 2Fe + H_2O \quad (4.3)$$

However, the XRD patterns which are shown in Figure 4.35 confirm the presence of Fe_2O_3 in sample Fe_2O_3 as well as in Fe_2O_3/Ca6Mg2Ce1 after the reduction test. Generally, according to the Fe_2O_3 reducibility tests of both samples, the reaction temperature for SESR was studied in range >550 °C, see section (5.2.2)

4.9. Chapter summary.

The most commonly used sorbent is calcium oxide (CaO), which can repeatedly uptake CO_2 over multiple carbonation/de-carbonation cycles, see equation (2.8). CaO has been considered as a promising candidate due to its high CO_2 uptake capacity and low cost (Blamey et al., 2010). The main drawback of using the naturally existing CaO, such as dolomite and limestone for CO_2 capture, is its stability during carbonation/ de-carbonation cycles as it was reported to be dropped by 80% after 10-20 cycles. CaO sintering and particles agglomeration were suggested to be the main cause of this dramatical drop (Lopez Ortiz and Harrison, 2001). (Bandi et al., 2002) claimed that CaO could maintain its micro-structure over multiple carbonation/ de-carbonation cycles by the addition of an inert material.

This study involved the synthesis of CaO-based sorbents using magnesium oxide (MgO) and cerium oxide (CeO_2) as modification elements to enhance its capacity and stability for CO_2 capture. The co-precipitation method modified after (Park et al., 2012) was used to prepare the synthetic CaO-based sorbent from a nitrate precursor in different molar percentages. The calcination temperature of 650 °C for 3 h was used to eliminate the sorbent moisture content and other instable components. The carbonation performances of the prepared sorbents were evaluated in a thermo-gravimetric analyser, where 20-50g of the sample was exposed to 100% CO_2 gas stream at 700 °C. The prepared samples exhibit different CO_2 capture capacities. Particularly, Ca6Mg1Ce1 and Ca4Mg1Ce1 which had CO_2 uptake capacities of 29 wt. % and 25 wt %, respectively, were in the accepted range to be applied in SESR processes for CO_2 capture, i.e. 20-40 wt. % (Park and Yi, 2012a, Abanades et al., 2004, Yi and Harrison, 2005).

The kinetics of the carbonation reaction were studied by fitting isothermal sorption data with three different kinetic models. The CO_2 uptake profile of C6Mg2Ce1, C4Mg2Ce1 and Ca1Mg2Ce1 exhibited three different phases; while CaO and Ca11Mg2Ce1 exhibited two phases. The JMA (Johnson-Mehl-Avrami) model fitted best the first and second stages as expected for Ca4Mg2Ce1, where SC fitted the initial stage and JMA fitted the second

stage. While contracting volume model (CV2/3, with a growth velocity decreasing with time fitted the final stages. Two groups of the prepared samples were selected for the comparison and characterisation of the important microstructure properties that led to different CO_2 uptake capacities. Ca6Mg2Ce1 and Ca4Mg2Ce1 were the higher CO_2 uptake group. Ca11Mg2Ce1 with high CaO content and Ca1Mg2Ce1 with low CaO content were the poor CO_2 uptake group. Ca11Mg2Ce1 and Ca1Mg2Ce1 had CO_2 uptake capacities of 17 wt% and 7 wt% respectively. The prepared CaO pure sorbent was used in this comparison as a benchmark.

XRD, SEM, surface area and porosity tests were applied for the selected samples before the CO_2 uptake. These characterisation results suggested that the higher CO_2 uptake did not relate to larger surface but to its porous structure. In order to compare efficiently the CO_2 capture capabilities of the selected sorbents, their CO_2 capture capacities were investigated over 45 cycles of multiple carbonation/de-carbonation reactions. Unexpectedly, all the samples exhibited a higher CO_2 uptake after the first cycle. Ca11Mg2Ce1 had dramatically increased from 17 wt. % to 54 wt. %, whereas CaO increased from 14 wt. % to 53 wt. %. After 25 cycles, the CO_2 uptake capacities of Ca11Mg2Ce1 and CaO had dropped to 39 wt.% and 43 wt.%, respectively. The Ca6Mg2Ce1 sample showed a relatively stable CO_2 uptake capacity as the overall decay of the CO_2 uptake capacity after 45 cycles from the capacity of the first cycle was calculated to be 25 wt.%.

Characterisation tests of the selected samples after cycling revealed that the CaO crystallite size had decreased, the surface topography became smoother and micro-cracks were observed in the range of 1-10 μm. It is worth mentioning that the increase in CO_2 uptake of Ca11Mg2Ce1 and CaO after the first cycle was accompanied with a decrease in the surface areas from 150 and 212 m^2/g to 11 and 2 m^2/g respectively. This observation backed up the premise that a higher surface area was not the key factor for a higher CO_2 uptake. The investigation of the pore distribution in the selected samples revealed that pores >10 μm were exposed to volume changes during the

multiple carbonation/de-carbonation cycles. The CO_2 uptake capacity of Fe_2O_3 /Ca6Mg2Ce1 and the characterisation results showed that the sorbent properties were not changed by mixture with a Fe_2O_3 catalyst, using co-precipitation method. The reducibility test of Fe_2O_3 suggest that Fe_2O_3 is totally reduced to Fe in temperature >534°C. Therefore, the SESR reaction temperature were studied in temperature range >534°C.

CHAPTER FIVE

Activity tests for iron oxide catalyst and CaO-based sorbents in sorption enhanced ethanol steam reforming

5.1. Introduction

This chapter describes ethanol steam reforming reactions over the prepared iron oxide catalyst mixed with CaO-based sorbent. The experiments were done in a fixed bed reactor in order to study ethanol conversion, catalyst selectivity and sorbent activity under various operating conditions. The reactions were carried out for 3 hours at a series of temperatures of 550, 600, 650 and 700°C and atmospheric pressure; see section (5.2.2). A constant flow rate of premixed water and ethanol at molar ratios of 6 and 1 was introduced into the reactor. Comparison study of the effects of varying liquid hourly space velocity was also conducted in section (5.2.3). The possibility of carbon deposition was investigated for the used catalyst samples at 700 °C, see section (5.2.4). In order to investigate the catalytic behaviour and sorbent activity during long-term operation, stability test for 10 cycles equivalent to 30 hours on stream, at 700°C is also illustrated in section (5.4).

5.2. Chemical Equilibrium analysis of ethanol steam reforming

The reaction that converts ethanol into hydrogen in the presence of sufficient steam is shown in (equation 2.7). Ethanol decomposition (equation 5.1) and ethanol dehydration (equation 5.2) are the possible reactions in the case of insufficient steam (Haryanto et al, 2005). Numerous side reactions are reported in the steam reforming system, such as

methanation (equation 2.2), Water Gas Shift (WGS) (equation 2.3) and the Boudouard reaction equation (5.3).

Ethanol decomposition

$$C_2H_5OH \rightarrow CO + H_2 + CH_4 \quad (5.1)$$

Ethanol dehydration:

$$CH_3CH_2OH \rightarrow H_2C=CH_2 + H_2O \quad (5.2)$$

$$2CO \leftrightarrow CO_2 + C \quad (5.3)$$

These reactions produce hydrogen and carbon monoxide with a considerable reductive potential that could allow the reduction of iron oxide starting from hematite (Fe_2O_3) down to metallic iron (Fe) (Hormilleja et al., 2014). The chemical equilibria for the ethanol steam reforming (equation 2.7) and ethanol decomposition (equation 5.1) were predicted using the CEA program (Chemical Equilibrium with Applications) (Zehe, 2010). The CEA programme uses minimisation of Gibbs free energy to calculate the product concentrations at the chemical equilibrium of any reaction. The CEA was programmed to calculate all possible products by entering the moles of ethanol (1 mol) and water (6 mol) in the temperature range between 500-800 °C. Reaction output values obtained for every 50 °C interval at atmospheric pressure. The products of ethanol steam reforming for the steam to ethanol molar ratio of 6:1, are shown in Figure 5.1, whereas ethanol decomposition reaction is shown in Figure 5.2.

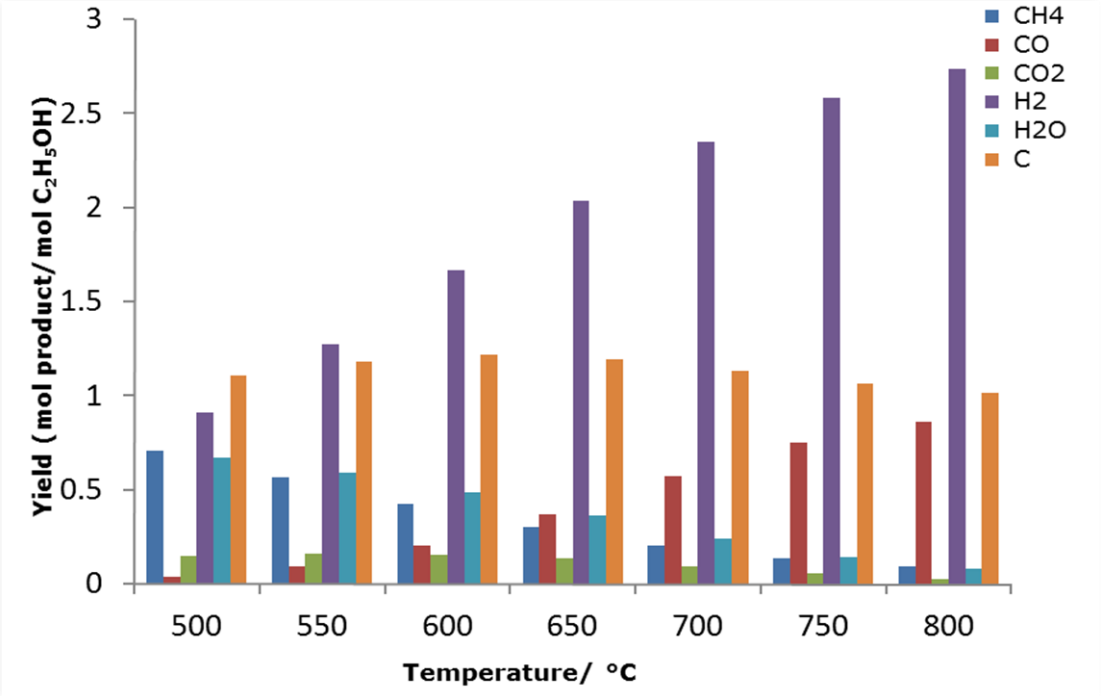

Figure 5.1. Products yields at equilibrium ethanol decomposition calculated by CEA modelling software at 101.325×10^3 Pa.

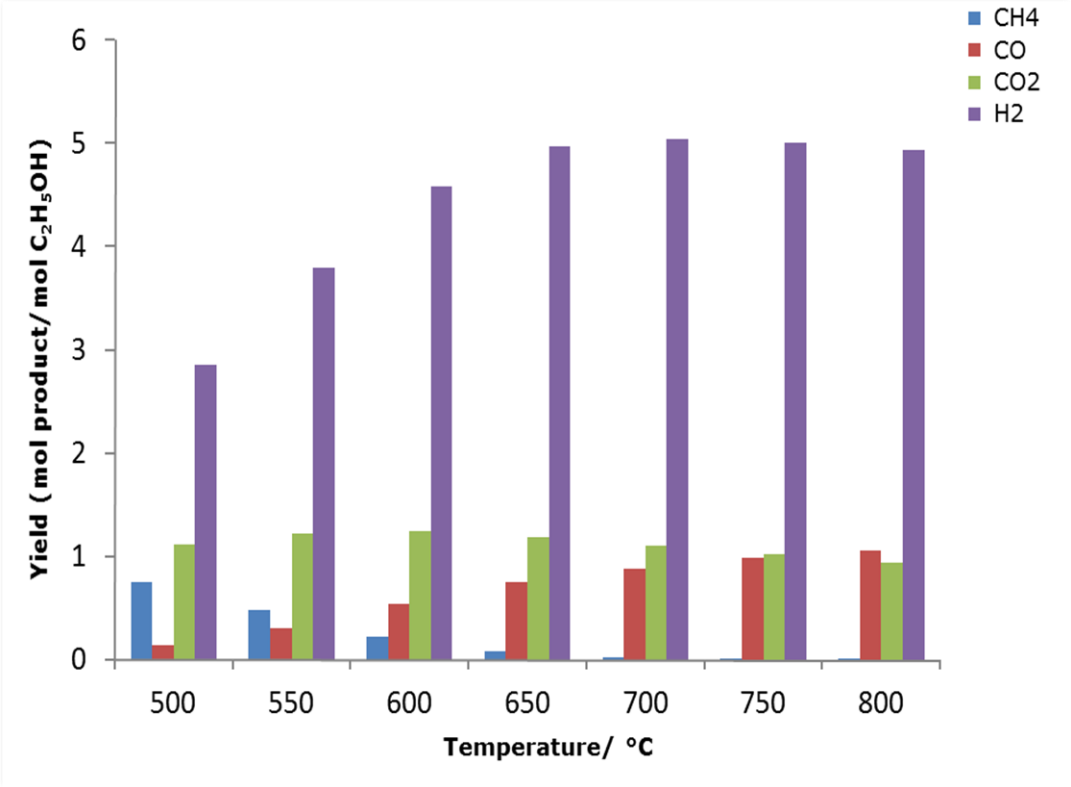

Figure 5.2. Products yields at equilibrium ethanol steam reforming at 101.325×10^3 Pa and H_2O/EtOH =6, calculated by CEA modelling software.

The equilibrium compositions obtained from the thermodynamic calculation for the ethanol decomposition reaction showed that the hydrogen increased while the yields of methane (CH_4) decreased concurrently, with increasing the operating temperature, see Figure 5.1. Carbon (C) yields were relatively stable, whereas carbon dioxide (CO_2) yields decreased due to the reverse of the WGS reaction at high temperature (>500°C). Alternatively, in the steam reforming of ethanol for H_2O/EtOH =6, hydrogen yields increased until 650°C and then stabilised. CH_4 concentration decreased to 700 °C and there was no evidence of CH_4 in temperature over 700°C. The CO yield increases whereas CO_2 was stable over the studied temperature range. The presence of water and C was the difference between ethanol decomposition and steam reforming, see Figure 5.2.

5.3. Sorption Enhanced ethanol steam reforming (SEESR) tests

Sorption enhanced ethanol steam reforming were investigated in a fixed bed reactor in terms of ethanol conversion and the amount of reformate produced at different reaction conditions. The experimental investigations were undertaken with three objectives, to study: effect of reaction temperature, effect of varying gas hourly space velocity and stability of the catalyst and sorbent during cycling. The experiments were performed at 550, 600, 650, 700 °C with the H_2O/EtOH ratio of 6:1 at atmospheric pressure. The minimum reaction temperature was determined according to the iron oxide reduction temperature >534°C see section (4.6). It was reported for H_2O/C_2H_5OH molar ratios between 3 to 6 the equilibrium amounts of H_2 were increased, no significant increase was noticed for H_2O/C_2H_5OH molar ratios higher or less than that range (Olivas et al., 2014). The latter observation was the reason for choosing H_2O/EtOH =6 ratio to be used in at of all the micro-reactor experimental tests. The effect of varying gas hourly space velocity was studied for GHSV of 2093 h^{-1}, 4186 h^{-1} and 8371 h^{-1}. The sorbent and catalyst stability test were performed for 10 cycles, which corresponded to 30 hours of reaction. The yield of the produced gases (CO_2, CH_4, C_2H_4, C_2H_6, C_3H_8, H_2) were

calculated by the mass balance of carbon, oxygen and hydrogen. It was assumed that the total molar flow of carbon entering the reactor from ethanol was equal to the carbon leaving the reactor; the outlet coke accumulation was neglected, as there was no evidence for this on the samples after reaction, see section (5.2.5).

The carbon balance equation 5.4 contains two unknowns, $n_{out,dry}$, $C_2H_5OH,_{out}$:

$$(y_{CH_4} + 2y_{C_2H_4} + 2y_{C_2H_6} + 3y_{C_3H_8} + y_{CO_2}) \times n_{out,dry} + 2 \times n_{C_2H_5OH,out} = 2 \times n_{C_2H_5OH,in} \quad (5.4)$$

where, in and out subscripts denote relevant mole entering or leaving the reactor.

y = mole fraction of species.

n =total molar flow rate / mol /min.

n_i = molar flow rate of species i/mol /min.

The hydrogen balance analysis was performed as shown in equation 5.5. Hydrogen entering the reaction from water and ethanol was equal to hydrogen leaving the reaction. Equation 5.7 contains three unknowns, $n_{out,dry}$, $nH_2O,_{out}$ and nC_2H_5OH.

$$(2y_{H_2} + 4y_{CH_4} + 6y_{C_2H_6} + 4y_{C_2H_4} + 8y_{C_3H_8}) \times n_{out,dry} + 2 \times n_{H_2O_{out}} + 6 \times n_{C_2H_5OH_{out}} = 6 \times n_{C_2H_5OH_{in}} + 2 \times n_{H_2O_{in}}$$

(5.5)

Ethanol and water conversion was defined as follows:

$$X_{EtOH} = \frac{nC_2H_5OH_{in} - nC_2H_5OH_{out}}{nC_2H_5OH_{in}} \times 100 \quad (5.6)$$

where,

$nC_2H_5OH_{in}$: ethanol molar flow rate entering the reactor/mol/min.

n $C_2H_5OH_{out}$: ethanol molar flow rate leaving the reactor/mol/min.

$$X_{H_2O} = \frac{nH_2O_{in} - nH_2O_{out}}{nH_2O_{in}} \times 100 \quad (5.7)$$

where,

nH_2O_{in}: water molar flow rate entering the reactor/mol/min.

nH_2O_{out}: water molar flow rate leaving the reactor/mol/min.

The molar flow rates of products from reaction were calculated by:

$$n_{i,out} = y_i \times n_{out,dry} \tag{5.8}$$

Product yield (Y_i) was defined as follows:

$$Y_i = \frac{n_{i,out}}{nC_2H_5OH_{in}} \tag{5.9}$$

The selectivity (S_i) of any product CO_2, CH_4, C_2H_4, C_2H_6, C_3H_8, H_2 was defined as follows

$$Si = 100 \times \frac{moles\ of\ Xi\ produced}{\Sigma\ moles\ Xi} \tag{5.10}$$

Iron oxide exists as different phases depending on the temperature and gas phase conditions. Table 5.1 shows the different phases of iron oxide. In the conventional steam- iron process, iron oxide is used to reduce steam to hydrogen. First iron oxide is reduced from hematite (Fe_2O_3), to magnetite (Fe_3O_4), to wustite (FeO), and to metallic iron (Fe)(Yamaguchi et al., 2011). Recently, different fuels such as gasified coal, gasified biomass, natural gas, petroleum products, industrial waste gas from blast furnaces or refineries have been used to reduce iron oxide using CO as the reducing gas, the product was reduced iron oxide and CO_2, see equations 5.11-5.14.

$$3\ Fe_2O_3 + CO \rightarrow 2\ Fe_3O_4 + CO_2 \tag{5.11}$$

$$Fe_3O_4 + CO \rightarrow 3\ FeO + CO_2 \tag{5.12}$$

$$FeO + CO \rightarrow Fe + CO_2 \tag{5.13}$$

Alternatively, Fe_3O_4 can be reduced to Fe as shown in equation (5.14):

$$Fe_3O_4 + 4\ CO \leftrightarrow 4\ CO_2 + 3\ Fe \tag{5.14}$$

Then, H_2 is produced by oxidizing FeO and Fe with steam in as shown in reactions equations (5.15) and (5.16).

$$Fe + H_2O \rightarrow FeO + H_2 \quad (5.15)$$

$$3\ FeO + H_2O \rightarrow Fe_3O_4 + H_2 \quad (5.16)$$

CO and H_2 from equation (5.17) and (5.18) can be subsequently oxidized as follows:

$$H_2 + FeO \rightarrow H_2O + Fe \quad (5.17)$$

$$CO + FeO \rightarrow CO_2 + Fe \quad (5.18)$$

Table 5.1. The oxidation states of iron oxide (Murugan, 2012).

Chemical name	Chemical formula	Oxidation state
Iron	Fe	0
Iron (II) oxide, wustite	FeO	+2
Iron (II,III) oxide, magnetite	Fe_3O_4	+2,+3
Iron (III) oxide, hematite	Fe_2O_3	+3

*Magnetite exists as a mixture of wustite and hematite.

5.2.1. Sorbent Activity Test

Steam reforming (SR), Water gas shift (WGS) and carbonation reactions are all active during the SESR CO_2 uptake pre-breakthrough phase. The calcined CaO capture CO_2 while ethanol steam reforming is favored by the CO_2 removal. steam has been reported to affect the carbonation reaction (Sultana and Chen, 2011). Several studies were conducted for the investigation of the effect of steam on the carbonation on CaO-based sorbent (Sun et al., 2008, Manovic and Anthony, 2010, Zeman, 2008). Dobner et al., 1977 reported that the carbonation rate of calcined dolomite was enhanced with the presence of steam (Dobner et al., 1977). On the contrary, Sun et al., 2008 claimed that there was no evidence of carbonation reaction enhancement in presence of steam (Sun et al., 2008). Han et al., 1994 observed that CO_2 uptake capacity of was slightly affected by the addition of steam to the CO_2/N_2 mixture (Han et al., 1994). In this context, a detailed kinetic study on CaO based acceptor is still needed to understand steam effects

on the carbonation reaction. TGA is widely used for the evaluation of CO_2 sorbent capacities. Many authors used TGA to study CaO-based sorbent performance (Balasubramanian et al., 1999, Han et al., 1994). However, some of TGAs have technical limitation that inhibit their usage for CO_2 sorbent evaluation in the presence of steam (Sultana and Chen, 2011).

Fixed bed reactor can be used in presence of steam at different conditions for CO_2 capture experiments and provide more accurate kinetic results (Chen et al., 1996). Reaction operating conditions and sorbent properties such as its mass and sorption capacity are responsible for the duration of the CO_2 uptake pre-breakthrough period. From TGA results of CO_2 uptake capacities of the prepared CaO-based sorbents, sample Ca6Mg2Ce1 exhibited high and stable capacity (>20 wt. %) over 45 cycles of successive carbonation/de-carbonation reaction, see section (4.3) and (4.6).

Accordingly, Ca6Mg2Ce1 was added to the iron oxide catalyst using co-precipitation method, see sections (3.1) and (4.8). The mixed Fe_2O_3/Ca6Mg2Ce1 sample was made up in 1:6 weight ratio respectively, 1 g of the mixed Fe_2O_3/Ca6Mg2Ce1 equivalent to 0.86 g of Ca6Mg2Ce1 was used for SEESR in a fixed bed reactor. Figure.5.3 shows the mass spectrometer graphs for the comparison between H_2 and CO_2 production profiles in mixed Fe_2O_3/Ca6Mg2Ce1 and in Fe_2O_3 alone.

Generally, it was observed that the CO_2 production profile did not correspond to hydrogen production in the Fe_2O_3/Ca6Mg2Ce1 mixture compared to Fe_2O_3 alone, which confirms the CO_2 absorption activity of the CaO. The CO_2 breakthrough started after 70 min from induction (i.e. 32 min) and 110 min of reaction time (i.e. 180 min). Alternatively, Figure 5.2 indicated that the de-carbonation period of 60 min in pure argon at 700 °C was enough to regenerate CaO and thus convert $CaCO_3$ to CaO. The latter observation was similar to results obtained from TGA.

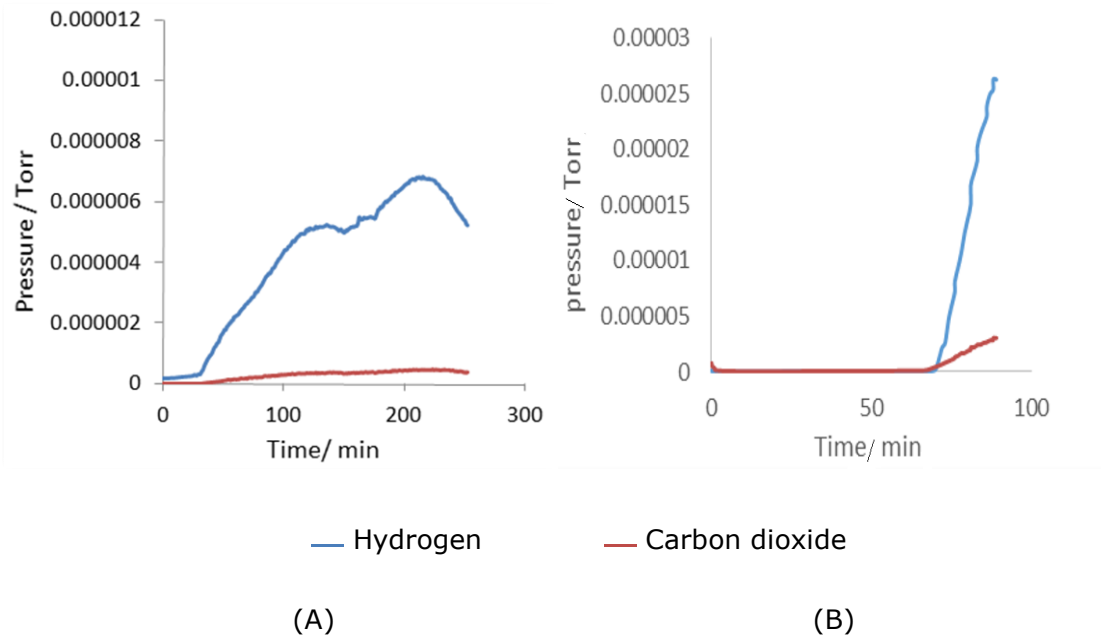

Figure 5.3. Mass spectrometer pressure versus time for hydrogen, carbon dioxide production profile at 700 °C, 101.325×10^3 Pa and H_2O/EtOH =6 in (A) Fe_2O_3/Ca6Mg2Ce1 (B) Fe_2O_3.

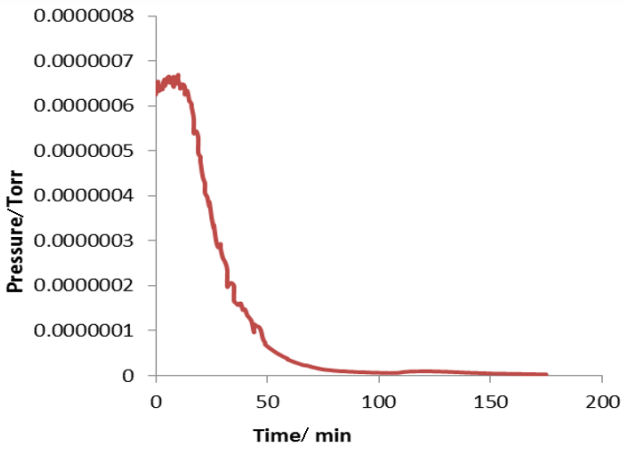

Figure 5.4. Mass spectrometer sorbent regeneration profile.

5.2.2. Effect of reaction temperature

Temperature is an important parameter in the SESR reaction; it influences not only the thermodynamic equilibrium of carbonation and WGS reaction but also the rate of the reforming reactions (Noor et al., 2014). The experimental investigations of temperature

effect were studied in the range of 550–700°C and results are represented in Figure 5.5. The minimum reaction temperature was determined according to the iron oxide reduction temperature >534°C, see Figure 4.6. As observed from Figure 5.6, the maximum hydrogen yield was achieved at 600 °C. Figure 5.7 shows that the selectivity towards hydrogen production was higher than 55 % at all the studied temperatures.

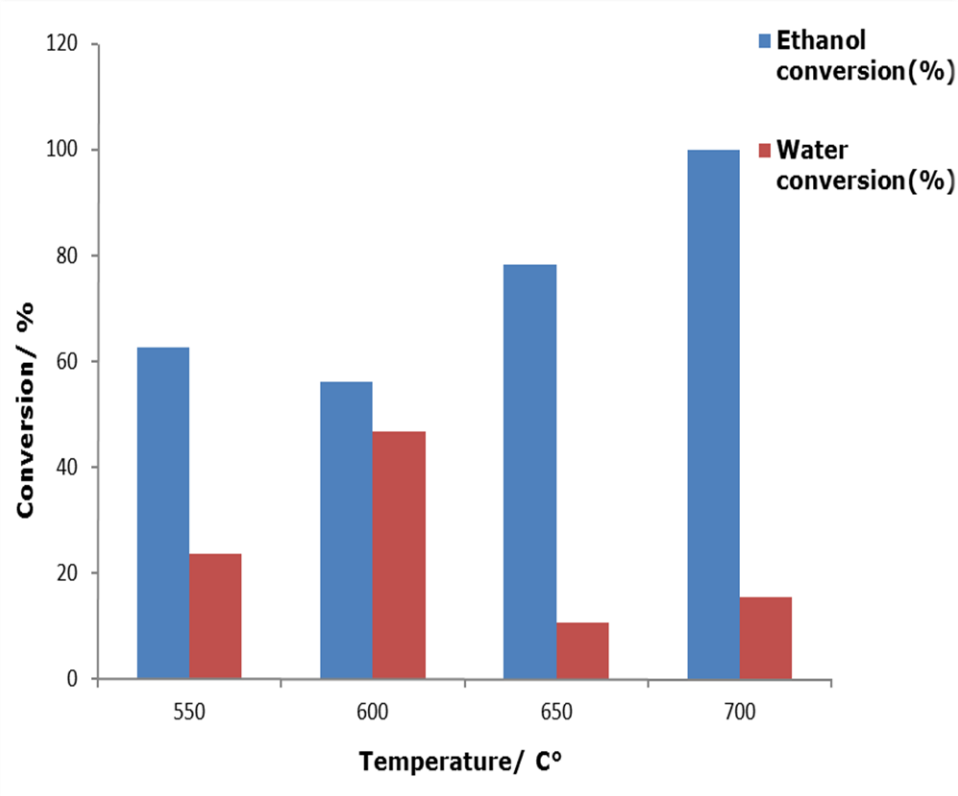

Figure 5.5. Ethanol/water conversion for ethanol reaction at 550, 600, 650, 700°C, 101.325×10^3 Pa and H_2O/EtOH =6 and GHSV (4186 h^{-1}).

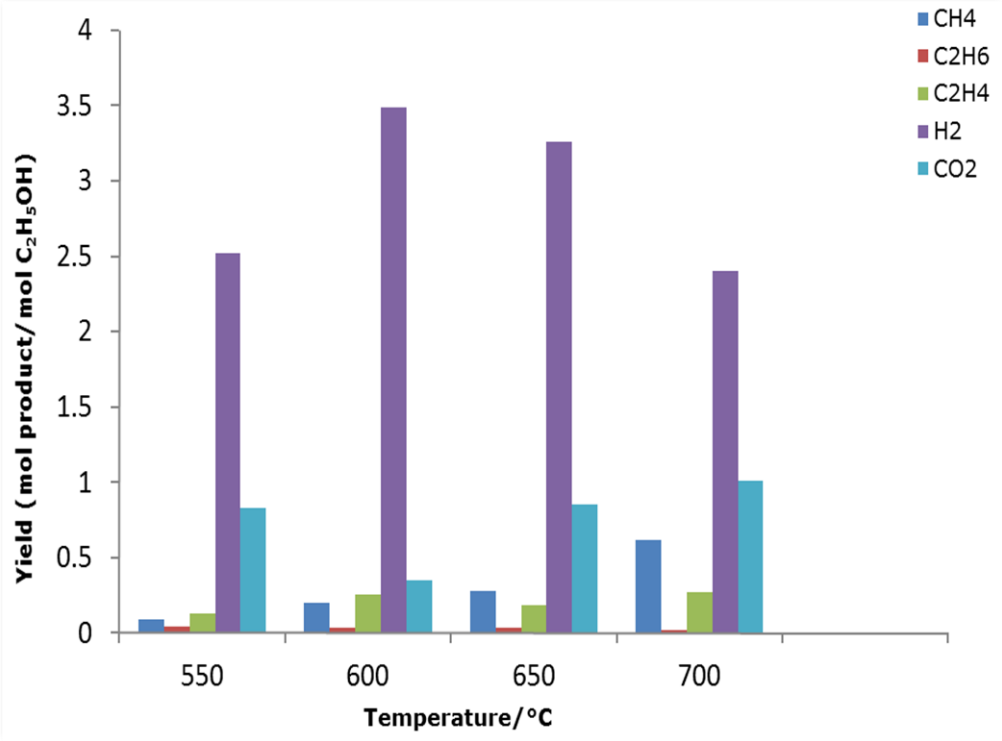

Figure 5.6. Products yields for ethanol/Fe_2O_3/Ca6Mg2Ce1 reaction at 550, 600, 650, 700°C, 101.325×10^3 Pa and H_2O/EtOH =6 and GHSV (4186 h^{-1}).

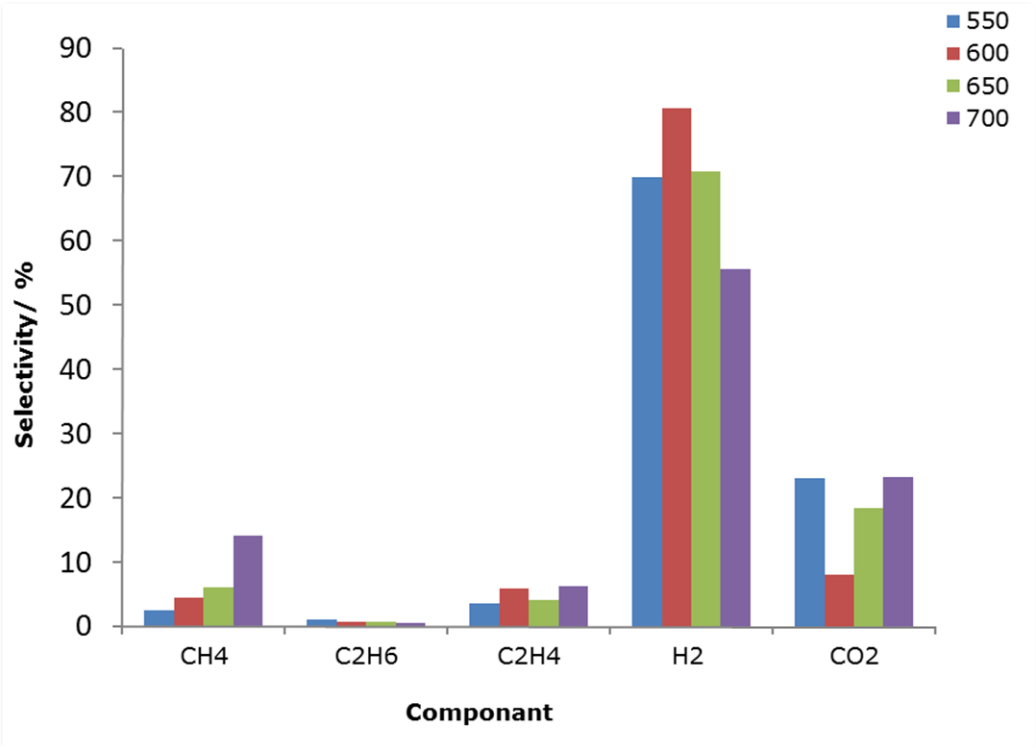

Figure 5.7. Products selectivity for ethanol/Fe_2O_3/Ca6Mg2Ce1 reaction at 550, 600, 650, 700°C, 101.325×10^3 Pa and H_2O/EtOH =6 and GHSV (4186 h^{-1}).

The low water conversion at higher temperature range (600-700 °C), see Figure 5.5, suggested that the ethanol decomposition reaction was the dominant reaction. In spite of that, there was no evidence of C or CO in the produced gas. Absence of CO in the produced gas indicated that CO had been converted to CO_2 via WGS reaction. Alternatively, CO could have been a reducer gas for Fe_2O_3 to Fe_3O_4 in the first stage, and from Fe_3O_4 to Fe in the second stage, as shown in equation 5.11-5.14. It is important to note that there are also reactions between the gaseous reactant and product, which can take place within the reactor, that can contribute in the conversion of CO into CO_2, such as water-gas shift reaction (WGS) and Boudouard reaction, see equations 2.3 and 5.3 respectively.

Ethanol conversion gradually increased with increasing temperature. The product yield of experimental results for the studied temperature range of 550-700°C, are shown in Figure 5.6. It is noticed that the H_2 concentration increased until 600°C and then dropped with increasing temperature to 700°C. There was a deviation of the experimental H_2 content, from the corresponding equilibrium values, as the hydrogen yield was approximately half the amount of the calculated predication (2.5mol H_2/mol EtOH). This decrease in H_2 yield may have been due to higher CH_4 content in the gas product. CH_4 increases could have been the result of the favorable thermodynamics of the methanation reaction. CO_2 was relatively increased with the temperature increase; this increase may be referring to the reverse of WGS reaction at higher temperature.

Traces of C_2H_4 and C_2H_6 (<0.2) were observed in the gas products with no evidence of C or CO. C_2H_4 may have resulted from ethanol dehydration, see Table 2.4. In general, the experimental gas compositions from SEESR reaction were found to be rather inconsistent with the predicted equilibrium values. This can possible ascribed to iron oxide activity and selectivity towards the methanation reaction. However, the experimental results showed a high dependence on temperature.

It can be concluded that hydrogen production by SEESR was kinetically limited by the WGS reaction and enhanced methanation. These observations can be explained by the fact that endothermic SR reactions equation 2.1 and reverse of WGS equation 2.3 were

favourable at elevated temperature; while exothermic WGS was favoured at lower temperature. In spite of that, contribution of endothermic SR reactions to hydrogen yield were dominating over exothermic WGS, leading to growing trends of hydrogen yield with increasing temperature. The maximum H_2 yield and minimum CO_2 concentration was achieved at 600°C. Higher temperatures were unfavorable for the exothermic carbonation kinetics which resulted in higher CO_2 concentration and lower H_2 purity at 700°C. The highest H_2 purity (80%) was achieved at 600°C.

It may be concluded that the temperature effect on equilibria was complex, as the ethanol reforming was endothermic therefore, the equilibrium constant increases with temperature. On the other hand, the water–gas shift reaction was exothermic, thus its equilibrium constant dropped at with elevated temperature. Therefore, at higher temperatures, H_2 was converted back to H_2O while CO_2 was converted back to CO, see equation 2.3. Hence, it was necessary to optimise the reaction temperature in order to maximise H_2 yield. Accordingly, high CO_2 content increased the backward reaction rate of WGS and a higher temperature was able to compensate or promote the forward SR reaction rate.

5.2.3. Effect of gas hourly space velocity (GHSV)

The influence of varying gas hourly space velocity (GHSV) of the premixed H_2O/EtOH feed fuel on the produced gas yields was studied under given ethanol steam reaction conditions of (H_2O/EtOH =6, 700°C, 101.325 $\times$ 10 ^{3} Pa). The variation of GHSV was performed by adjusting the amount of the feed flow rate. Figures 5.8, 5.9 show the dependence of reaction products yield (%) and selectivity (%) during the SESR of ethanol at 700°C and atmospheric pressure on the GHSV.

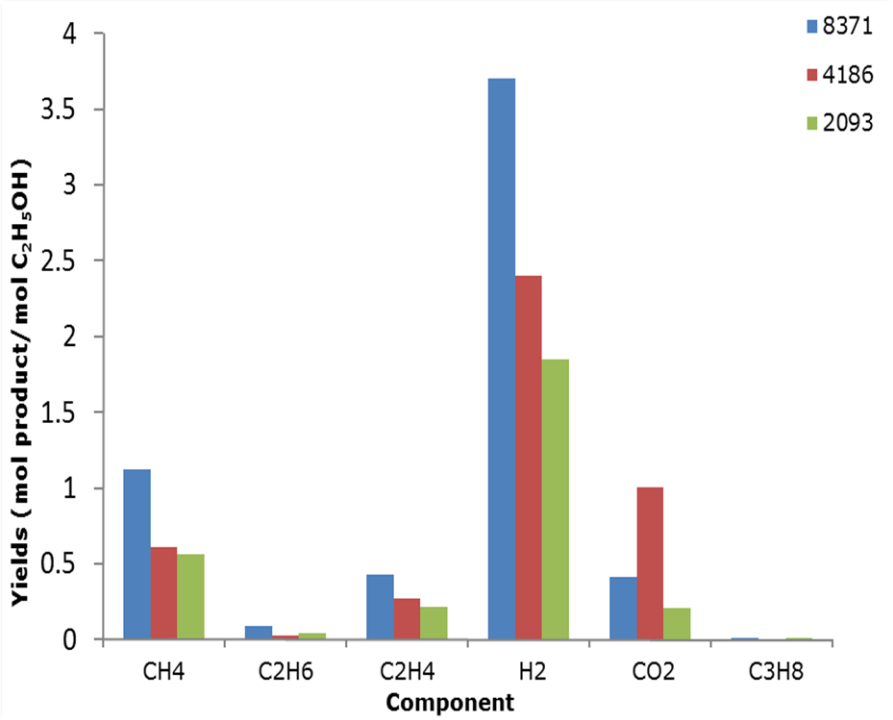

Figure 5.8. Products yields for ethanol/Fe_2O_3/Ca6Mg2Ce1 reaction at 2093 h^{-1}, 4186 h^{-1} and 8371 h^{-1}, 700 °C, 101.325×10^3 Pa and H_2O/EtOH =6.

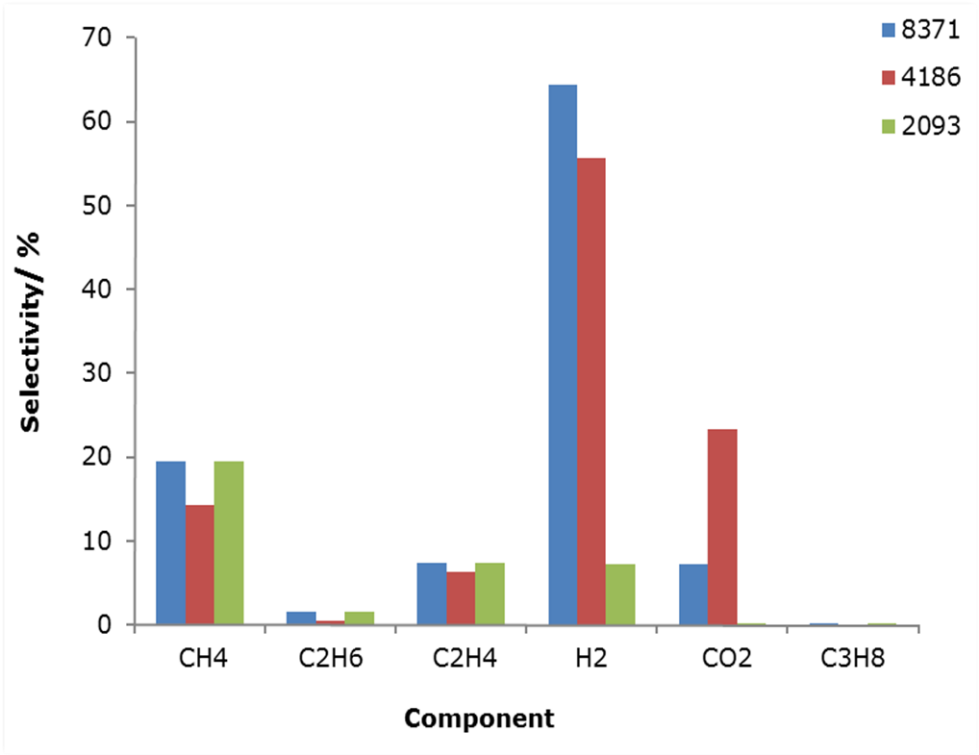

Figure 5.9. Products selectivity for ethanol/Fe_2O_3/Ca6Mg2Ce1 reaction at 2093 h^{-1}, 4186 h^{-1} and 8371 h^{-1}, 700°C, 101.325×10^3 Pa and H_2O/EtOH =6.

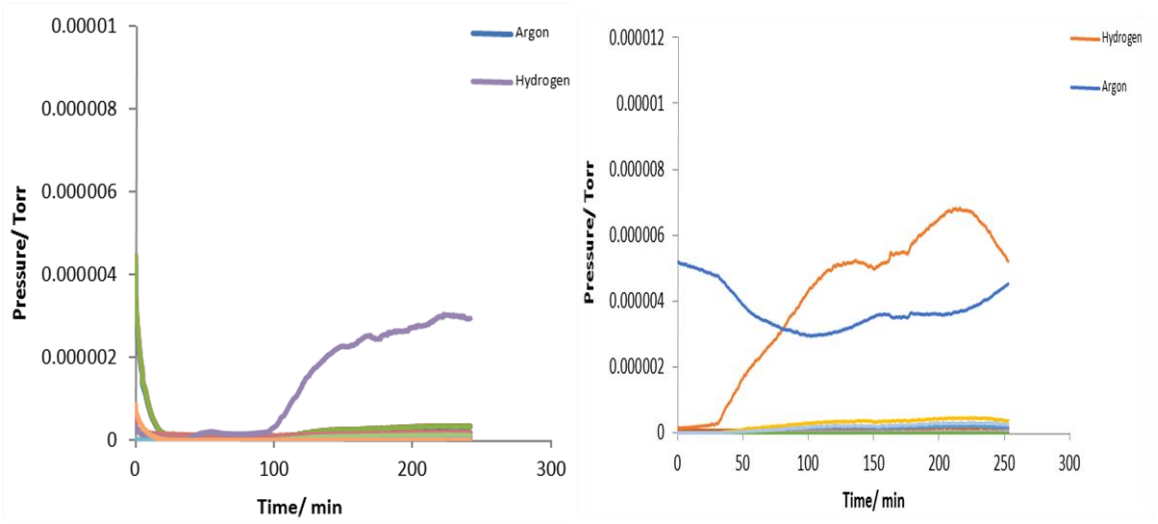

(A) (B)

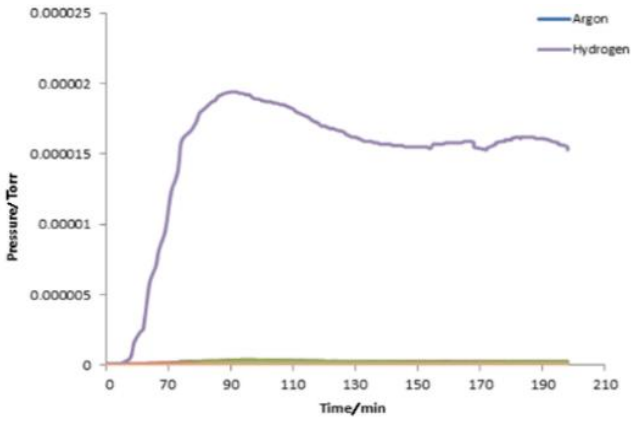

(C)

Figure 5.10. Mass spectrometer profile versus induction time for ethanol/Fe_2O_3/Ca6Mg2Ce1 reaction for GHSV of 2093 h^{-1} (A), 4186 h^{-1} (B) and 8371 h^{-1} (C) at 700 °C, 101.325×10^3 Pa and H_2O/EtOH =6.

As shown in Figure 5.8, with the feed flow rate increasing from of 2093 h^{-1} up to 8371 h^{-1}, the H_2 yield increased from 1.9 to 3.7 mole H_2/mole EtOH and selectivity increased from 7% to 64%. The CH_4 selectivity remained relatively constant (14-19%). The C_2H_2 and C_2H_6 were remained stable for the different studied GHSVs. The results showed a gradual decrease of H_2 yields with decreasing GHSVs.

The later decrease in H_2 yield may suggest a much lower reaction rate of ethanol reforming and water gas shift reactions at lower GHSVs. However, it was claimed that with fewer GHSVs the contact time between the catalyst bed and the reactants became longer (Wei et al., 2000). Therefore, the thermodynamic equilibrium conversions of the reactants were completely achieved. On the other hand, increasing GHSV value will result in a limitation of active centres in the catalyst for the growing number of the reactants. Eventually, these two factors mean that higher GHSVs led to lower H_2 yields and less reactants conversions (Wei et al., 2000, Xu et al., 2012).

Nevertheless, SESR using iron oxide is extremely complicated and there is still need for further investigation. It was also noticed that there was no need for the iron oxide reduction step, which was similar to chemical looping reaction and therefore the iron oxide catalyst was reduced and oxidised by the produced gas in the looping cycle and this may explain the higher reactivity of the iron oxide catalyst at higher GHSV. The mass spectrometer profiles for the reactions at 2093-4186-8371 h^{-1} displayed in Figure 5.10 confirm that although the reactions at the different GHSVs have the same induction periods, the reaction kinetics is slow at lower GHSV.

5.2.4. Carbon formation analysis for used iron oxide catalysts

Carbon deposition on the catalyst surface is considered one of the main causes of catalyst deactivation as discussed in chapter 2 section (2.2) (Bengaard et al., 2002, Rostrup-Nielsen, 1984, Sidjabat and Trimm, 2000). It could cause physical damage of the catalyst pores, such as catalyst pore-mouth plugging as well as obstruction of the active sites on the catalyst loss of surface area of (Twigg and Burgess, 2003, Richardson, 2013). The hydrocarbon decomposition reaction is the main source of carbon deposition (Rostrup-Nielsen et al., 2002). The TGA analysis described in chapter 3 section (3.9) were used to investigate the amount of carbon deposition for the used iron oxide/ sorbent at 550-700°C and iron oxide alone at 700 °C. Both air and N_2 were used separately in the TGA as the purging gas to show the comparison reduction for the used samples after ethanol steam reforming Figure 5.11, 5.12. Furthermore, XRD tests were

conducted to investigate the changes of the samples phases after 3h of ethanol steam reforming reaction, see Figures 5.13 and 5.14.

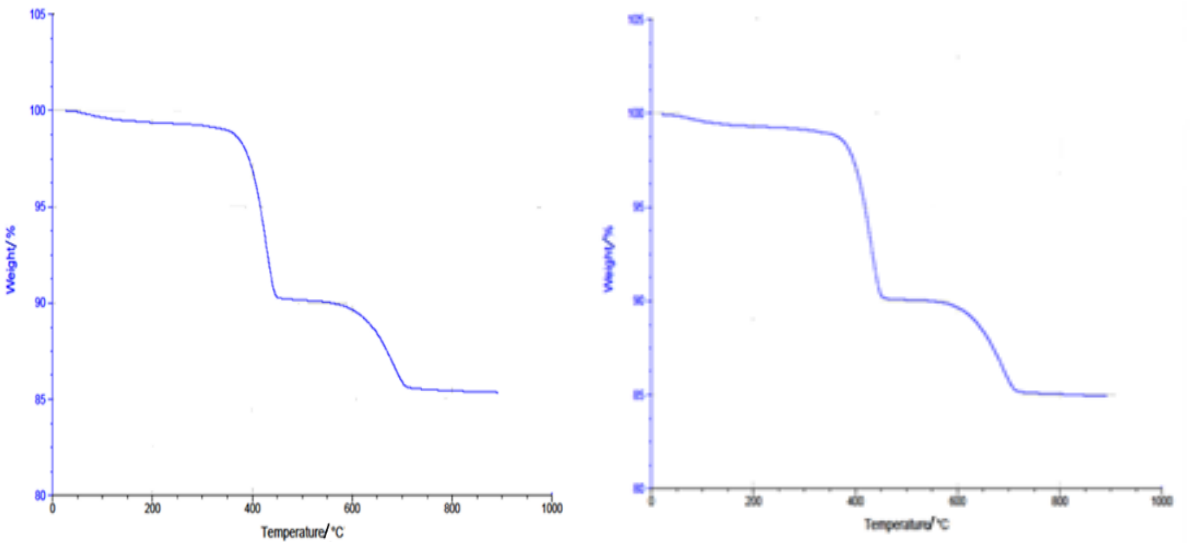

(A) (B)

Figure 5.11. TGA curve for the used Fe_2O_3/Ca6Mg2Ce1 reacted at 700°C, 101.325×10^3 Pa and S/C =6, under air as purging gas with ramping rate of 5°C/min to 900 °C (A) and N_2 as purging gas with ramping rate of 5°C/min to 900 °C (B)

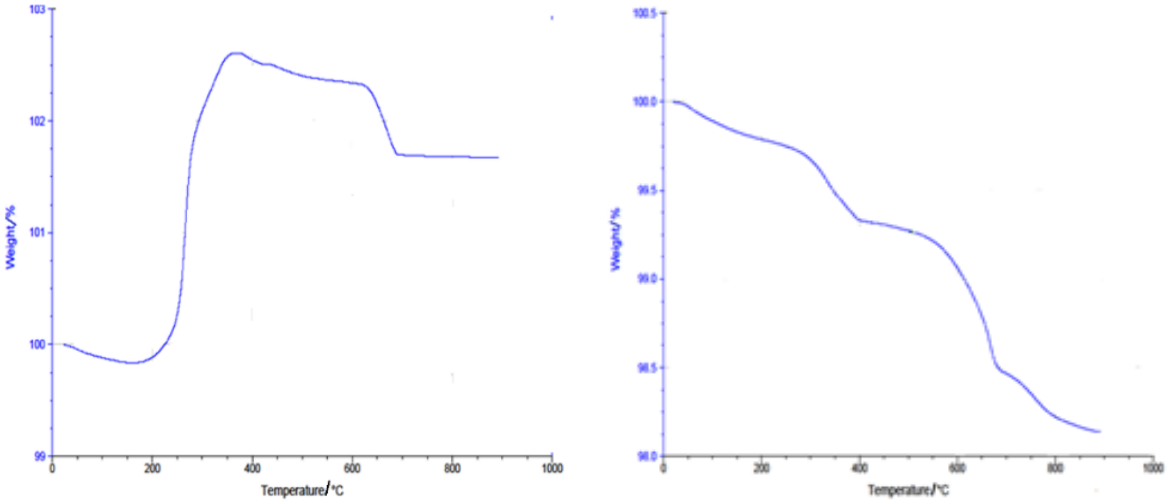

(A) (B)

Figure 5.12. TGA curve for the used Fe_2O_3 reacted at 700°C, 101.325×10^3 Pa and S/C =6 under air as purging gas with ramping rate of 5°C/min to 900 °C (A) and N_2 as purging gas with ramping rate of 5°C/min to 900 °C (B).

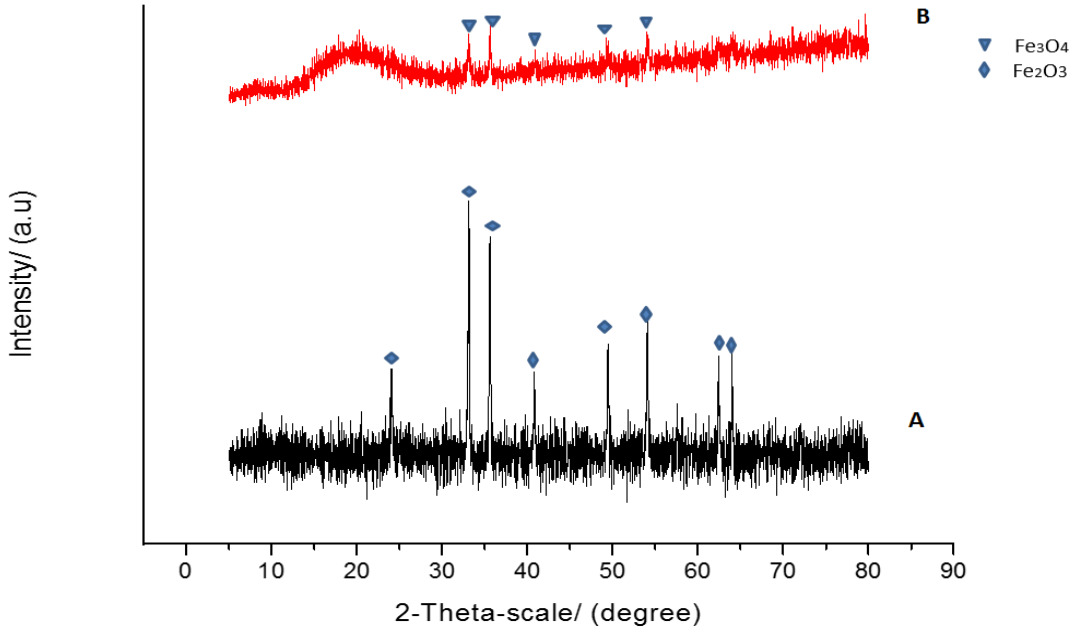

Figure 5.13. XRD pattern for used Fe_2O_3 reacted at 700°C, 101.325×10^3 Pa and S/C =6 before A and after B carbon deposition test in TGA under air as purging gas with ramping rate of 5°C/min to 900 °C.

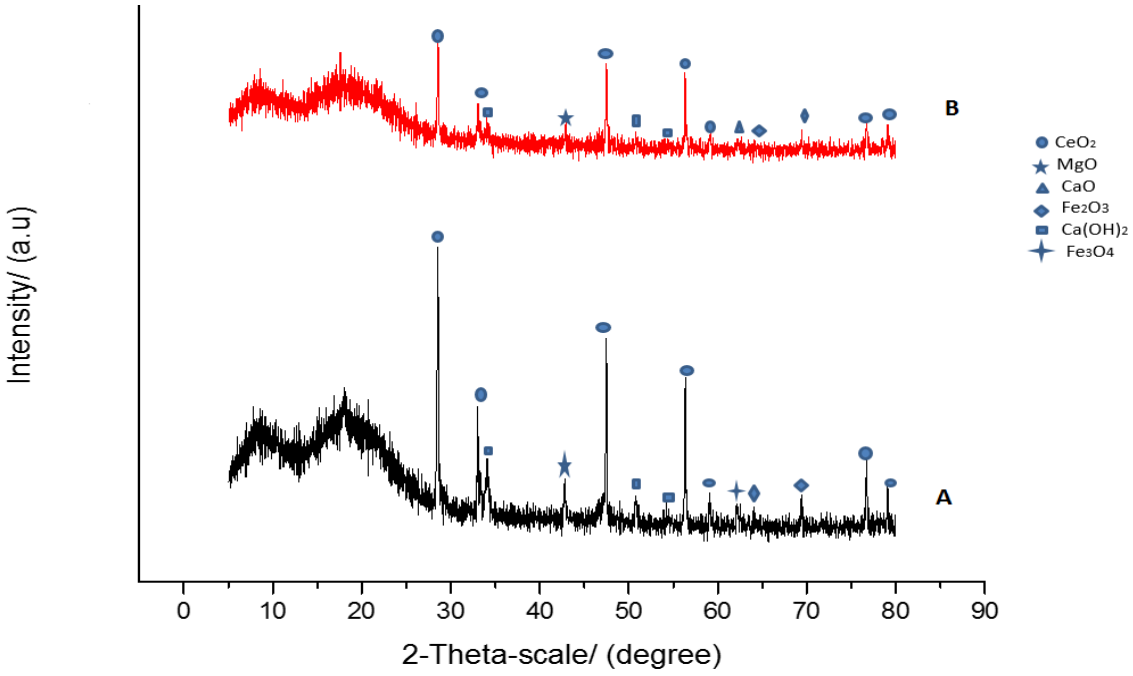

Figure 5.14. XRD pattern for used Fe_2O_3 / Ca6Mg2Ce1 reacted at 700°C, 101.325×10^3 Pa and S/C =6 before A and after B carbon deposition test in TGA under air as purging gas with ramping rate of 5°C/min to 900 °C.

Figure 5.11 shows that the Fe_2O_3 /Ca6Mg2Ce1 sample exhibited similar reduction curves in air and N_2 atmospheres. By examining the XRD patterns for Fe_2O_3/Ca6Mg2Ce1 before the TGA test, no evidence of a carbon phase was detected. Fe_3O_4 phase appeared in the sample before the TGA test whereas Fe_2O_3 appeared after it. Therefore, the weight loss from 25 °C up to 400°C is ascribed to moisture and other volatiles loss, while the weight loss from 400°C up to 600°C to the thermal decomposition of $Ca(OH)_2$ as $Ca(OH)_2$ decomposed to CaO at 450-500°C (Criado et al., 2014). Similar results were obtained in the determination of sorbent calcination temperature which was discussed in section (4.2). XRD patterns of the used Fe_2O_3 / Ca6Mg2Ce1 sample before TGA test showed the presence of $Ca(OH)_2$ due to moisture contamination.

On the other hand, the TGA profile of Fe_2O_3 sample in air showed different behaviour from in N_2 atmosphere, see Figure 5.12. For Fe_2O_3 in air, first there was weight reduction from 25 °C up to 159 °C due to moisture loss, the curve shows weight gain from 200°C up to 350°C due to Fe_3O_4 oxidation to Fe_2O_3 then less than 1% weight loss was observed in temperature range from 350°C up to 650°C due temperature effects as some of the oxidised Fe_2O_3 was again reduced to Fe_3O_4 as previously noticed in the catalyst reducibility test. After 650°C the sample weight was stabilized.

As shown in the XRD, Fe_2O_3 appeared in sample Fe_2O_3/Ca6Mg2Ce1 after TGA this indicated the reversible effect of oxidation and temperature effects which resulted in an oxidised phase of Fe_2O_3. Generally, it can be concluded from the TGA and XRD results for Fe_2O_3/Ca6Mg2Ce1 and Fe_2O_3, that there was no evidence of carbon deposition on both samples used in the ethanol reformation reaction. The Boudouard reaction, see equation 5.3, is known as carbon deposition reaction and it is thermodynamically favored at a low temperature and high pCO/pCO_2. CH_2CH_2 was detected in the GC results over all temperatures. CH_2CH_2 has been considered as a main precursor for the deposition of coke on the catalyst surface (Han et al., 2013). The extent of iron oxide reduction may determine the state of carbon deposited on the surface of the particles. When the iron oxide was reduced to FeO, very pure H_2 was produced (Cho et al., 2014). Minimisation of

coke formation could be achieved through the optimisation of the steam-to-ethanol ratio and the operating temperature (Christensen et al., 2006, Rossetti et al., 2014).

It was reported that coke gasification by steam at high temperatures resulted in improvement of catalyst performance (Arslan et al., 2014). Therefore, activity tests were also performed at 700°C to facilitate carbon gasification. Furthermore, carbon gasification could also contribute to the increase in H_2 yields. Carbon gasification by steam produces CO_2 and CO see equation 5.19, 5.20.

$$C + 2H_2O \rightarrow CO_2 + 2H_2 \quad (5.19)$$

$$2C + 2H_2O \rightarrow 2CO + 2H_2 \quad (5.20)$$

Arslan et al ,2014 reported that carbon formation was favored at H_2O/EtOH molar ratios less than 6 (Arslan et al., 2014). These results are consistent with the thermodynamic equilibrium analysis showed in section (5.2), where the coke was not likely to form at S/E molar ratios of 6 for the ethanol steam reforming reaction. Addition of cerium oxide as modification facilitates the oxygen mobility in oxidation and reduction reaction (Fornasiero et al., 1996, Gorte and Zhao, 2005, Cheng et al., 1996). Its oxygen-storage/release capacity (OSC) enables the immediate gasification of deposited carbon and therefore promotes the catalyst stability (Song and Ozkan, 2009, Wang et al., 2004).

Recently, CeO_2 has extensively been used as a catalyst support for ethanol reforming mainly because it favors ethanol dehydrogenation to CH_3CHO rather than dehydration to CH_2CH_2, which polymerises and form coke (Idriss, 2004, Bion et al., 2012). Some authors reported that ceria-supported noble metal is active for the water gas shift reaction (Kugai et al., 2005, Deluga et al., 2004, Han et al., 2013). XRD patterns of Fe_2O_3 alone sample and Fe_2O_3 / Ca6Mg2Ce1 sample after the first cycle of ethanol steam reforming at 700 °C ,1 atm and 4186 h^{-1} shows that there was no evidence of carbon existence.

It also can be seen from the TGA graphs that for the Fe_2O_3 alone sample and Fe_2O_3/Ca6Mg2Ce1 sample had similar reduction profiles either by using air or N_2 as the carrier gas. This similarity may confirm that there is no contribution of carbon oxidation and accordingly there is no significant carbon existence in both samples after H_2O/EtOH reaction. The reduction of the weight at temperatures between 350-600 °C is ascribed to dehydration of $Ca(OH)_2$, as previously discussed in the sorbent calcination temperature determination test which is described in section (4.1). The appearance of $Ca(OH)_2$ in the samples before the TGA experiment confirmed this observation.

5.4. Cycling behaviour test (Time-on-stream behaviour)

The deactivation of some catalysts is considered the main prevention for their practical application. Coke deposition and sintering of the metallic active phase are the main causes of catalyst deactivation. The long stability of the iron oxide catalyst was examined under the specific reaction conditions of H_2O/EtOH =6, 700 °C, LHSV= $4h^{-1}$, 1 atm. Iron oxide catalyst exhibited reasonable catalytic reactivity and stability throughout the 30 hours of the long stability test counted as 10 cycles of ethanol steam reforming reaction. Each cycle consisted of four hours, three hours of ethanol reformation and CaO carbonation and one hour of de-carbonation and regeneration of CaO.

The product gases composition as a function of time on stream of the SESR reaction process on Fe/Ca6Mg2Ce1 at 700°C is shown in Table 5.2, 5.3. The H_2 yield in the gas product remained relatively constant over the period of 10 cycles (2.2-2.7mol H_2/mol EtOH) corresponding to 53-57% concentration. The stability of H_2 yield and selectivity indicated that there was no significant deactivation of the iron oxide catalyst. It was of interest that the induction time for H_2O/EtOH reaction was gradually increased as the number of cycles proceeded from 32 min at first cycle to 66 min after 5 cycles and finally to 103 min after 10 cycle of reaction. The reason for this decay in induction time is not clear and may need more investigation in the future work.

Table 5.2. Products yields vs. induction time for ethanol/Fe2O3/Ca6Mg2Ce1 reaction for cycle 1,5,10 at 700°C, 101.325 × 10 ^{3} Pa, GHSV= 4186 $h^{-1}$and C/W=6.

Cycle	Time on stream (h)	Induction Time (min)	Yields					
			H_2	CH_4	C_2H_6	C_2H_4	C_3H_8	CO_2
Cycle 1	3	32	2.56	0.65	0.025	0.29	0	1.07
Cycle 5	15	66	2.73	1.31	0.077	0.64	0.002	0
Cycle10	30	103	2.27	1.11	0.088	0.55	0.002	0.22

Table 5.3. Products selectivity vs. induction time for ethanol/Fe2O3/Ca6Mg2Ce1 reaction for cycle 1,5,10 at 700°C, 101.325 × 10^{3} Pa, GHSV= 4186 $h^{-1}$and C/W=6.

Cycle	Time on stream (h)	Induction Time	Selectivity					
			H_2	CH_4	C_2H_6	C_2H_4	C_3H_8	CO_2
Cycle 1	3	32	55.66	14.19	0.54	6.29	0	23.32
Cycle 5	15	66	57.40	27.52	1.63	13.40	0.051	0
Cycle10	30	103	53.48	26.17	2.08	12.98	0.048	5.24

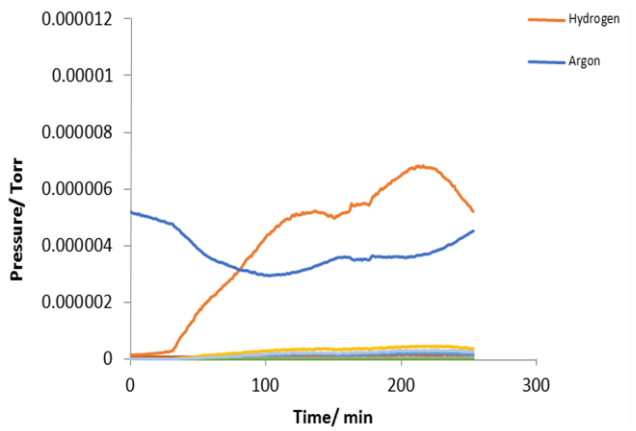

(A)

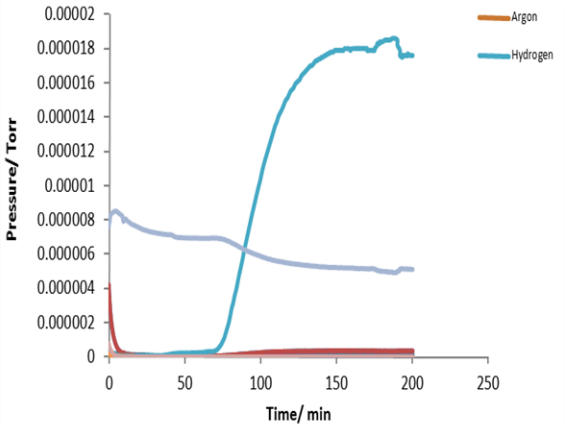

(B)

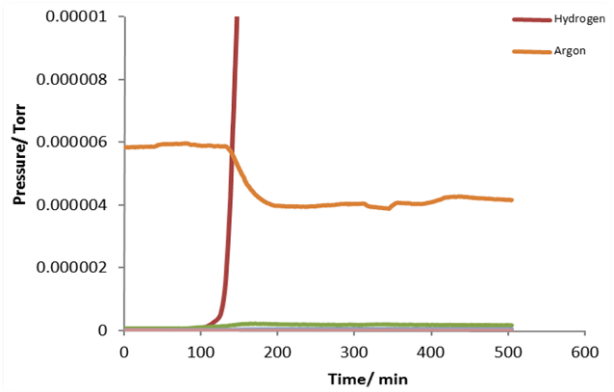

(C)

Figure 5.15. Ethanol/Fe_2O_3/Ca6Mg2Ce1 reaction mass spectrometer profile versus induction time for GHSV of 2093 h^{-1} (A), 4186 h^{-1} (B) and 8371 h^{-1} (C) at 700°C, 101.325×10 ^{3} Pa and H_2O/EtOH =6.

5.5. Chapter summary

Iron oxide catalyst mixed with Ca6Mg2Ce1, CO_2 sorbent, was prepared using the co-precipitation method. The mixed oxides were used for ethanol reforming reaction at steam carbon ratio H_2O/EtOH =6 and atmospheric pressure. Activity tests were conducted for the mixed oxide Fe_2O_3/Ca6Mg2Ce1 and for Fe_2O_3 alone. The mass spectrometer graphs for the comparison between H_2 and CO_2 production profiles in mixed Fe_2O_3/Ca6Mg2Ce1 and in Fe_2O_3 alone confirmed the CaO activity for CO_2 capture up to 70 min after induction time i.e. 32 min, and 110 min after SESR reaction time i.e.180 min.

This study also investigated the effects of reaction temperature (550-700°C), effects of gas hourly space velocity (2093-4186-8371 h^{-1}) and long-term stability test on the products distribution. The catalyst achieved a maximum of ethanol conversion of 100% at 700°C. The maximum hydrogen yield achieved was 3.5 mol H_2/mol EtOH at 600°C. GC results revealed that there was no evidence of CO and C, over all the studied temperature range. The reaction was also performed at different gas hourly space velocities of 2093, 4186 and 8371 h^{-1}.

The results showed an enhancement in reaction reactivity by increasing the GHSVs. Although, there was gradual delay in induction period after EtOH /steam injection and before reaction occurrence upon cycling, the mixed catalyst/sorbent had a high stability for hydrogen production within 10 cycles equivalent to 30 hours on stream, the reason for that is not clear and need more investigation in the future work.

CHAPTER SIX

General conclusions and suggestion for future work

Novel synthetic CaO-based sorbents were developed to be applied for the CO_2 capture in SESR process. Based on the experimental work carried out in this research the following conclusions were drawn. For the preparation of the CaO-based sorbents, the adapted co-precipitation method from (Park and Yi, 2012) described in section (3.1) was modified by adding a drying step to 350°C, under continuous slight stirring inside fume cupboard and the calcination of the samples at 650 °C afterwards successfully converted the nitrate precursors into oxide phases. MgO and CeO_2 were maintained their inert nature as they did not take part in the carbonation reactions and did not change the crystalline structure of CaO. It has been found that the CO_2 uptake capacity and CaO utilization of the prepared samples depend on the MgO , CeO_2, CaO ratio, thus controlling this ratio can results in improved the CaO utilisation and the CO_2 uptake capacity. It was found that samples at CaO, MgO and CeO_2 molar ratio of 6:2:1, 4:2:1 had CO_2 uptake capacities of 29 wt. % and 25 wt % respectively were in the accepted range to be applied in SESR processes for CO_2 capture i.e. 20-40 wt. % (Park and Yi, 2012a, Abanades et al., 2004, Yi and Harrison, 2005).

In order to understand better, the CaO carbonation reaction mechanism, modelling of the CO_2 uptake kinetics was investigated. It was reported that the carbonation reaction undergoes two main mechanism stages corresponding to the CO_2 interaction with the sorbent surface in the first stage and CO_2 diffusion through the product layer of $CaCO_3$ in order to reach the CaO core in the second stage, which suggests the modelling of CO_2 uptake kinetics by two different models. However, in this study, the carbonation reaction kinetics for samples at CaO, MgO and CeO_2 molar ratio of 6:2:1, 4:2:1 and 1:2:1 were modelled by three different models. The JMA (Johnson-Mehl-Avrami) model fitted best

the first and second stages, except for sample at CaO, MgO and CeO_2 molar ratio of 4:2:1 where surface chemisorption (SC) fits the initial stage and JMA fitted the second stage. While the contracting volume model (CV2/3, with a growth velocity decreasing with time fitted the final stages. The characterisation tests of the prepared samples confirmed that there was no clear correlation found between best CO_2 uptake and surface area. It is also concluded that the presence of MgO and CeO_2 as a partition wall provided a well-dispersed skeleton that prevented CaO sorbent sintering and provided a porous surface structure with some correlation with the pore structure. The sorbents' behaviour during the multiple carbonation/de-carbonation cycles revealed that all the prepared sorbents exhibited an increase in the CO_2 uptake capacities after the first cycle in different rate. The CO_2 released in the de-carbonation reaction changed the surface particle sizes from $CaCO_3$ back to CaO and resulted in formation of micro-cracks on the surface, which facilitated CO_2 mass transport during the next carbonation steps.

The sample of CaO, MgO and CeO_2 molar ratio of 6:2:1 showed relatively good stability over 45 cycles of successive carbonation/de-carbonation reactions and maintained over 75% of the capacity of the fresh sample. However, the compromise between the higher CO_2 uptake for a few cycles and stability of CO_2 uptake should be considered. The characterisation of the samples after multiple cycles of carbonation/de-carbonation showed that considerable changes in the sorbent microstructure, such as decrease of the CaO crystallite size after the first cycle, decrease in porosity and appearance of micro-cracks in the sorbent surface after 45 cycles. The improved stability of the sample of CaO, MgO and CeO_2 molar ratio (6:2:1) over 45 cycles of successive carbonation/de-carbonation reactions suggests its potential for the enhancement of ethanol steam reforming.

Carbonation tests in the TGA and characterisation tests of the sorbent /catalyst mixture revealed that the sorbent maintained its chemical and physical properties after being mixed with iron oxide as catalyst by the co-precipitation method described in section (3.1). Generally, and based on the above conclusions, it may be concluded that sorbent

porous texture is the key parameter for the gained stability over multiple carbonation/de-carbonation cycles. On the other hand, the activity test of the iron oxide/CaO-based sorbent mixture was investigated in a fixed bed reactor for the SESR atmospheric pressure and temperature of 550-600-660-700°C and gas hourly space velocity (GHSV) of 2093-4186-8371 h^{-1}. The long term cycling reactivity of catalyst /sorbent mixture was evaluated over 10 cycles equivalent to 30 hours of SESR reaction time.

The following conclusions were reached from the SEESR tests. The experimental results of SEESR showed that the CO_2 breakthrough curve level off after 70 min of induction time (i.e. 32 min) and 110 min of reaction time which was used to calculate of the required sorbent amount for the SEESR reaction based on this results for the future work. Although, the ethanol conversion of 100% was achieved at 700°C, which confirmed iron oxide catalytic activity, the maximum H_2 yield of 3.5 mol H_2/mol EtOH was obtained at 600°C. An enhancement in reaction reactivity by increasing the GHSV was observed. The mixed catalyst/sorbent had a high stability for hydrogen production within 10 cycles and 30 hours on stream. However, there was a gradual delay in induction period after EtOH /steam injection and before reaction occurrence appeared upon cycling, the reason for that is not clear and require more investigation in the future work.

It is worth mentioning that the GC results showed no evidence of CO in the produced gas across all the studied temperatures although it was favoured thermodynamically, this may be due to the iron oxide activity on WGS reaction to convert CO into the easy separable CO_2 and this confirmed the suitability of this research as an alternative route for hydrogen production suitable for PEM fuel cells. TGA and XRD tests confirmed that no carbon deposition had occurred.

In summary, based on the above conclusions, this research proved the suitability of employing iron oxide as reforming catalyst and provide promising route to produce hydrogen CO free suitable for PEM fuel cells through a novel and flexible SESR. However,

a complete development of this novel process to be reliable and economically viable is now essential. Therefore, better understanding of all the aspect of these reactions is recommended from the perspective of future work, including the following aspects:

- Further study on the CaO based-sorbent and sorbent/catalyst mixture formulation in more different molar percentages.
- The activity of the CaO-based sorbent for CO_2 capture during SESR should be improved to provide better CO_2 management.
- Long term study of SESR cyclic operation and process optimization with respect of the life time of both CaO-based sorbent and the iron oxide catalyst.
- In-situ characterization of the sorbent/catalyst mixture.
- The delay of the induction period in SESR upon cycling needs further investigation to identify the reason behind this delay in order to understand and control this phenomenon.
- An economical assessment of all the operating parameters is necessary in order to evaluate the feasibility of the present study.

References

ABANADES, J. C. & ALVAREZ, D. 2003. Conversion limits in the reaction of CO_2 with lime. Energy & Fuels, 17**,** 308-315.

ABANADES, J. C., ANTHONY, E. J., LU, D. Y., SALVADOR, C. & ALVAREZ, D. 2004. Capture of CO_2 from combustion gases in a fluidized bed of CaO. AIChE Journal, 50**,** 1614-1622.

AHNER, C. & HÄRING, H.-W. 2008. Industrial gases processing, Wiley-VCH.

ALVAREZ, D. & ABANADES, J. C. 2005. Pore-size and shape effects on the recarbonation performance of calcium oxide submitted to repeated calcination/recarbonation cycles. Energy & fuels, 19**,** 270-278.

ANTHONY, E. 2011. Ca looping technology: current status, developments and future directions. Greenhouse Gases: Science and Technology, 1**,** 36-47.

ARGYLE, M. D. & BARTHOLOMEW, C. H. 2015. Heterogeneous Catalyst Deactivation and Regeneration: A Review. Catalysts, 5**,** 145-269.

ARMOR, J. N. 1999. The multiple roles for catalysis in the production of H_2. Applied Catalysis A: General, 176**,** 159-176.

ARSLAN, A., GUNDUZ, S. & DOGU, T. 2014. Steam reforming of ethanol with zirconia incorporated mesoporous silicate supported catalysts. International Journal of Hydrogen Energy, 39**,** 18264-18272.

AUPRÊTRE, F., DESCORME, C. & DUPREZ, D. 2002. Bio-ethanol catalytic steam reforming over supported metal catalysts. Catalysis Communications, 3**,** 263-267.

BACAS 2006. Hydrogen as an energy carrier Royal Belgian Academy Council
of Applied Science

BALASUBRAMANIAN, B., ORTIZ, A. L., KAYTAKOGLU, S. & HARRISON, D. 1999. Hydrogen from methane in a single-step process. Chemical Engineering Science, 54**,** 3543-3552.

BALL, M. & WIETSCHEL, M. 2009. The future of hydrogen–opportunities and challenges. International Journal of Hydrogen Energy, 34**,** 615-627.

BANDI, A., SPECHT, M., SICHLER, P. & NICOLOSO, N. In situ gas conditioning in fuel reforming for hydrogen generation. 5th International Symposium on Gas Cleaning at High Temperature. US DOE National Energy Technology Laboratory, Morgantown, USA, 2002.

BARELLI, L., BIDINI, G., GALLORINI, F. & SERVILI, S. 2008. Hydrogen production through sorption-enhanced steam methane reforming and membrane technology: A review. Energy, 33**,** 554-570.

BARKER, R. 1973. The reversibility of the reaction $CaCO_3 \rightleftarrows CaO + CO_2$. Journal of applied Chemistry and biotechnology, 23**,** 733-742.

BARTHOLOMEW, C. H. 2001. Mechanisms of catalyst deactivation. Applied Catalysis A: General, 212**,** 17-60.

BARTHOLOMEW, C. H. & FARRAUTO, R. J. 2011. Fundamentals of industrial catalytic processes, John Wiley & Sons.

BASAGIANNIS, A. C., PANAGIOTOPOULOU, P. & VERYKIOS, X. E. 2008. Low temperature steam reforming of ethanol over supported noble metal catalysts. Topics in catalysis, 51**,** 2-12.

BASMADJIAN, D. 1996. The little adsorption book: a practical guide for engineers and scientists, crc press.

BENGAARD, H. S., NØRSKOV, J. K., SEHESTED, J., CLAUSEN, B., NIELSEN, L., MOLENBROEK, A. & ROSTRUP-NIELSEN, J. 2002. Steam reforming and graphite formation on Ni catalysts. Journal of Catalysis, 209**,** 365-384.

BERUTO, D., BARCO, L. & SEARCY, A. W. 1984. CO_2-Catalyzed Surface Area and Porosity Changes in High-Surface-Area CaO Aggregates. Journal of the american ceramic society, 67**,** 512-516.

BHAT, S. A. & SADHUKHAN, J. 2009. Process intensification aspects for steam methane reforming: an overview. AIChE Journal, 55**,** 408-422.

BHATIA, K. K. & WANG, C.-Y. 2004. Transient carbon monoxide poisoning of a polymer electrolyte fuel cell operating on diluted hydrogen feed. Electrochimica Acta, 49**,** 2333-2341.

BHATIA, S. & PERLMUTTER, D. 1983. Effect of the product layer on the kinetics of the CO_2-lime reaction. AIChE Journal, 29**,** 79-86.

BION, N., DUPREZ, D. & EPRON, F. 2012. Design of nanocatalysts for green hydrogen production from bioethanol. ChemSusChem, 5**,** 76-84.

BLAMEY, J., ANTHONY, E., WANG, J. & FENNELL, P. 2010. The calcium looping cycle for large-scale CO_2 capture. Progress in Energy and Combustion Science, 36**,** 260-279.

BLAN ET AL. 2013. Available: https://controls.engin.umich.edu/wiki/index.php/CompositionSensors.

BOHN, C. D., MULLER, C. R., CLEETON, J. P., HAYHURST, A. N., DAVIDSON, J. F., SCOTT, S. A. & DENNIS, J. S. 2008. Production of very pure hydrogen with simultaneous capture of carbon dioxide using the redox reactions of iron oxides in packed beds. Industrial & Engineering Chemistry Research, 47**,** 7623-7630.

BONJOUR, J., CLAUSSE, M. & MEUNIER, F. 2005. A TSA process with indirect heating and cooling: parametric analysis and scaling-up to practical sizes. Chemical Engineering and Processing: Process Intensification, 44**,** 969-977.

BORGWARDT, R. H. 1989. Calcium oxide sintering in atmospheres containing water and carbon dioxide. Industrial & Engineering Chemistry Research, 28**,** 493-500.

BROWN, M., DOLLIMORE, D. & GALWEY, A. 1980. Reactions in the solid state. Comprehensive chemical kinetics, vol. 2. XXIIElsevier, Amsterdam.

BRUN-TSEKHOVOI, A., ZADORIN, A., KATSOBASHVILI, Y. R. & KOURDYUMOV, S. The process of catalytic steam-reforming of hydrocarbons in the presence of carbon dioxide acceptor. Hydrogen energy progress VII, proceedings of the 7th world hydrogen energy conference, 1988. 25-29.

BRUNAUER, S., EMMETT, P. H. & TELLER, E. 1938. Adsorption of gases in multimolecular layers. Journal of the American Chemical Society, 60**,** 309-319.

BSHISH, A., YAAKOB, Z., NARAYANAN, B., RAMAKRISHNAN, R. & EBSHISH, A. 2011. Steam-reforming of ethanol for hydrogen production. Chemical Papers, 65**,** 251-266.

BUSCA, G., COSTANTINO, U., MONTANARI, T., RAMIS, G., RESINI, C. & SISANI, M. 2010. Nickel versus cobalt catalysts for hydrogen production by ethanol steam reforming: Ni–Co–Zn–Al catalysts from hydrotalcite-like precursors. international journal of hydrogen energy, 35**,** 5356-5366.

CALLES, J., CARRERO, A., VIZCAÍNO, A., LINDO, M., STOLTEN, D. & GRUBE, T. 2010. Hydrogen Production by Ethanol Steam Reforming on Ni/SiO_2 Catalysts: Effect of Ce and Zr Incorporation. Report Nr.: Schriften des Forschungszentrums Jülich/Energy & Environment.

CARRERO, A., CALLES, J. & VIZCAÍNO, A. 2010. Effect of Mg and Ca addition on coke deposition over Cu–Ni/SiO 2 catalysts for ethanol steam reforming. Chemical Engineering Journal, 163**,** 395-402.

CARVILL, B., HUFTON, J., ANAND, M. & SIRCAR, S. 1996. Sorption-enhanced reaction process. AIChE Journal, 42**,** 2765-2772.

CAVALLARO, S., CHIODO, V., FRENI, S., MONDELLO, N. & FRUSTERI, F. 2003. Performance of Rh/Al_2O_3 catalyst in the steam reforming of ethanol: H 2 production for MCFC. Applied Catalysis A: General, 249**,** 119-128.

CHEMGUIDE 2000. THE MASS SPECTROMETER

CHEN, D., GRØNVOLD, A., REBO, H., MOLJORD, K. & HOLMEN, A. 1996. Catalyst deactivation studied by conventional and oscillating microbalance reactors. Applied Catalysis A: General, 137**,** L1-L8.

CHEN, Y., SHAO, Z. & XU, N. 2008. Ethanol Steam Reforming over Pt Catalysts Supported on $Ce_x Zr^{1-}{}_x O_2$ Prepared via a Glycine Nitrate Process. Energy & Fuels, 22**,** 1873-1879.

CHEN, Z., SONG, H. S., PORTILLO, M., LIM, C. J., GRACE, J. R. & ANTHONY, E. 2009. Long-term calcination/carbonation cycling and thermal pretreatment for CO_2 capture by limestone and dolomite. Energy & Fuels, 23**,** 1437-1444.

CHEN, Z., YAN, Y. & ELNASHAIE, S. S. 2004. Catalyst deactivation and engineering control for steam reforming of higher hydrocarbons in a novel membrane reformer. Chemical engineering science, 59**,** 1965-1978.

CHENG, X., HUA, W., YONGGANG, W., KONGZHAI, L. & XING, Z. 2010. Preparation and characterization of Ce-Fe-Zr-O (x)/MgO complex oxides for selective oxidation of methane to synthesize gas. Journal of Rare Earths, 28**,** 316-321.

CHENG, Z., WU, Q., LI, J. & ZHU, Q. 1996. Effects of promoters and preparation procedures on reforming of methane with carbon dioxide over Ni/Al_2O_3 catalyst. Catalysis Today, 30**,** 147-155.

CHO, W. C., LEE, D. Y., SEO, M. W., KIM, S. D., KANG, K., BAE, K. K., KIM, C. H., JEONG, S. & PARK, C. S. 2014. Continuous operation characteristics of chemical looping hydrogen production system. Applied Energy, 113**,** 1667-1674.

CHOI, S., DRESE, J. H. & JONES, C. W. 2009. Adsorbent materials for carbon dioxide capture from large anthropogenic point sources. ChemSusChem, 2**,** 796-854.

CHRISTENSEN, K. O., CHEN, D., LØDENG, R. & HOLMEN, A. 2006. Effect of supports and Ni crystal size on carbon formation and sintering during steam methane reforming. Applied Catalysis A: General, 314**,** 9-22.

CHUE, K., KIM, J., YOO, Y., CHO, S. & YANG, R. 1995. Comparison of activated carbon and zeolite 13X for CO_2 recovery from flue gas by pressure swing adsorption. Industrial & Engineering Chemistry Research, 34**,** 591-598.

CIAMBELLI, P., PALMA, V. & RUGGIERO, A. 2010. Low temperature catalytic steam reforming of ethanol. 2. Preliminary kinetic investigation of Pt/CeO_2 catalysts. Applied Catalysis B: Environmental, 96**,** 190-197.

COBO, M., PIERUCCINI, D., ABELLO, R., ARIZA, L., CÓRDOBA, L. F. & CONESA, J. A. 2013. Steam reforming of ethanol over bimetallic $RhPt/La_2O_3$: long-term stability under favorable reaction conditions. International Journal of Hydrogen Energy, 38**,** 5580-5593.

COLLODI, G. & WHEELER, F. 2010. Hydrogen production via steam reforming with CO_2 capture. Chemical Engineering Transactions, 19**,** 37-42.

COMMERCIALIZATION, A. I. L. 2004. Research Needs to Advance New Technology. BCS Incorporated.

CONDON, J. B. 2006. Surface area and porosity determinations by physisorption: measurements and theory, Elsevier.

CRIADO, Y. A., ALONSO, M. & ABANADES, J. C. 2014. Kinetics of the $CaO/Ca(OH)_2$ hydration/dehydration reaction for thermochemical energy storage applications. Industrial & Engineering Chemistry Research, 53**,** 12594-12601.

CUÉLLAR-FRANCA, R. M. & AZAPAGIC, A. 2015. Carbon capture, storage and utilisation technologies: A critical analysis and comparison of their life cycle environmental impacts. Journal of CO_2 Utilization, 9**,** 82-102.

DA SILVA, C. C. & SOMBRA, A. S. 2011. Temperature dependence of the magnetic and electric properties of $Ca_2Fe_2O_5$. Materials Sciences and Applications, 2**,** 1349.

DAI, Z., NOBLE, R. D., GIN, D. L., ZHANG, X. & DENG, L. 2015. Combination of Ionic liquids with membrane technology: A new approach for CO_2 separation. Journal of Membrane Science.

DELUGA, G., SALGE, J., SCHMIDT, L. & VERYKIOS, X. 2004. Renewable hydrogen from ethanol by autothermal reforming. Science, 303**,** 993-997.

DENG, L., KIM, T.-J., SANDRU, M. & HÄGG, M.-B. PVA/PVAm blend FSC membrane for natural gas sweetening. Proceedings of the 1st Annual Gas Processing Symposium, 2009. Elsevier Amsterdam, 247-255.

DEREVSCHIKOV, V., LYSIKOV, A. & OKUNEV, A. 2011. High temperature CaO/Y_2O_3 carbon dioxide absorbent with enhanced stability for sorption-enhanced reforming applications. Industrial & Engineering Chemistry Research, 50**,** 12741-12749.

DEROUANE, E. G. 1998. Zeolites as solid solvents. Journal of Molecular Catalysis A: Chemical, 134**,** 29-45.

DIAGNE, C., IDRISS, H. & KIENNEMANN, A. 2002. Hydrogen production by ethanol reforming over $Rh/CeO_2–ZrO_2$ catalysts. Catalysis Communications, 3**,** 565-571.

DIAGNE, C., IDRISS, H., PEARSON, K., GÓMEZ-GARCÍA, M. A. & KIENNEMANN, A. 2004. Efficient hydrogen production by ethanol reforming over Rh catalysts. Effect of

addition of Zr on CeO_2 for the oxidation of CO to CO_2. Comptes Rendus Chimie, 7**,** 617-622.

DINCER, I. & ACAR, C. 2015. Review and evaluation of hydrogen production methods for better sustainability. International Journal of Hydrogen Energy.

DING, Y. & ALPAY, E. 2000a. Adsorption-enhanced steam–methane reforming. Chemical Engineering Science, 55**,** 3929-3940.

DING, Y. & ALPAY, E. 2000b. Equilibria and kinetics of CO_2 adsorption on hydrotalcite adsorbent. Chemical Engineering Science, 55**,** 3461-3474.

DO, D. D. 1998. Adsorption analysis, World Scientific.

DOMÍNGUEZ, M., TABOADA, E., IDRISS, H., MOLINS, E. & LLORCA, J. 2010. Fast and efficient hydrogen generation catalyzed by cobalt talc nanolayers dispersed in silica aerogel. Journal of Materials Chemistry, 20**,** 4875-4883.

DULLIEN, F. A. 2012. Porous media: fluid transport and pore structure, Academic press.

DUNN, S. 2002. Hydrogen futures: toward a sustainable energy system. International journal of hydrogen energy, 27**,** 235-264.

EBNER, A. D., REYNOLDS, S. P. & RITTER, J. A. 2007. Nonequilibrium kinetic model that describes the reversible adsorption and desorption behavior of CO_2 in a K-promoted hydrotalcite-like compound. Industrial & engineering chemistry research, 46**,** 1737-1744.

EC 2003. Hydrogen Energy and Fuel Cells

EERE 2010. FUEL CELL TECHNOLOGIES PROGRAM. U.S: US department of Energy.

ERDŐHELYI, A., RASKÓ, J., KECSKÉS, T., TÓTH, M., DÖMÖK, M. & BAÁN, K. 2006. Hydrogen formation in ethanol reforming on supported noble metal catalysts. Catalysis Today, 116**,** 367-376.

EWING, J., BERUTO, D. & SEARCY, A. W. 1979. The nature of CaO produced by calcite powder decomposition in vacuum and in CO_2. Journal of the American Ceramic Society, 62**,** 580-584.

FABER, J. & FAWCETT, T. 2002. The powder diffraction file: present and future. Acta Crystallographica Section B: Structural Science, 58**,** 325-332.

FAJARDO, H. V. & PROBST, L. F. D. 2006. Production of hydrogen by steam reforming of ethanol over Ni/Al_2O_3 spherical catalysts. Applied Catalysis A: General, 306**,** 134-141.

FENG, B., LIU, W., LI, X. & AN, H. 2006. Overcoming the problem of loss-in-capacity of calcium oxide in CO_2 capture. Energy & Fuels, 20**,** 2417-2420.

FENNELL, P. S., PACCIANI, R., DENNIS, J. S., DAVIDSON, J. F. & HAYHURST, A. N. 2007. The effects of repeated cycles of calcination and carbonation on a variety of different limestones, as measured in a hot fluidized bed of sand. Energy & fuels, 21**,** 2072-2081.

FLOCH, P., GABRIEL, S., MANSILLA, C. & WERKOFF, F. 2007. On the production of hydrogen via alkaline electrolysis during off-peak periods. International Journal of Hydrogen Energy, 32**,** 4641-4647.

FORNASIERO, P., BALDUCCI, G., DI MONTE, R., KAŠPAR, J., SERGO, V., GUBITOSA, G., FERRERO, A. & GRAZIANI, M. 1996. Modification of the redox behaviour of CeO_2 induced by structural doping with ZrO 2. Journal of Catalysis, 164**,** 173-183.

FREEMANTLE, M. 1998. Designer solvents-Ionic liquids may boost clean technology development. Chemical & engineering news, 76**,** 32-37.

FRIED, J. R. 2014. Polymer science and technology, Pearson Education.

FRUSTERI, F., FRENI, S., SPADARO, L., CHIODO, V., BONURA, G., DONATO, S. & CAVALLARO, S. 2004. H 2 production for MC fuel cell by steam reforming of ethanol over MgO supported Pd, Rh, Ni and Co catalysts. Catalysis Communications, 5**,** 611-615.

GALVITA, V. & SUNDMACHER, K. 2007. Redox behavior and reduction mechanism of Fe_2O_3–$CeZrO_2$ as oxygen storage material. Journal of Materials Science, 42**,** 9300-9307.

GERMAN, R. M. 1996. Sintering theory and practice. Sintering Theory and Practice, by Randall M. German, pp. 568. ISBN 0-471-05786-X. Wiley-VCH, January 1996., 1.

GEUS, J. 1986. Preparation and properties of iron oxide and metallic iron catalysts. Applied Catalysis, 25**,** 313-333.

GIESCHE, H. 2006. Mercury porosimetry: a general (practical) overview. Particle & particle systems characterization, 23**,** 9-19.

GINSTLING, A. & BROUNSHTEIN, B. 1950. Concerning the diffusion kinetics of reactions in spherical particles. J. Appl. Chem. USSR, 23**,** 1327-1338.

GORTE, R. & ZHAO, S. 2005. Studies of the water-gas-shift reaction with ceria-supported precious metals. Catalysis Today, 104**,** 18-24.

GOULA, M. A., KONTOU, S. K. & TSIAKARAS, P. E. 2004. Hydrogen production by ethanol steam reforming over a commercial Pd/γ-Al_2O_3 catalyst. Applied Catalysis B: Environmental, 49**,** 135-144.

GRASA, G. S. & ABANADES, J. C. 2006. CO_2 capture capacity of CaO in long series of carbonation/calcination cycles. Industrial & Engineering Chemistry Research, 45**,** 8846-8851.

GRUENE, P., BELOVA, A. G., YEGULALP, T. M., FARRAUTO, R. J. & CASTALDI, M. J. 2011. Dispersed Calcium Oxide as a Reversible and Efficient CO_2– Sorbent at Intermediate Temperatures. Industrial & Engineering Chemistry Research, 50**,** 4042-4049.

GUILHAUS, M. 1995. Special feature: Tutorial. Principles and instrumentation in time-of-flight mass spectrometry. Physical and instrumental concepts. Journal of Mass Spectrometry, 30**,** 1519-1532.

HAN, C. & HARRISON, D. P. 1994. Simultaneous shift reaction and carbon dioxide separation for the direct production of hydrogen. Chemical Engineering Science, 49**,** 5875-5883.

HAN, C., SILABAN, A., NARCIDA, M. & HARRISON, D. 1994. A calcium oxide sorbent process for bulk separation of carbon dioxide. Final report. Louisiana State Univ., Baton Rouge, LA (United States). Dept. of Chemical Engineering.

HAN, X., YU, Y., HE, H. & SHAN, W. 2013. Hydrogen production from oxidative steam reforming of ethanol over rhodium catalysts supported on Ce–La solid solution. international journal of hydrogen energy, 38**,** 10293-10304.

HARRIS, D. C. 1999. 24. Gas Chromatography. Quantitative chemical analysis**,** 675-712.

HARRISON, D. P. 2008. Sorption-enhanced hydrogen production: a review. Industrial & Engineering Chemistry Research, 47**,** 6486-6501.

HARYANTO, A., FERNANDO, S., MURALI, N. & ADHIKARI, S. 2005. Current status of hydrogen production techniques by steam reforming of ethanol: a review. Energy & Fuels, 19**,** 2098-2106.

HE, L., BERNTSEN, H. & CHEN, D. 2009. Approaching Sustainable H_2 Production: Sorption Enhanced Steam Reforming of Ethanol†. The Journal of Physical Chemistry A, 114**,** 3834-3844.

HEDIN, N., ANDERSSON, L., BERGSTRÖM, L. & YAN, J. 2013. Adsorbents for the post-combustion capture of CO_2 using rapid temperature swing or vacuum swing adsorption. Applied Energy, 104**,** 418-433.

HENNINGS, U. & REIMERT, R. 2008. Stability of rhodium catalysts supported on gadolinium doped ceria under steam reforming conditions. Applied Catalysis A: General, 337**,** 1-9.

HOFFMANN, E. 1996. Mass spectrometry, Wiley Online Library.

HOLLING, B., KANDZIORA, C. & RITTER, R. 2013. CO_2 Recovery from Industrial Hydrogen Facilities and Steel Production to Comply With Future European Emission Regulations. Energy Procedia, 37**,** 7221-7230.

HOMSI, D. 2012. Steam reforming of methane ans ethanol over CoMgAl, Ru/CoMgAl and Cu/CoMgAl catalysts.

HORMILLEJA, E., DURÁN, P., PLOU, J., HERGUIDO, J. & PEÑA, J. 2014. Hydrogen from ethanol by steam iron process in fixed bed reactor. International Journal of Hydrogen Energy, 39**,** 5267-5273.

HOU, Z., YOKOTA, O., TANAKA, T. & YASHIMA, T. 2003. A novel KCaNi/α-Al_2O_3 catalyst for CH4 reforming with CO_2. Catalysis letters, 87**,** 37-42.

HUFTON, J., MAYORGA, S. & SIRCAR, S. 1999. Sorption-enhanced reaction process for hydrogen production. AIChE Journal, 45**,** 248-256.

HUMPHREY, J. L. 1997. Separation process technology, McGraw-Hill (canada).

HUSSEY, C. L. 1988. Room temperature haloaluminate ionic liquids. Novel solvents for transition metal solution chemistry. Pure and applied Chemistry, 60**,** 1763-1772.

HUTSON, N. D., SPEAKMAN, S. A. & PAYZANT, E. A. 2004. Structural effects on the high temperature adsorption of CO_2 on a synthetic hydrotalcite. Chemistry of materials, 16**,** 4135-4143.

IDRISS, H. 2004. Ethanol reactions over the surfaces of noble metal/cerium oxide catalysts. Platinum metals review, 48**,** 105-115.

IEA 2012. World Energy Outlook 2012. International Energy Agency.

IEA 2013. Key World Energy Statistics. International Energy Agency.

IEA 2014. Key World Energy Statistics. International Energy Agency.

IEA 2015. Energy and climate change,World Energy Outlook Special Report. France: International Energy Agency.

JAIN, I. 2009. Hydrogen the fuel for 21st century. International journal of hydrogen energy, 34**,** 7368-7378.

JIANG, L., HAIXIA, Z., GONGQUAN, S. & QIN, X. 2006. Influence of preparation method on the performance of PtSn/C anode electrocatalyst for direct ethanol fuel cells. Chinese Journal of Catalysis, 27**,** 15-19.

JOHNSEN, K. 2006. Sorption-enhanced steam methane reforming in fluidized bed reactors.

KADDOURI, A. & MAZZOCCHIA, C. 2004. A study of the influence of the synthesis conditions upon the catalytic properties of Co/SiO_2 or Co/Al_2O_3 catalysts used for ethanol steam reforming. Catalysis Communications, 5**,** 339-345.

KARASEK, F. W. & CLEMENT, R. E. 2012. Basic gas chromatography-mass spectrometry: principles and techniques, Elsevier.

KARELOVIC, A., GARCÍA, X., WOJCIESZAK, R., RUIZ, P. & GORDON, A. L. 2010. Insight on the promoting effect of Zr and Ti on the catalytic properties of Rh/SiO_2 for partial oxidation of methane. Applied Catalysis A: General, 384**,** 220-229.

KÄRGER, J. & RUTHVEN, D. M. 1992. Diffusion in zeolites and other microporous solids, Wiley New York.

KHAWAM, A. 2007. Application of solid-state kinetics to desolvation reactions.

KHAWAM, A. & FLANAGAN, D. R. 2006. Solid-state kinetic models: basics and mathematical fundamentals. The Journal of Physical Chemistry B, 110**,** 17315-17328.

KHZOUZ, M. 2014. The development and characterization of Ni-Cu/Al_2O_3 catalyst for hydrogen production via multi-fuel reforming. University of Birmingham.

KIERZKOWSKA, A. M. & MÜLLER, C. R. 2013. Sol–Gel-Derived, Calcium-Based, Copper-Functionalised CO_2 Sorbents for an Integrated Chemical Looping Combustion–Calcium Looping CO_2 Capture Process. ChemPlusChem, 78**,** 92-100.

KIM, S., HAN, S. H. & LEE, Y. M. 2012. Thermally rearranged (TR) polybenzoxazole hollow fiber membranes for CO_2 capture. Journal of Membrane Science, 403**,** 169-178.

KIM, T.-J., VRÅLSTAD, H., SANDRU, M. & HÄGG, M.-B. 2013. Separation performance of PVAm composite membrane for CO_2 capture at various pH levels. Journal of Membrane Science, 428**,** 218-224.

KLUG, H. P. & ALEXANDER, L. E. 1954. X-ray diffraction procedures, Wiley New York.

KO, D., SIRIWARDANE, R. & BIEGLER, L. T. 2005. Optimization of pressure swing adsorption and fractionated vacuum pressure swing adsorption processes for CO_2 capture. Industrial & engineering chemistry research, 44**,** 8084-8094.

KOH, A. C., LEONG, W. K., CHEN, L., ANG, T. P., LIN, J., JOHNSON, B. F. & KHIMYAK, T. 2008. Highly efficient ruthenium and ruthenium–platinum cluster-derived nanocatalysts for hydrogen production via ethanol steam reforming. Catalysis Communications, 9**,** 170-175.

KOHL, A. L. & NIELSEN, R. 1997. Gas purification, Gulf Professional Publishing.

KOIRALA, R., REDDY, G. K. & SMIRNIOTIS, P. G. 2012. Single nozzle flame-made highly durable metal doped Ca-based sorbents for CO_2 capture at high temperature. Energy & Fuels, 26**,** 3103-3109.

KUGAI, J., VELU, S. & SONG, C. 2005. Low-temperature reforming of ethanol over CeO_2-supported Ni-Rh bimetallic catalysts for hydrogen production. Catalysis Letters, 101**,** 255-264.

KUMAR, A., PRASAD, R. & SHARMA, Y. 2014. Steam reforming of ethanol: production of renewable hydrogen. Int J Environ Res Dev, 4**,** 203-212.

KWON, S., FAN, M., DACOSTA, H. F., RUSSELL, A. G. & TSOURIS, C. 2011. Reaction kinetics of CO_2 carbonation with Mg-rich minerals. The Journal of Physical Chemistry A, 115**,** 7638-7644.

KYAW, K., MATSUDA, H. & HASATANI, M. 1996. Applicability of Carbonation/Decarbonation Reactions to High-Tempereture Thermal Energy Storage and Temperature Upgrading. Journal of chemical engineering of Japan, 29**,** 119-125.

LEHMANN, W. D. 2011. Jürgen H. Gross: Mass spectrometry–A Textbook. Analytical and Bioanalytical Chemistry, 401**,** 3033-3034.

LEUNG, D. Y., CARAMANNA, G. & MAROTO-VALER, M. M. 2014. An overview of current status of carbon dioxide capture and storage technologies. Renewable and Sustainable Energy Reviews, 39**,** 426-443.

LEWIS, M. & TAYLOR, A. 2006. High temperature thermochemical processes. DOE Hydrogen Program.

LI, K., HANEDA, M., GU, Z., WANG, H. & OZAWA, M. 2013. Modification of CeO_2 on the redox property of Fe_2O_3. Materials Letters, 93**,** 129-132.

LI, Z.-S., CAI, N.-S., HUANG, Y.-Y. & HAN, H.-J. 2005. Synthesis, experimental studies, and analysis of a new calcium-based carbon dioxide absorbent. Energy & Fuels, 19**,** 1447-1452.

LIANG, G., HUOT, J., BOILY, S., VAN NESTE, A. & SCHULZ, R. 1999a. Catalytic effect of transition metals on hydrogen sorption in nanocrystalline ball milled MgH_2–Tm (Tm=Ti, V, Mn, Fe and Ni) systems. Journal of Alloys and Compounds, 292**,** 247-252.

LIANG, G., HUOT, J., BOILY, S., VAN NESTE, A. & SCHULZ, R. 1999b. Catalytic effect of transition metals on hydrogen sorption in nanocrystalline ball milled MgH 2–Tm (Tm= Ti, V, Mn, Fe and Ni) systems. Journal of Alloys and Compounds, 292**,** 247-252.

LIGURAS, D. K., KONDARIDES, D. I. & VERYKIOS, X. E. 2003. Production of hydrogen for fuel cells by steam reforming of ethanol over supported noble metal catalysts. Applied Catalysis B: Environmental, 43**,** 345-354.

LIPMAN, T. E. 2004. What will power the hydrogen economy. Analysis and report prepared for the natural resources defense council, 3.

LIU, W., FENG, B., WU, Y., WANG, G., BARRY, J. & DINIZ DA COSTA, J. O. C. 2010. Synthesis of sintering-resistant sorbents for CO_2 capture. Environmental science & technology, 44**,** 3093-3097.

LLORCA, J., HOMS, N. S., SALES, J. & DE LA PISCINA, P. R. R. 2002. Efficient production of hydrogen over supported cobalt catalysts from ethanol steam reforming. Journal of Catalysis, 209**,** 306-317.

LOPEZ-RAMON, M., JAGIELLO, J., BANDOSZ, T. & SEATON, N. 1997. Characterisation of microporous carbons by using molecular simulation to analyse the adsorption of molecules of different sizes. SPECIAL PUBLICATION-ROYAL SOCIETY OF CHEMISTRY, 213**,** 73-80.

LÓPEZ-ORTIZ, A., RIVERA, N. P., ROJAS, A. R. & GUTIERREZ, D. L. 2005. Novel carbon dioxide solid acceptors using sodium containing oxides. Separation science and technology, 39**,** 3559-3572.

LOPEZ ORTIZ, A. & HARRISON, D. P. 2001. Hydrogen production using sorption-enhanced reaction. Industrial & Engineering Chemistry Research, 40**,** 5102-5109.

LOVON, A. S., LOVON-QUINTANA, J. J., ALMERINDO, G. I., VALENCA, G. P., BERNARDI, M. I., ARAUJO, V. D., RODRIGUES, T. S., ROBLES-DUTENHEFNER, P. A. & FAJARDO, H. V. 2012. Preparation, structural characterization and catalytic properties of Co/CeO_2 catalysts for the steam reforming of ethanol and hydrogen production. Journal of Power Sources, 216**,** 281-289.

LU, H., KHAN, A., PRATSINIS, S. E. & SMIRNIOTIS, P. G. 2008a. Flame-made durable doped-CaO nanosorbents for CO_2 capture. Energy & Fuels, 23**,** 1093-1100.

LU, H., KHAN, A. & SMIRNIOTIS, P. G. 2008b. Relationship between Structural Properties and CO_2 Capture Performance of CaO– Based Sorbents Obtained from Different Organometallic Precursors. Industrial & Engineering Chemistry Research, 47**,** 6216-6220.

LU, H., SMIRNIOTIS, P. G., ERNST, F. O. & PRATSINIS, S. E. 2009. Nanostructured Ca-based sorbents with high CO_2 uptake efficiency. Chemical Engineering Science, 64**,** 1936-1943.

LYSIKOV, A., TRUKHAN, S. & OKUNEV, A. 2008. Sorption enhanced hydrocarbons reforming for fuel cell powered generators. International Journal of Hydrogen Energy, 33**,** 3061-3066.

MACHOCKI, A., DENIS, A., GRZEGORCZYK, W. & GAC, W. 2010. Nano-and micro-powder of zirconia and ceria-supported cobalt catalysts for the steam reforming of bio-ethanol. Applied Surface Science, 256**,** 5551-5558.

MAŁECKI, A., TAREEN, J. A., DOUMERC, J. P., RABARDEL, L. & LAUNAY, J. C. 1985. Kinetics of thermal decomposition of Co_3O_4 powder and single crystals. Journal of Solid State Chemistry, 56**,** 49-57.

MANOVIC, V. & ANTHONY, E. J. 2007. SO_2 retention by reactivated CaO-based sorbent from multiple CO_2 capture cycles. Environmental science & technology, 41**,** 4435-4440.

MANOVIC, V. & ANTHONY, E. J. 2009. Long-term behavior of CaO-based pellets supported by calcium aluminate cements in a long series of CO_2 capture cycles. Industrial & Engineering Chemistry Research, 48**,** 8906-8912.

MANOVIC, V. & ANTHONY, E. J. 2010. Carbonation of CaO-based sorbents enhanced by steam addition. Industrial & engineering chemistry research, 49**,** 9105-9110.

MARIOLAKOS, I., KRANIOTI, A., MARKATSELIS, E. & PAPAGEORGIOU, M. 2007. Water, mythology and environmental education. Desalination, 213**,** 141-146.

MARKEWITZ, P., KUCKSHINRICHS, W., LEITNER, W., LINSSEN, J., ZAPP, P., BONGARTZ, R., SCHREIBER, A. & MÜLLER, T. E. 2012. Worldwide innovations in the development of carbon capture technologies and the utilization of CO_2. Energy & environmental science, 5**,** 7281-7305.

MARTIN, D. & DUPREZ, D. 1995. The effects of support and of particle size on the redox properties of rhodium. Applied Catalysis A: General, 131**,** 297-307.

MARTOS, C., DUFOUR, J. & RUIZ, A. 2009. Synthesis of Fe_3O_4-based catalysts for the high-temperature water gas shift reaction. international journal of hydrogen energy, 34**,** 4475-4481.

MATJUSHI, M. P. Z. M., GIANNETTO, G., URBINA, C., GARCIA, L., BOLIVAR, C., SCOTT, C., BOSCH, P. & LARA, V. 1997. Synthesis and characterization of a zeolite A with detergent characteristics. Characterisation of Porous Solids IV, 4**,** 253.

MATTISSON, T., ZAFAR, Q., LYNGFELT, A. & GEVERT, B. Integrated hydrogen and power production from natural gas with CO_2 capture. 15th World Hydrogen Energy Conference, Yokohama, 27th June-2 July, 2004., 2004.

MCQUILLAN, B., BROWN, L., BESENBRUCH, G., TOLMAN, R., CRAMER, T., RUSS, B., VERMILLION, B., EARL, B., HSIEH, H. & CHEN, Y. 2005. High efficiency generation of hydrogen fuels using solar thermochemical splitting of water: annual report. General Atomics, Report No. GA-A24972.

MEN, Y. & YANG, M. 2012. SMSI-like behavior and Ni promotion effect on NiZnAl catalysts in steam reforming of methanol. Catalysis Communications, 22**,** 68-73.

MENG, L. 2011. Improved hydrogen sorption kinetics in wet ball milled Mg hydrides, Forschungszentrum Jülich.

METZ, B., DAVIDSON, O., DE CONINCK, H., LOOS, M. & MEYER, L. 2005. Carbon dioxide capture and storage, IPCC Geneva, Switzerland.

MILLER, D. D., SIRIWARDANE, R. & POSTON, J. 2015. Fluidized-bed and fixed-bed reactor testing of methane chemical looping combustion with MgO-promoted hematite. Applied Energy, 146**,** 111-121.

MIYATA, S. 1977. Synthesis of Hydrotalcite-Like Compounds and their Physico-Chemical Properties-The Systems Mg^{2+}-Al3^{+}-$SO_4^{2-}$and Mg^{2+}-Al^{3+}-CrO_4^{2}. Clays and Clay minerals, 25**,** 14-18.

MOMIRLAN, M. & VEZIROGLU, T. N. 2005. The properties of hydrogen as fuel tomorrow in sustainable energy system for a cleaner planet. International Journal of Hydrogen Energy, 30**,** 795-802.

MONTES-HERNANDEZ, G., CHIRIAC, R., TOCHE, F. & RENARD, F. 2012. Gas–solid carbonation of $Ca(OH)_2$ and CaO particles under non-isothermal and isothermal conditions by using a thermogravimetric analyzer: implications for CO_2 capture. international journal of Greenhouse Gas Control, 11**,** 172-180.

MURPHY, T. M., OFFORD, G. T. & PAUL, D. R. 2009. Fundamentals of membrane gas separation. Membrane Operations: Innovative Separations and Transformations**,** 63-82.

MURUGAN, A. 2012. Iron-containing perovskite materials for stable hydrogen production by chemical looping water splitting.

MYSCOPE. 2015. Electron-matter interactions [Online]. Available: http://li155-94.members.linode.com/myscope/sem/background/concepts/interactions.php.

NAKAGAWA, K. & OHASHI, T. 1998. A novel method of CO_2 capture from high temperature gases. Journal of the Electrochemical Society, 145**,** 1344-1346.

NOOR, T., GIL, M. V. & CHEN, D. 2014. Production of fuel-cell grade hydrogen by sorption enhanced water gas shift reaction using Pd/Ni–Co catalysts. Applied Catalysis B: Environmental, 150**,** 585-595.

NORBECK, J. M., BARTH, M. J., FARRELL, J. A. & HEFFEL, J. W. 1997. Development and evaluation of a hydrogen fuel power plant for a hybrid electric vehicle—phase II. Final report to the South Coast Air Quality Management District under contract, 95073.

OHASHI, T. & NAKAGAWA, K. Effect of potassium carbonate additive on CO_2 absorption in lithium zirconate powder. MRS Proceedings, 1998. Cambridge Univ Press, 249.

OLIVAS, D. A., GUERRERO, M. B., BRETADO, M. E., DA SILVA PAULA, M. M., GUTIÉRREZ, J. S., VELDERRAIN, V. G., ORTIZ, A. L. & COLLINS-MARTÍNEZ, V. 2014. Enhanced ethanol steam reforming by CO_2 absorption using CaO, CaO* MgO or Na_2ZrO_3. International Journal of Hydrogen Energy, 39**,** 16595-16607.

OTSUKA, K., YAMADA, C., KABURAGI, T. & TAKENAKA, S. 2003. Hydrogen storage and production by redox of iron oxide for polymer electrolyte fuel cell vehicles. International Journal of Hydrogen Energy, 28**,** 335-342.

PACALA, S. & SOCOLOW, R. 2004. Stabilization wedges: solving the climate problem for the next 50 years with current technologies. science, 305**,** 968-972.

PARK, J. & YI, K. B. 2012a. Effects of preparation method on cyclic stability and CO_2 absorption capacity of synthetic CaO–MgO absorbent for sorption-enhanced hydrogen production. International Journal of Hydrogen Energy, 37**,** 95-102.

PARK, J. & YI, K. B. 2012b. Effects of preparation method on cyclic stability and CO_2 absorption capacity of synthetic CaO–MgO absorbent for sorption-enhanced hydrogen production. international journal of hydrogen energy, 37**,** 95-102.

PATTERSON, A. 1939. The Scherrer formula for X-ray particle size determination. Physical review, 56**,** 978.

PEREGO, C. & VILLA, P. 1997. Catalyst preparation methods. Catalysis Today, 34**,** 281-305.

PIRNGRUBER, G. D., CASSIANO-GASPAR, S., LOURET, S., CHAUMONNOT, A. & DELFORT, B. 2009. Amines immobilized on a solid support for postcombustion CO 2 capture–A preliminary analysis of the performance in a VSA or TSA process based on the adsorption isotherms and kinetic data. Energy Procedia, 1**,** 1335-1342.

PLAZA, M., PEVIDA, C., ARENILLAS, A., RUBIERA, F. & PIS, J. 2007. CO_2 capture by adsorption with nitrogen enriched carbons. Fuel, 86**,** 2204-2212.

PLAZINSKI, W., RUDZINSKI, W. & PLAZINSKA, A. 2009. Theoretical models of sorption kinetics including a surface reaction mechanism: a review. Advances in Colloid and Interface Science, 152**,** 2-13.

POJANAVARAPHAN, C., SATITTHAI, U., LUENGNARUEMITCHAI, A. & GULARI, E. 2015. Activity and stability of Au/CeO_2–Fe_2O_3 catalysts for the hydrogen production via oxidative steam reforming of methanol. Journal of Industrial and Engineering Chemistry, 22**,** 41-52.

QIN, C., LIU, W., AN, H., YIN, J. & FENG, B. 2012. Fabrication of CaO-based sorbents for CO_2 capture by a mixing method. Environmental science & technology, 46**,** 1932-1939.

RAMKUMAR, S., PHALAK, N. & FAN, L.-S. 2012. Calcium looping process (CLP) for enhanced steam methane reforming. Industrial & Engineering Chemistry Research, 51**,** 1186-1192.

RAMOS, I. A. C., MONTINI, T., LORENZUT, B., TROIANI, H., GENNARI, F. C., GRAZIANI, M. & FORNASIERO, P. 2012. Hydrogen production from ethanol steam reforming on M/CeO_2/YSZ (M= Ru, Pd, Ag) nanocomposites. Catalysis Today, 180**,** 96-104.

RETALLICK, W. B. 1963. Method for the production of hydrogen. Google Patents.

RFA 2015. World Fuel Ethanol Production. Washington, DC: Renewable Fuels Association.

RICHARDSON, J. T. 1999. Principles of Catalyst Development

RICHARDSON, J. T. 2013. Principles of catalyst development, Springer.

RODRIGUEZ, F., COHEN, C., OBER, C. K. & ARCHER, L. 2014. Principles of polymer systems, Crc Press.

ROGER, W. 1933. Hydrogen production. Google Patents.

ROSSETTI, I., LASSO, J., NICHELE, V., SIGNORETTO, M., FINOCCHIO, E., RAMIS, G. & DI MICHELE, A. 2014. Silica and zirconia supported catalysts for the low-temperature ethanol steam reforming. Applied Catalysis B: Environmental, 150**,** 257-267.

ROSTRUP-NIELSEN, J. R. 1984. Catalytic steam reforming, Springer.

ROSTRUP-NIELSEN, J. R., SEHESTED, J. & NØRSKOV, J. K. 2002. Hydrogen and synthesis gas by steam-and CO_2 reforming. Advances in catalysis, 47**,** 65-139.

ROUQUEROL, J., ROUQUEROL, F., LLEWELLYN, P., MAURIN, G. & SING, K. S. 2013. Adsorption by powders and porous solids: principles, methodology and applications, Academic press.

RUSTEN, H. K. 2010. Simulation and modelling of hydrogen production by sorption enhanced steam methane reforming in fixed bed reactors.

RUTHVEN, D. M. 1984. Principles of adsorption and adsorption processes, John Wiley & Sons.

SALGE, J. R., DELUGA, G. A. & SCHMIDT, L. D. 2005. Catalytic partial oxidation of ethanol over noble metal catalysts. Journal of Catalysis, 235**,** 69-78.

SAMOILA, P., BOUTZELOIT, M., ESPECEL, C., EPRON, F. & MARÉCOT, P. 2010. Relationship between the structural properties of supported bimetallic Pt–Rh catalysts and their performances for methylcyclopentane ring opening. Journal of Catalysis, 276**,** 237-248.

SÁNCHEZ-SÁNCHEZ, M., NAVARRO, R. & FIERRO, J. 2007. Ethanol steam reforming over Ni/MxOy–Al2O3 (M= Ce, La, Zr and Mg) catalysts: influence of support on the hydrogen production. International Journal of Hydrogen Energy, 32**,** 1462-1471.

SÁNCHEZ, L. G., MEINDERSMA, G. & DE HAAN, A. 2011. Kinetics of absorption of CO_2 in amino-functionalized ionic liquids. Chemical Engineering Journal, 166**,** 1104-1115.

SCHELL, J., CASAS, N. & MAZZOTTI, M. 2009. Pre-combustion CO_2 capture for IGCC plants by an adsorption process. Energy Procedia, 1**,** 655-660.

SCHOLES, C. A., CHEN, G. Q., STEVENS, G. W. & KENTISH, S. E. 2010. Plasticization of ultra-thin polysulfone membranes by carbon dioxide. Journal of Membrane Science, 346**,** 208-214.

SCOTT, K. & HUGHES, R. 1996. Introduction to industrial membrane processes. Industrial Membrane Separation Technology. Springer.

SEHESTED, J., GELTEN, J. A. & HELVEG, S. 2006. Sintering of nickel catalysts: Effects of time, atmosphere, temperature, nickel-carrier interactions, and dopants. Applied Catalysis A: General, 309**,** 237-246.

SEKER, E. 2008. The catalytic reforming of bio-ethanol over SiO_2 supported ZnO catalysts: The role of ZnO loading and the steam reforming of acetaldehyde. International Journal of Hydrogen Energy, 33**,** 2044-2052.

SELVAM, P., VISWANATHAN, B., SWAMY, C. & SRINIVASAN, V. 1986a. Magnesium and magnesium alloy hydrides. International Journal of Hydrogen Energy, 11**,** 169-192.

SELVAM, P., VISWANATHAN, B., SWAMY, C. S. & SRINIVASAN, V. 1986b. Magnesium and magnesium alloy hydrides. International Journal of Hydrogen Energy, 11**,** 169-192.

ŠESTÁK, J. & BERGGREN, G. 1971. Study of the kinetics of the mechanism of solid-state reactions at increasing temperatures. Thermochimica Acta, 3**,** 1-12.

SETZER, H. J., BETT, J. A. & LESIEUR, R. R. 1984. Iron oxide catalyst for steam reforming. Google Patents.

SHARMA, P. K., SAXENA, N., BHATT, A., RAJAGOPAL, C. & ROY, P. K. 2013. Synthesis of mesoporous bimetallic Ni–Cu catalysts supported over ZrO_2 by a homogenous urea coprecipitation method for catalytic steam reforming of ethanol. Catalysis Science & Technology, 3**,** 1017-1026.

SHIMIZU, T., HIRAMA, T., HOSODA, H., KITANO, K., INAGAKI, M. & TEJIMA, K. 1999. A twin fluid-bed reactor for removal of CO_2 from combustion processes. Chemical Engineering Research and Design, 77**,** 62-68.

SHIN, H. S. & KNAEBEL, K. 1987. Pressure swing adsorption: A theoretical study of diffusion-induced separations. AIChE journal, 33**,** 654-662.

SIDJABAT, O. & TRIMM, D. 2000. Nickel–magnesia catalysts for the steam reforming of light hydrocarbons. Topics in Catalysis, 11**,** 279-282.

SILABAN, A., NARCIDA, M. & HARRISON, D. 1996. Characteristics of the reversible reaction between CO_2 (g) and calcined dolomite. Chemical Engineering Communications, 146**,** 149-162.

SING, K. S. & GREGG, S. 1982. Adsorption, surface area and porosity. Academic Press, London**,** 1-5.

SONG, H. & OZKAN, U. S. 2009. Ethanol steam reforming over Co-based catalysts: role of oxygen mobility. Journal of Catalysis, 261**,** 66-74.

SUBAN, M., TUŠEK, J. & URAN, M. 2001. Use of hydrogen in welding engineering in former times and today. Journal of Materials Processing Technology, 119**,** 193-198.

SULTANA, K. S. & CHEN, D. 2011. Enhanced hydrogen production by in situ CO_2 removal on $CaCeZrO_x$ nanocrystals. Catalysis Today, 171**,** 43-51.

SUN, J., QIU, X.-P., WU, F. & ZHU, W.-T. 2005. H_2 from steam reforming of ethanol at low temperature over Ni/Y_2O_3, Ni/La_2O_3 and Ni/Al_2O_3 catalysts for fuel-cell application. International Journal of Hydrogen Energy, 30**,** 437-445.

SUN, P., GRACE, J., LIM, C. & ANTHONY, E. 2007a. The effect of CaO sintering on cyclic CO_2 capture in energy systems. AIChE Journal, 53**,** 2432-2442.

SUN, P., GRACE, J. R., LIM, C. J. & ANTHONY, E. J. 2007b. Removal of CO_2 by calcium-based sorbents in the presence of SO_2. Energy & fuels, 21**,** 163-170.

SUN, P., GRACE, J. R., LIM, C. J. & ANTHONY, E. J. 2008. Investigation of attempts to improve cyclic CO_2 capture by sorbent hydration and modification. Industrial & Engineering Chemistry Research, 47**,** 2024-2032.

SYMONDS, R. T., LU, D. Y., MACCHI, A., HUGHES, R. W. & ANTHONY, E. J. 2009. CO_2 capture from syngas via cyclic carbonation/calcination for a naturally occurring limestone: Modelling and bench-scale testing. Chemical Engineering Science, 64**,** 3536-3543.

TAKENAKA, S., NOMURA, K., HANAIZUMI, N. & OTSUKA, K. 2005. Storage and formation of pure hydrogen mediated by the redox of modified iron oxides. Applied Catalysis A: General, 282**,** 333-341.

TALU, O. 1998. Needs, status, techniques and problems with binary gas adsorption experiments. Advances in Colloid and Interface Science, 76**,** 227-269.

THITAKAMOL, B., VEAWAB, A. & AROONWILAS, A. 2007. Environmental impacts of absorption-based CO_2 capture unit for post-combustion treatment of flue gas

from coal-fired power plant. International Journal of Greenhouse Gas Control, 1**,** 318-342.

THOMAS, W. J. & CRITTENDEN, B. D. 1998. Adsorption technology and design, Butterworth-Heinemann.

TIEMERSMA, T., PATIL, C., VAN SINT ANNALAND, M. & KUIPERS, J. 2006. Modelling of packed bed membrane reactors for autothermal production of ultrapure hydrogen. Chemical Engineering Science, 61**,** 1602-1616.

TIEN, C. 1994. Adsorption calculations and modeling.

TWIGG, M. V. & BURGESS, J. 2003. 5.4 - Iron. In: MEYER, J. A. M. J. (ed.) Comprehensive Coordination Chemistry II. Oxford: Pergamon.

TWIGG, M. V. & TWIGG, M. 1989. Catalyst handbook, CSIRO.

VOSS, C. 2005. Applications of pressure swing adsorption technology. Adsorption, 11**,** 527-529.

WALDRON, W. E., HUFTON, J. & SIRCAR, S. 2001. Production of hydrogen by cyclic sorption enhanced reaction process. AIChE journal, 47**,** 1477-1479.

WANAT, E., VENKATARAMAN, K. & SCHMIDT, L. 2004. Steam reforming and water–gas shift of ethanol on Rh and Rh–Ce catalysts in a catalytic wall reactor. Applied Catalysis A: General, 276**,** 155-162.

WANG, F. 2012. Hydrogen production from steam reforming of ethanol over an Ir/ceria-based catalyst: catalyst ageing analysis and performance improvement upon ceria doping. Université Claude Bernard-Lyon I.

WANG, M., LAWAL, A., STEPHENSON, P., SIDDERS, J. & RAMSHAW, C. 2011. Post-combustion CO_2 capture with chemical absorption: A state-of-the-art review. Chemical Engineering Research and Design, 89**,** 1609-1624.

WANG, W., STAGG-WILLIAMS, S. M., NORONHA, F. B., MATTOS, L. V. & PASSOS, F. B. 2004. Partial oxidation and combined reforming of methane on Ce-promoted catalysts. Catalysis today, 98**,** 553-563.

WANG, W. & WANG, Y. 2009. Dry reforming of ethanol for hydrogen production: thermodynamic investigation. International Journal of Hydrogen Energy, 34**,** 5382-5389.

WASHBURN, E. W. 1921. The dynamics of capillary flow. Physical review, 17**,** 273.

WASSERSCHEID, P. & KEIM, W. 2000. Ionic liquids-new" solutions" for transition metal catalysis. Angewandte Chemie, 39**,** 3772-3789.

WEBB, P. A. January 2001. An Introduction To The Physical Characterization of Materials by Mercury

Intrusion Porosimetry with Emphasis On Reduction And Presentation of

Experimental Data. Norcross, Georgia: Micromeritics Instrument Corp.

WEI, J.-M., XU, B.-Q., LI, J.-L., CHENG, Z.-X. & ZHU, Q.-M. 2000. Highly active and stable Ni/ZrO 2 catalyst for syngas production by CO_2 reforming of methane. Applied Catalysis A: General, 196**,** L167-L172.

WEITKAMP, J., SING, K. S. W. & SCHÜTH, F. 2002. Handbook of porous solids, Wiley-Vch.

WELTON, T. 1999. Room-temperature ionic liquids. Solvents for synthesis and catalysis. Chemical reviews, 99**,** 2071-2084.

WESTERMARCK, S. 2000. Use of mercury porosimetry and nitrogen adsorption in characterisation of the pore structure of mannitol and microcrystalline cellulose powders, granules and tablets, University of Helsinki Helsinki, Finland.

WIND, J. D., PAUL, D. R. & KOROS, W. J. 2004. Natural gas permeation in polyimide membranes. Journal of Membrane Science, 228**,** 227-236.

WINTER, C.-J. 2009. Hydrogen energy—Abundant, efficient, clean: A debate over the energy-system-of-change. International Journal of Hydrogen Energy, 34**,** S1-S52.

WITOON, T. 2011. Characterization of calcium oxide derived from waste eggshell and its application as CO_2 sorbent. Ceramics International, 37**,** 3291-3298.

WU, S. & ZHU, Y. 2010. Behavior of $CaTiO_3$/nano-CaO as a CO_2 reactive adsorbent. Industrial & Engineering Chemistry Research, 49**,** 2701-2706.

WU, Y., BLAMEY, J., ANTHONY, E. & FENNELL, P. 2010. Morphological changes of limestone sorbent particles during carbonation/calcination looping cycles in a thermogravimetric analyzer (TGA) and reactivation with steam. Energy & Fuels, 24**,** 2768-2776.

XIAO, P., WILSON, S., XIAO, G., SINGH, R. & WEBLEY, P. 2009. Novel adsorption processes for carbon dioxide capture within a IGCC process. Energy Procedia, 1**,** 631-638.

XIE, C., CHEN, Y., LI, Y., WANG, X. & SONG, C. 2011. Influence of sulfur on the carbon deposition in steam reforming of liquid hydrocarbons over CeO_2–Al_2O_3 supported Ni and Rh catalysts. Applied Catalysis A: General, 394**,** 32-40.

XU, L., ZHAO, H., SONG, H. & CHOU, L. 2012. Ordered mesoporous alumina supported nickel based catalysts for carbon dioxide reforming of methane. International Journal of Hydrogen Energy, 37**,** 7497-7511.

XUAN, J., LEUNG, M. K., LEUNG, D. Y. & NI, M. 2009. A review of biomass-derived fuel processors for fuel cell systems. Renewable and Sustainable Energy Reviews, 13**,** 1301-1313.

YAMAGUCHI, D., TANG, L., WONG, L., BURKE, N., TRIMM, D., NGUYEN, K. & CHIANG, K. 2011. Hydrogen production through methane–steam cyclic redox processes with iron-based metal oxides. International Journal of Hydrogen Energy, 36**,** 6646-6656.

YANG, H., XU, Z., FAN, M., GUPTA, R., SLIMANE, R. B., BLAND, A. E. & WRIGHT, I. 2008. Progress in carbon dioxide separation and capture: A review. Journal of Environmental Sciences, 20**,** 14-27.

YANG, R., KIKKINIDES, E. & CHO, S. 1993. Concentration and Recovery of CO_2 from Fuel Gas by Pressure Swing Adsorption. Ind. Chem. Eng, 32**,** 2714.

YEE, D. & PURI, R. 1995. Coalbed methane recovery using pressure swing adsorption separation. Google Patents.

YI, K. B. & HARRISON, D. P. 2005. Low-pressure sorption-enhanced hydrogen production. Industrial & engineering chemistry research, 44**,** 1665-1669.

YONG, Z., MATA, V. & RODRIGUES, A. E. 2001. Adsorption of carbon dioxide onto hydrotalcite-like compounds (HTlcs) at high temperatures. Industrial & Engineering Chemistry Research, 40**,** 204-209.

YU, Y., LIU, W., AN, H., YANG, F., WANG, G., FENG, B., ZHANG, Z. & RUDOLPH, V. 2012. Modeling of the carbonation behavior of a calcium based sorbent for CO_2 capture. International Journal of Greenhouse Gas Control, 10**,** 510-519.

ZAFAR, Q., MATTISSON, T. & GEVERT, B. 2005. Integrated hydrogen and power production with CO_2 capture using chemical-looping reforming redox reactivity of particles of CuO, Mn_2O_3, NiO, and Fe_2O_3 using SiO_2 as a support. Industrial & engineering chemistry research, 44**,** 3485-3496.

ZEHE 2010. Chemical Equilibrium with Applications,CEA.

ZEMAN, F. 2008. Effect of steam hydration on performance of lime sorbent for CO_2 capture. International journal of greenhouse gas control, 2**,** 203-209.

ZHANG, B., CAI, W., LI, Y., XU, Y. & SHEN, W. 2008. Hydrogen production by steam reforming of ethanol over an Ir/CeO_2 catalyst: reaction mechanism and stability of the catalyst. international journal of hydrogen energy, 33**,** 4377-4386.

ZHOU, Z., QI, Y., XIE, M., CHENG, Z. & YUAN, W. 2012. Synthesis of CaO-based sorbents through incorporation of alumina/aluminate and their CO_2 capture performance. Chemical Engineering Science, 74**,** 172-180.